WELDING OF ASTM A709 GRADE 50CR USING AUSTENITIC FILLER WIRES AT VARYING HEAT INPUTS AND MAXIMUM INTERPASS TEMPERATURES

A Thesis

Presented to

The Faculty of the School of Engineering and Applied Science

University of Virginia

In Partial Fulfillment

Of the Requirements for the Degree

Master of Science in Material Science and Engineering

By Xuemeng Xia,

May 2020

Table of Contents

Abstract

ASTM A709 Grade 50CR (50CR) is a low carbon (< 0.03 wt% C) structural steel with a ferritic-martensitic dual phase microstructure developed to address the corrosion issues associated with the use of traditional weathering steels, especially in environments involving combined prolonged wetness and chloride salts. The typical composition of 50CR contains 10.5 to 12.5 wt% chromium with a maximum of 1.0% silicon, 1.5% of nickel, and 1.5% manganese. When 50CR is produced by ArcelorMittal under the tradename Duracorr®, 0.20 – 0.35% molybdenum is also added. The fabrication of bridge girders from 50CR has largely relied on the use of 309L solid filler wire, which is an austenitic stainless steel. Prior to this research, heat inputs up to 55 kJ/in and maximum interpass temperatures up to 450 °F for 1" thick plate have been explored by the Oregon Department of Transportation.

The objective of this project was to determine the high end of heat inputs and maximum interpass temperatures that could be used during submerged are welding (SAW) of 50CR and to evaluate alternative filler wire materials for fabrication through the use of both 1/2" and 1" thick plates. Given the desire to produce 50CR bridge girders that are considered maintenance-free, microstructural analysis as well as mechanical testing was carried out to evaluate the proposed heat inputs in terms of failure within the lifetime of the bridge. A total of four austenitic stainless steel filler wires were used in this study, three of which were solid wires: 309L, 309LSi, and 316L, and one metal cored wire: 309LC. The heating profile was modeled using the Rosenthal equations while the fusion microstructure was modeled using the Schaeffler constitution diagram.

The following conclusions were drawn from this research. A range of austenitic stainless steel filler wires can be used to successfully weld 50CR; 309LC, 309LSi, and 316L were all found to be viable alternatives to the incumbent filler wire, 309L. Use of 309L filler wires for 1/2" plates results in welds which are borderline with respect to impact energy at the high heat input level of 75 kJ/in, over the maximum interpass temperature range investigated. Lower heat inputs (e.g., 50 kJ/in which was previously shown to be effective) are recommended. Similar results were obtained for welds in 1/2" plates produced with 309LSi and 316L. Heat inputs of up to 75 kJ/in at all maximum interpass temperatures explored (up to 450 °F) can be used to weld 1/2" plates with 309LC filler wire. Heat inputs of up to 90 kJ/in and interpass temperatures of up to 450 °F can be used for all four of the filler wires investigated (309L, 309LC, 309LSi, and 316L) for 1" thick plate. All of the resulting welds surpass the mechanical requirements of AASHTO/AWS D1.5 bridge welding code.

Interestingly, the metal cored wire 309LC out-performed the solid filler wires examined in this study with respect to production (higher deposition rates and fewer required passes) and mechanical properties (especially impact toughness) of the resulting welds. The enhanced toughness and lack of ductile to brittle transition in the fusion zone of 1/2" plates welded using 309LC filler wire appear to be due to the mitigation of large, aligned δ-ferrite grain formation during solidification. Such large, aligned grains otherwise serve as preferred crack paths in welds. This difference in solidification structure is hypothesized to be due to the difference in molten metal transfer modes suggested by literature.

Finally, tensile and Charpy V-notch tests to failure of the base material, 50CR, revealed a curious delamination cracking phenomenon akin to fracturing of wood. The delamination cracking of 50CR occurs due to the intersection of both microstructural and mechanical aspects, including stringers which appear to lower the through-thickness strength of the plate and a pronounced neck (with about 80% reduction in area) that causes the local stress state to transform from uniaxial to triaxial. Future research could focus on exploring the implications of this delamination phenomenon on other sorts of welds, such as T-joints. No cracks of any sort (including delamination cracks), however, were observed in the butt-welds created in this study.

Acknowledgments

I would like to thank my advisor, Dr. James Fitz-Gerald, for his continued support, patience, and expertise. He made me not only the material scientist I am today, but also the person I am. I would also like to thank Dr. Sean Agnew for his ability to provide in the same capacity. My experience at the University of Virginia would not have been the same without them, and I am proud to call them my mentors. I would also like to thank Dr. Bi-Cheng Zhou for taking time out of his busy schedule to serve as my committee chair and to provide his expertise.

I would also like to thank everyone in the Materials Science and Engineering department, people I am grateful to call my friends and colleagues. I would like to extend a special thank you to Kim Fitzhugh-Higgins, who I could always turn to with any problem I was having, whether academic or personal. I could not have succeeded without Sherri Sullivan who was always there to answer any financial questions I had. A special thanks goes out to the Fitz-Gerald, Agnew, and McDonnell lab groups who were always available to lend an ear whenever I had some science or life struggle that I needed to talk out.

I would like to thank the people at the Virginia Transportation Research Council (VTRC) and at the Virginia DOT (VDOT) for their support and funding: especially Dr. Stephen Sharp for acting both as a mentor and for believing enough in me as an intern to offer to send me to graduate school, Bill Ordel for his expertise and for his mentorship, and Jason Provines for his expertise. I would also like to thank all of the industry experts that provided help on this project: Justin Ocel at Turner Fairbank Research Center, Fred Fletcher from ArcelorMittal, and Adam Steppe from High Steel Structures.

Lastly, I'd like to thank my friends and family for providing so much love and support as I journeyed through both my undergraduate and graduate career. A special thanks goes out to the Virginia Glee Club, providing me both a creative outlet and a brotherhood where I am accepted and celebrated as I am. I am truly blessed and grateful to have so many people supporting me.

Chapter 1: Introduction and Background

1.1 Motivation for the Use of Dual Phase Steels

Due to the poor corrosion resistance of mild steel, alternatives with comparable mechanical properties have been explored as replacements in structural applications.[1–3] Although weathering steels are able to meet the mechanical property requirements (strength, ductility, toughness, formability and weldability) for bridge girders, they fail to meet the corrosion resistance necessary in environments with prolonged moisture and/or chloride salts.[1,2,4] Corrosion causes a decrease in the girder web thickness, which leads to an increase in the stress of the load carrying components. Because of this, both weathering and mild steels need to be coated with a protective corrosion resistant barrier every ten to twenty years.[1,4,5] This need for periodic re-coating is costly and often has additional negative social, economic, and environmental impacts.[6] Thus, a more corrosion resistant alternative is sought. Austenitic (and even duplex austenitic-ferritic) stainless steels are too costly due to the higher nickel (Ni) content, while ferritic stainless steels tend to exhibit poor weldability due to the excessive grain growth in the heat affected zone (HAZ), which leads to a decrease in the fracture toughness.[2,3,15,16,7–14] Dual phase (ferritic-martensitic) stainless steels, such as ASTM A709 grade 50CR (50CR), and its legacy alloy, 3CR12, have been offered as a possible solution. Dual phase steels are alloyed and thermo-mechanically processed to possess the corrosion resistance of ferritic stainless steels, while maintaining the strength, toughness, and ductility of carbon steel.[17] Designed to form a protective scale that reduces the atmospheric corrosion rate, 50CR has been determined by various studies to be more cost-effective over the lifetime of a bridge in comparison with weathering steel.[1,5,6,18] However, in order to reap the full benefits of 50CR, the fabrication method for bridge girders, typically through the use of submerged arc welding, must

be optimized and the resulting welds be well characterized, so that the goal of maintenance-free dual phase bridges can be realized.

1.2 Development and Historical Use of High Chromium Dual Phase Steels

Developed in the late 1970s in South Africa by modifying AISI 409 to improve the weldability, 3CR12 is a low carbon (< 0.03%) steel that contains a nominal chromium (Cr) content of 12 wt%.[4,8,13] Meant to fill the gap between conventional carbon steel and stainless steel, 3CR12 has been utilized in many industries successfully due to its wet abrasion and corrosion resistance.[12,15,19,20] The typical mechanical properties were found to be a yield strength of 380 MPa (*55.1 ksi*), a tensile strength of 530 MPa (*76.9 ksi*), and an elongation of 26%.[3,9] The mining industry has heavily utilized 3CR12 for transport carts and mine water conveyance. The equipment used for coal showed little to no indication of general corrosion, discoloration, or pitting. The operation temperature and the chloride and dissolved solid levels in the gold mining waste water varied greatly between locations, which led to mixed results. Similarly, varying results were seen for the waste water industry. In the sugar industry, 3CR12 has been successfully used in equipment for processing both cane and beet sugar.[19]

3CR12 has a banded two phase (ferrite and austenite) microstructure at elevated temperatures, such as during hot rolling.[4,8,19,21–23] This is accomplished by changing the balance of austenite and ferrite stabilizers with reference to the Kaltenhauser equation (Equation 1.1) to place the microstructure within the two phase region, shown in Figure 1.1. Austenite stabilizers, such as Ni, manganese (Mn), carbon (C), and nitrogen (N) stabilize the austenite phase (γ), pushing the γ loop towards higher Cr levels, while ferrite stabilizers, such as Cr, silicon (Si), and molybdenum (Mo), stabilize the ferrite phase (δ at elevated temperatures/α at temperatures below 783 °C (*1360.4 °F)*).[4,24–30] A steel is considered to be fully austenitic at 1000 °C (*1832 °F*) if the Kaltenhauser ferrite factor (KFF) is less than or equal to 8. If the KFF is greater than 8,

then the elevated temperature microstructure is at least partially ferritic.[31] The KFF ranges typically from 9 to 12 for 3CR12.[3]

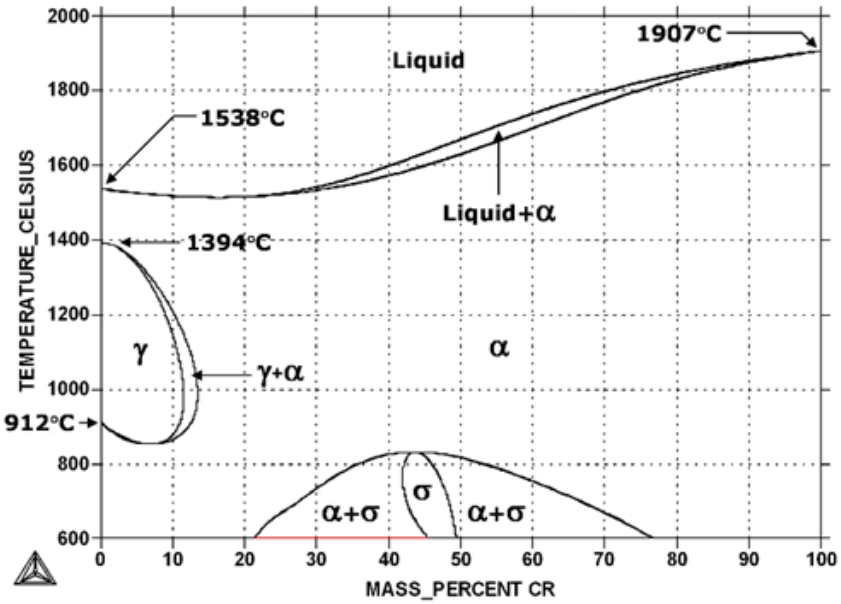

Figure 1.1. *Iron-chromium phase diagram: two of the main components that make up stainless steel, featuring the two equilibrium phases most commonly found in stainless steel: ferrite (α) and austenite (γ). It is important to note that martensite is not present in the phase diagram because it is a metastable phase.*

$$K_m = Cr + 6Si + 8Ti + 4Mo + 2Al - 2Mn - 4Ni - 40(C + N) - 20P - 5Cu$$

Equation 1.1. K_m *is the ferrite number, while* ***Cr***, ***Si***, ***Ti***, ***Mo***, ***Al***, ***Mn***, ***Ni***, ***C***, ***N***, ***P***, *and* ***Cu*** *are the weight percent of chromium, silicon, titanium, molybdenum, aluminum, manganese, nickel, carbon, nitrogen, phosphorous, and copper respectively.*

The martensite start (M_s) temperature for 3CR12 was found to range from 460 – 550 °C (*860 – 1022 °F*).[8,11,32,33] The martensite finish (M_f) temperature was found to range from 380 – 400 °C (*716 – 752 °F*).[11,32] This ensures that any austenite phase in the microstructure will transform into martensite as the alloy is cooled to room temperature resulting in a final microstructure of banded ferrite and martensite.[32,33] The exact phase balance is dependent on both the thermomechanical history and the composition.[32] However, experiments to fully

austenitize the material showed that due to the balance of alloying elements, 3CR12 was never able to reach a microstructure that was 100 vol% austenite.[4,23,32]

To combat the potential issue of chromium carbide formation after a heat treatment, such as welding, which can lead to a phenomenon known as sensitization, 3CR12 was stabilized with titanium (Ti).[21] Sensitization, which is directly related to the carbon content of the alloy, is typically combatted by 1) minimizing the C content 2) stabilizing with Ti, niobium (Nb), or other elements or 3) a combination of 1) and 2).[34] These stabilizing elements are meant to form stable carbides preferentially at higher temperatures so that there is less C available in solution for chromium carbide formation.[3,35]

Due to 3CR12 being Ti stabilized, the precipitates that formed are largely Ti based, such as titanium-carbo-nitrides and titanium-sulfides.[4,22,33,36] This is a key difference between the legacy alloy, 3CR12, and 50CR, formerly known as ASTM A1010.[37] However, 50CR has a similar microstructure of banded ferrite and tempered martensite, and an otherwise identical composition.[18] This can be seen in Table 1.1, which lists the required compositions of the alloy systems relevant to this study.

Table 1.1. *Chemical composition requirements of the AISI 409 based alloy systems mentioned in this thesis. Single values indicate the maximum allowed.*

Element	**AISI 409**[9]	**3CR12**[9]	**Duracorr ®**[18]	**50CR**[37]
C	0.08	0.03	0.025	0.030
N	-	0.03	0.030	0.030
Mn	1.00	1.50	1.50	1.50
P	0.045	0.030	0.40	0.040
S	0.045	0.030	0.010	0.010
Si	1.0	1.0	0.70	1.00
Cr	10.5 – 11.75	11.0 – 12.0	11.0 – 12.5	10.5 – 12.5
Ni	0.5	1.5	1.00	1.50
Other	6xC – 0.75 **Ti**	4(C+N) – 0.6 **Ti**	0.20– 0.35 **Mo**	

50CR has been produced in the United States since 1992. The typical mechanical properties are a yield strength of 56.7 ksi, a tensile strength of 76.7 ksi, and an elongation of 36%.[1] Due to its Cr content, 50CR cannot be efficiently cut using an oxyfuel torch, so plasma, powder, or laser cutting is recommended. Short-term accelerated marine testing and marine atmospheric testing at Kure Beach showed that 50CR had superior corrosion resistance to galvanized coatings and traditional weathering steels.[38] The maximum corrosion rate was found to be less than 0.00025" (6.35 μm) per year.[1] According to its producer, 50CR should be considered for overpasses in northern climates with minimal vertical clearance, bridges over depressed roadways that are commonly subject to concentrated salt spray, or for bridges along the sea coast. However, 50CR is not intended in applications where the bridge will be subject to long-term immersion in salt water environments.[38]

In 2004, the first 50CR (A1010) multi-cell box girder bridge was erected in Williams, California as part of the Innovative Bridge Research and Construction Program.[39] Following its construction, several other state Departments of Transportations (DOTs) as well as commercial entities have begun using 50CR in bridge girder applications, shown in Figure 1.2.[40] Due to the size and shape of bridge girders, the steel I-beams are commonly welded together instead of cast.

a) b)

Figure 1.2. a) *A bridge fabricated from Duracorr at ArcelorMittal's Coatesville facility in Pennsylvania.*[18] ***b)*** *VDOT's Route 340 bridge made from ASTM A709 grade 50CR steel provided by ArcelorMittal in Waynesboro, VA. It is important to note that both bridges are over a body of running water, which would result in prolonged exposure to moisture.*

1.3 Introduction to Arc Welding

Welding, according to Messler Jr., describes the "process in which materials of the same fundamental type or class are brought together and caused to join (and become one) through the formation of primary (and occasionally secondary) chemical bonds under the combined action of heat and pressure." Welding will typically fall into two main categories: heterogenous and homogeneous. Homogeneous welding describes the process of joining two essentially identical types or compositions of materials, while heterogeneous welding joins two dissimilar types or compositions of materials. However, heterogeneous welding requires that the materials to be joined are essentially the same atomic structure so that chemical bonds can form, such as metallic, ionic, or covalent bonds.[41]

Arc welding can typically be broken down into two categories: non-consumable electrode and consumable electrode welding. Non-consumable electrode arc welding includes gas tungsten arc welding (GTAW/TIG), plasma arc welding (PAW), carbon arc welding, stud arc welding, atomic hydrogen welding, and magnetically impelled arc butt welding. Consumable electrode welding includes gas metal arc welding (GMAW/MIG), shielded metal arc welding (SMAW), flux cored arc welding (FCAW), submerged arc welding (SAW), electrogas welding (EGW), and electroslag welding (ESW). When using a consumable electrode, there are three predominant metal transfer modes: 1) free flight transfer 2) bridging transfer and 3) slag-protected transfer. Free flight transfer can further be broken down into spray or globular type transfer. Spray type metal transfer is characterized by the axial transfer of fine molten droplets at the rate of hundreds per second, which leads to an essentially splatter free transfer. Globular type metal transfer causes large globules of molten metal to form at the tip of the consumable and joins the weld pool predominantly by gravity and arc forces. This is typically slower, resulting in a transfer rate of a few (less than ten) droplets per second. Short circuiting metal transfer, the most common

type of bridging transfer, is characterized by a low welding current and voltage. This leads to the slow formation of molten globules at the end of the consumable that will periodically come in contact with the weld pool, causing the molten material to form or join the melt pool. Slag-protected metal transfer applies mainly to the ESW and SAW techniques. Due to the presence of a molten slag layer, the metal transfer from the tip of the welding electrode is never truly free flight. Instead, the molten metal from the electrode transfers through the molten slag layer, resulting in protection from the environment and an overall higher heat efficiency.[42] A schematic of SAW can be seen in Figure 1.3.

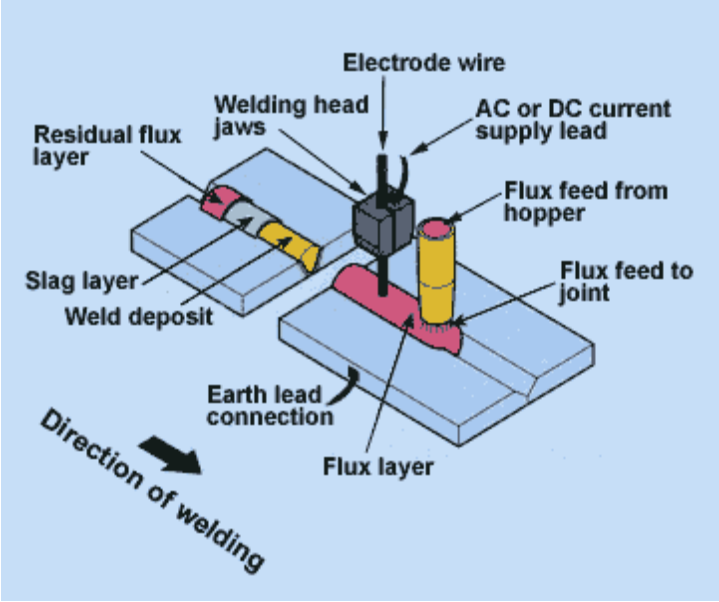

Figure 1.3. *Schematic of submerged arc welding. The melting welding electrode forms a weld pool underneath the flux layer. The heat of the forming weld pool will cause the melting of some of the flux, which will solidify as slag. The residual flux is often recycled, and the slag layer is chipped away. Figure obtained from TWI Ltd.*[43]

In arc welding, the transfer of energy from the welding apparatus to the electrode can be calculated by Equation 1.2. The efficiency factor will depend on the welding process. Heat is commonly lost through radiation, conduction, and convection.[44] SAW is generally considered one of the most heat efficient welding processes due to the protective flux layer that covers the developing weld pool, leading an efficiency factor of 0.9 to 0.99. The 1-10% heat loss is

attributed to the flux that does not melt during the welding process, which will allow some of the heat to escape.[41]

$$Q = \frac{60\eta VI}{1000v}$$

Equation 1.2. Q *is the heat input, indicated in kilojoules per inch or kilojoules per millimeters.* ***η*** *is the welding process efficiency, typically ranging from 0.22 - 0.48 for TIG to 0.9 - 0.99 for SAW.*[41] ***V*** *is the welding voltage, measured in volts.* ***I*** *is the welding current, measured in amps.* ***v*** *is the welding speed, measured in inches per minute or millimeters per minute.*[41]

In 1935, Rosenthal modeled the weld thermal cycle using a series of heat flow equations by assuming a heat source moving at a constant speed along the x axis of a fixed rectangular system.[41] The Rosenthal heat flow model depicts the melt pool geometry as a distorted half ellipsoid and is commonly used to predict the temperature cycle experienced by a point at any distance away from the center line of a weld as well as to calculate the cooling time from 800 °C (1472 °F) to 500 °C (932 °F), known as the $\Delta t_{8\text{-}5}$. It makes four key assumptions: 1) the heat flow comes from a point source 2) the thermal capacity, conductivity and diffusivity are not a function of temperature 3) there is no heat at the plate surface and 4) there is no latent heat change due to phase transformations. Although the assumptions made are not reflective of observed scientific data, it has been shown that the Rosenthal model can accurately predict the temperature distribution around a weld. The peak temperature calculated for a specific distance away from the weld centerline can give an indication of the possible microstructure. The $\Delta t_{8\text{-}5}$ is important because this temperature range is optimum for chromium carbide formation, and ferrite decomposition into sigma, chi, and other brittle phases. The formation of these unwanted phases are detrimental to the corrosion resistance as well as the toughness of the weld.[16,44–48] The time spent in the 800 °C (1472 °F) to 500 °C (932 °F) temperature range should therefore be minimized as much as possible. This can be done by controlling the heat input relative to the plate thickness.

The Rosenthal heat flow model is divided into two sets of equations: 2D heat flow for thin plate and 3D heat flow for thick plate. A diagram of the two different heat flow representations can be seen in Figure 1.4. The critical plate thickness, in which the transition from using 2D heat flow to 3D heat flow modeling occurs, can be calculated by Equation 1.3.

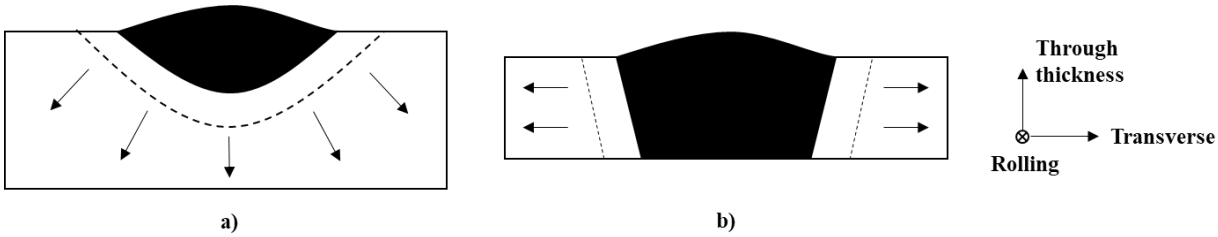

Figure 1.4. *The diagram shows the difference between 3D heat flow* ***(a)*** *and 2D heat flow* ***(b)****. The weld pool is indicated in the black, while the dotted line indicates the heat affected zone. In 3D heat flow i.e. thick plate, the weld pool does not completely penetrate the thickness of the base plate, and therefore heat can travel through the thickness, rolling, and transverse directions. Meanwhile, in 2D heat flow i.e. thin plate, the heat can only travel in the rolling and transverse directions. The figure is adapted from Easterling.*[41]

$$d_{crit} = \sqrt{\frac{Q}{2\rho C}\left[\frac{1}{773 - T_0} + \frac{1}{1073 - T_o}\right]}$$

Equation 1.3. $\boldsymbol{d_{crit}}$ *is the critical plate thickness in meters.* $\boldsymbol{Q}$ *is the heat input, in Joules per meter.* $\boldsymbol{\rho}$ *is the specific gravity in kilograms per cubic meter.* $\boldsymbol{C}$ *is the specific heat Joules per kilogram-Kelvin.* $\boldsymbol{T_0}$ *is the initial temperature of the plate in Kelvin, which can be taken as ambient temperature if no pre-heat is applied.*[45]

For 2D thin plate modeling, the peak temperature ($\mathbf{T_{peak}}$) as a function of distance (**r**) away from the weld centerline perpendicular to the welding direction can be calculated using Equation 1.4, while the $\mathbf{\Delta t_{8\text{-}5}}$ can be calculated using Equation 1.8. The temperature (**T**) as a function of time at a specified distance (**r**) away from the weld centerline perpendicular to the welding direction can be calculated using Equation 1.10. Both Equations 1.8 and 1.10 use a temperature factor, **Θ**, that can be calculated using Equation 1.6.[45] The equivalent heat flow equations for 3D thick plate modeling are given in Equations 1.5, 1.7, 1.9, and 1.11.[44] The variables used in the heat flow equations are defined in the following manner: $\mathbf{T_0}$ is the initial

temperature of the plate in Kelvin, which can be taken as ambient temperature if no pre-heat is applied. **Q** is the heat input, in Joules per meter. **d** is the base plate thickness. **ρ** is the specific gravity of the base material in kilograms per cubic meter. **C** is the specific heat of the base material in Joules per kilogram-Kelvin. **r** is the distance from the weld center line perpendicular to the welding direction in meters. **λ** is the thermal conductivity, given in Joules per meter-seconds-Kelvin.[41,44,45]

Table 1.2. *Rosenthal heat flow equations and the calculated parameters*

Calculated Parameter	2D Thin Plate	3D Thick Plate
Peak temperature (**T_{peak}**) in Kelvin as a function of distance (**r**) from the weld centerline	**Equation 1.4**: $T_{peak} - T_0 = \sqrt{\frac{2}{\pi e}} \frac{Q}{2d\rho C r}$	**Equation 1.5:** $T_{peak} - T_0 = \frac{2Q}{\pi e \rho C r^2}$
Temperature factor to be used in Equation 1.8 – 1.11	**Equation 1.6:** $\frac{1}{\Theta} = \frac{1}{(773 - T_0)^2} - \frac{1}{(1073 - T_0)^2}$	**Equation 1.7:** $\frac{1}{\Theta} = \frac{1}{(773 - T_0)} - \frac{1}{(1073 - T_0)}$
Cooling time in seconds from 800 °C (1472 °F) to 500 °C (932 °F) i.e. the **Δt_{8-5}**	**Equation 1.8:** $\Delta t_{8-5} = \frac{Q^2}{4\pi\lambda\rho C \Theta d^2}$	**Equation 1.9:** $\Delta t_{8-5} = \frac{Q}{2\pi\lambda\Theta}$
Instantaneous temperature (**T**) at a given time at a specific distance (**r**) away from the weld centerline, given in Kelvin	**Equation 1.10:** $T - T_0 = \Theta \sqrt{\frac{\Delta t_{8-5}}{t}} e^{\frac{-\Theta^2 \Delta t_{8-5}}{2et(T_{peak} - T_0)^2}}$	**Equation 1.11:** $T - T_0 = \frac{\Theta \Delta t_{8-5}}{t} e^{\frac{-\Theta \Delta t_{8-5}}{et(T_{peak} - T_0)}}$

In a recent study by Poorhaydari et al., a model was developed for the weld plates of intermediate thicknesses. The thermal cycle of real welds has been determined by research to lie in between the two limiting sets of parameters given by Rosenthal. Thus, to determine the so-called 2.5D solution, the HAZ boundaries are used to determine the weighting factor. However, both the Rosenthal heat flow model and the model developed for intermediate plate thicknesses

are developed for bead on plate or autogenous welding and thus can only be used to get a first approximation of the weld thermal cycle, which is sufficient for the estimation of the effects of the weld heating and cooling cycle on the microstructure of both the weld fusion zone and the HAZ zone.[44]

Another important parameter that must be defined for a multiple pass welding procedure is the maximum interpass temperature. The maximum interpass temperature is the temperature below which the weld plate must cool to before a subsequent weld pass can be laid and is measured at the weld centerline at the beginning of the weld. This means that during all subsequent weld passes, the weld plate (i.e. the preheat) will be between room temperature and the maximum interpass temperature. The lower the maximum interpass temperature, the longer a welder must wait before laying a subsequent welding pass, increasing fabrication time and thus the overall cost of the welding procedure.

1.4 Effects of Welding Wire Geometry

There are three main types of welding consumable: 1) flux covered 2) flux cored or metal cored and 3) solid. The first type of filler wire involves a solid wire with an outer coating of flux. The second type of filler wire involves a tubular wire surrounding a mixture of various powders. For flux cored wires, the powder is a mixture of various metal oxides and silicates that aid in the stabilization of the arc. Metal cored wire similarly involves an outer metallic sheath, but the powder mixture inside is mainly composed of alloying elements.[41] The simplest tubular wires are produced by first forming the outer steel strip into a curved U profile. The outer metallic sheath is then filled with fluxing, deoxidizing, and/or alloying powders. The sheath and powder are then closed to round tube, drawn down to the final electrode size, and baked to remove any residual drawing lubricant.[49]

Various studies have shown the advantages that come from using a tubular filler wire construction when welding. In a study by Prajapati and Badheka, it was found that for single V-groove welding, there is a negligible trend found in the tensile testing data when comparing a flux cored wire, a metal cored wire, and a solid wire. However, the flux cored wire showed significantly higher impact energies for both the weld and HAZ Charpy V-notch (CVN) impact testing. This was hypothesized to be due to the double shielding by both the shield gas as well as the flux core of the flux cored wire, which will minimize the formation of precipitate phases. Both of the tubular wires showed a lower peak temperature measured at the center of the weld. This resulted in a smaller distortion angle.[50] Similar results were found in another study when using metal cored wire.[51]

The advantages of the tubular wires come from the electrical conductance path. Because the current will find the path of least resistance, it travels mainly through the metallic sheath. This leads to an overall higher current density for the same electrical input in a metal cored or flux cored wire when compared to a solid wire of the same diameter, resulting in a higher power per area being delivered at the tip of the filler wire and thus a higher melting rate, as shown in Figure 1.5.[49,52–54] This difference in current path leads to a differing dominating metal transfer path. In the case of the tubular wire, the molten metal will be transferred to the weld pool by spray type transfer, as opposed to the globular transfer typically seen with the solid wires.[49]

The spray type metal transfer leads to metal cored wires' smoother transfer, high deposition efficiency and rate, high duty cycle and travel, and low spatter, slag, and fume generation. Metal cored wires have a deposition efficiency of 92-98%, while solid wires tend to have a deposition efficiency of 95-98%. The deposition rate, given in pounds per hour or kilograms per hour, for 0.045" tubular wires (flux and metal cored) was found to be twelve to

fourteen pounds per hour compared to the eight to ten pounds per hour for solid wires. This higher deposition rate would allow for fewer welding passes for the same geometry, resulting in faster fabrication. Although both solid and flux cored wires can have a high duty cycle (the amount of continuous arc time, affected by the travel speed, equipment, amount of time for slag removal, and the ability to easily replenish the consumable), only metal cored wires have been shown to have a high duty cycle when combined with a high travel speed without sacrificing bead appearance, penetration, and weld integrity. The low spatter, slag, and fume generation are due to the arc stabilizers that are used in the metal cored wire along with the alloying powder. This leads to a safer work environment for the welder and can reduce the amount of safety equipment necessary during welding.[49,52–54]

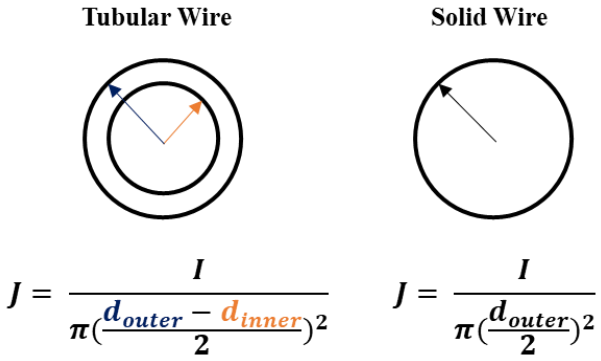

Figure 1.5. *Diagram indicating the difference of the current path between the tubular wire and solid wire. The current density (J) is determined by the current (I) divided by the cross-sectional area in which the current flows through. The tubular wire shown here represents the simplest construction with no overlap of the outer sheath. With a more complex metallic sheath construction, the current density would approach that of the solid wire. The figure is adapted from Select Arc Inc.*[41]

1.5 Research on the Welding of 3CR12

Research on the welding of 3CR12 has shown that the use of austenitic stainless steel filler wire materials is preferred over the use of a matching filler material, due to problems with cracking of the welds.[9,55] Gooch and Davey found that crack-free welds can be made using AISI

309, 309L, and 310. The mechanical properties of the weld were found to be comparable to the base plate, and adequate fusion weld ductility was found through bend testing. Hoffman similarly found that any austenitic filler wire is sufficient for the welding of 3CR12, but AISI 308, 309L, and 309LMo are preferred. This is due to the fact that 309 has a higher capacity for dilution without forming crack-sensitive microstructure, specifically martensite. Pagani performed fatigue and electrochemical testing on a matching filler wire to 3CR12, making it theoretically both mechanically and electrochemically compatible. However, the strength of the weld was found to be significantly higher than that of the base material because the fusion zone was predominantly martensite.[9]

The welding of 3CR12 results in the development of three distinct microstructural regions. The first region is the narrow coarse-grained high temperature HAZ (HTHAZ), which is characterized by ferrite grains and granular blocky angular Widmanstätten intergranular martensite. The next region is a duplex region characterized by fine grained ferrite and untempered intergranular and intragranular martensite. The phase composition will vary across width of zone. The last region is the low temperature HAZ (LTHAZ), which shows no change in hardness due to the previous heat treatment, specifically the hot rolling. The widths of these regions are mainly a function of the composition and heat input. The HTHAZ is cause for the most concern because of the large grain size leading a low fracture toughness (the ability of a material with a crack to resist fracture)[46] and due to its high potential for high temperature embrittlement due to the ferrite content.[9]

In his Ph.D. dissertation, Grobler focused his testing on mechanical tests that induces a triaxial stress state at the fusion line, whereas the previous studies focused on plane stress testing, using bend and tensile testing. He hypothesized that if the degree of constraint increased, then

the effect of narrow coarse HTHAZ would also increase. With the addition of a triaxial stress state, premature brittle fracture may occur. Using three-point face bend tests with the bend radius equal to the plate thickness for bead on plate welds, Grobler determined that the use of 316L allows for a full 180° bend when used with tempered 3CR12, while the matching 3CR12 filler wire only allowed for a bend of 9° when used to weld hot rolled 3CR12. Although the HTHAZ toughness is low, the deformation predominantly occurred either in the tempered base material or in the fusion zone when an austenitic filler wire was used. When the matching filler was used, cracks appeared in the coarse grained HAZ adjacent to the fusion line. This was determined to be due to the higher strength weld imposing higher amount of constraint.[9]

In order to test the fusion line toughness, Grobler created a fusion line notch fracture toughness test, shown in Figure 1.6.a), that include an artificial through-thickness crack. The samples were tested in tension at room temperature to obtain a load vs crack opening displacement curve. The samples were shown to fail in one of four ways, shown in Figure 1.6.b). Fracture modes 1 and 2 both occur by cleavage fracture in the HTHAZ. Fracture mode 3 involves the cleavage fracture in one of the HTHAZ and ductile tearing of the weld metal of the second fillet weld. Fracture more 4 occurs by the ductile tearing of both fillet welds. The samples welded with 309L and 316L failed by fracture mode 3 and 4 at the low heat input i.e.1.2 kJ/mm (30.5 kJ/in) and fracture mode 4 at the high heat input i.e.1.4 kJ/mm (35.6 kJ/in). The samples welded with 308L failed by fracture mode 3 at the low heat input and fracture mode 2 at the high heat input. The samples welded with E3CR12 failed by fracture 1 and 2, regardless of heat input. Microstructural analysis of the weld fusion zones determined that fracture modes 1 and 2 occurred when the fusion zone contained. The critical dilution values were determined by using the typical chemical compositions and the Schaeffler diagram, and were found to be 43%, 27%,

16% and 0% for 309L, 316L, 308L, and E3CR12 respectively. Thus, 309L filler metal is recommended for the welding of 3CR12 in high integrity structural applications due to its higher dilution capabilities.[9]

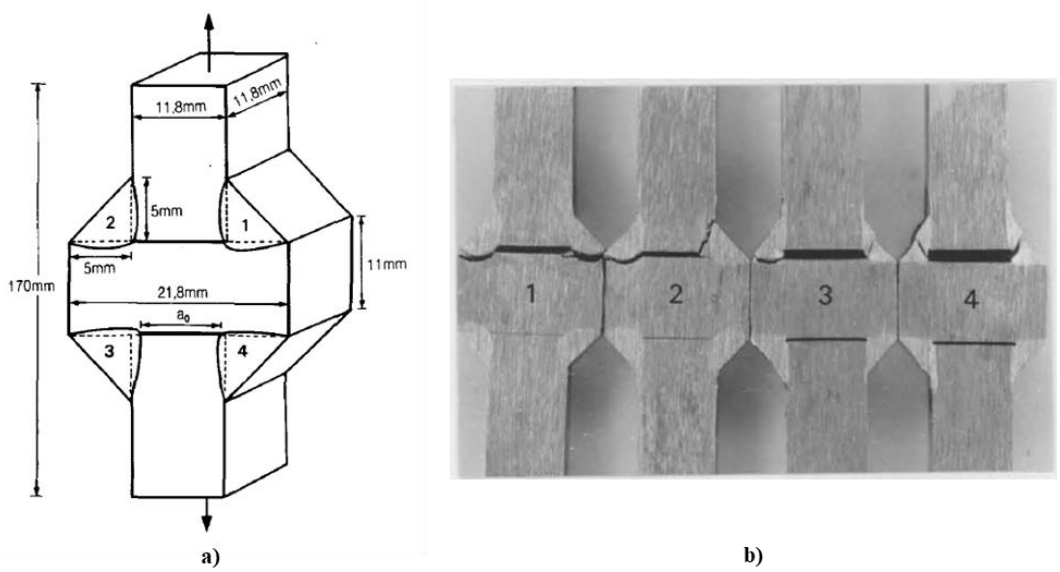

Figure 1.6. a) *The diagram shows the dimensions of the fusion line notch fracture toughness (FLNFT) sample. The four different filler wires (AISI 308L, 309L, 316L, and E3CR12) were used to shielded metal arc weld the fillet welds. The heat inputs used were 1.2 kJ/mm (30.5 kJ/in) and 1.4 kJ/mm (35.6 kJ/in) to represent a low and high. This sample was pulled in tension and a load vs crack opening displacement curve was determined.* ***b)*** *The four fracture modes observed using the FLNFT sample. Fracture modes 1 and 2 both occur by cleavage fracture in the HTHAZ. Fracture mode 3 involves the cleavage fracture in one of the HTHAZ and ductile tearing of the weld metal of the second fillet weld. Fracture more 4 occurs by the ductile tearing of both fillet welds. The figures are obtained from Grobler.*[9]

1.6 Austenitic Filler Solidification

The microstructure present after welding stainless steel is commonly predicted by using one of various constitution diagrams (Schaeffler[29], DeLeong[30], or WRC-92[28]), which plots the Cr_{eq} vs the Ni_{eq} values of the base and filler wire materials. The main difference between them is the elements and corresponding coefficients used for the calculation of the Cr_{eq} and the Ni_{eq}. The various equations can be seen in Table 1.3.

Table 1.3. *Various constitution diagrams commonly used to predict the welded microstructure of stainless steels and the equations used to calculate the Cr_{eq} (x axis) and the Ni_{eq} (y axis). The bolded items in the equations indicate the wt% of the phase stabilizing element.*

Constitution Diagram	Cr_{eq}	Ni_{eq}
Schaeffler[29]	Cr_{eq} = **Cr** + **Mo** + 1.5**Si** + 0.5**Nb**	Ni_{eq} = **Ni** + 30**C** + 0.5**Mn**
DeLong[30]	Cr_{eq} = **Cr** + **Mo** + 1.5**Si** + 0.5**Nb**	Ni_{eq} = **Ni** + 30**C** + 30**N** + 0.5**Mn**
WRC-92[28]	Cr_{eq} = **Cr** + **Mo** + 0.7**Nb**	Ni_{eq} = **Ni** + 35**C** + 20**N** + 0.25**Cu**

Austenitic filler metals often solidify according to one of four different pathways, shown in Figure 1.7. The solidification pathway is dictated by the balance of austenite and ferrite stabilizers, commonly expressed as the Cr_{eq}/Ni_{eq} value. For low Cr_{eq}/Ni_{eq} value, the *A* mode dominates and is characterized by complete austenitic solidification from the liquid phase. As the Cr_{eq}/Ni_{eq} value increases, the *AF* case allows for the formation delta (δ) ferrite forms in the Cr rich and Ni depleted inter-dendritic regions during the final stages after an initially austenitic driven solidification. As the Cr_{eq}/Ni_{eq} value continues to increase, the primary solidification phase transitions from austenite to δ ferrite, and the δ-ferrite becomes increasingly stable.[26,56,57] This value was determined by Hammar and Svensson (using Cr_{eq} = **Cr** + 1.37**Mo** + 1.5**Si** + 2**Nb** + 3**Ti**; Ni_{eq} = **Ni** + 0.31**Mn** + 22**C** + 14.2**N** + **Cu**) to be 1.55.[57] This value was verified by Suutala and Moisio, and Suutala. *FA* cases begin the solidification as δ-ferrite with the austenite growing as the terminating phase. Finally, *F* cases complete the solidification process as δ ferrite, and the solidification microstructure remains stable down to room temperature due to the high amount of ferrite stabilizers relative to the austenite stabilizers. In the *AF and FA* modes, the δ-ferrite that is formed is thermodynamically unstable at low temperatures and will tend to undergo a solid-state phase transformation to austenite during cooling to room temperature. Thus, designed to mainly solidify in the *FA* or *AF* modes, the use of austenitic filler wires will result in

a fusion zone that is primarily austenitic with residual delta ferrite in a combination of vermicular, acicular, or lathy morphologies.[26,56,57]

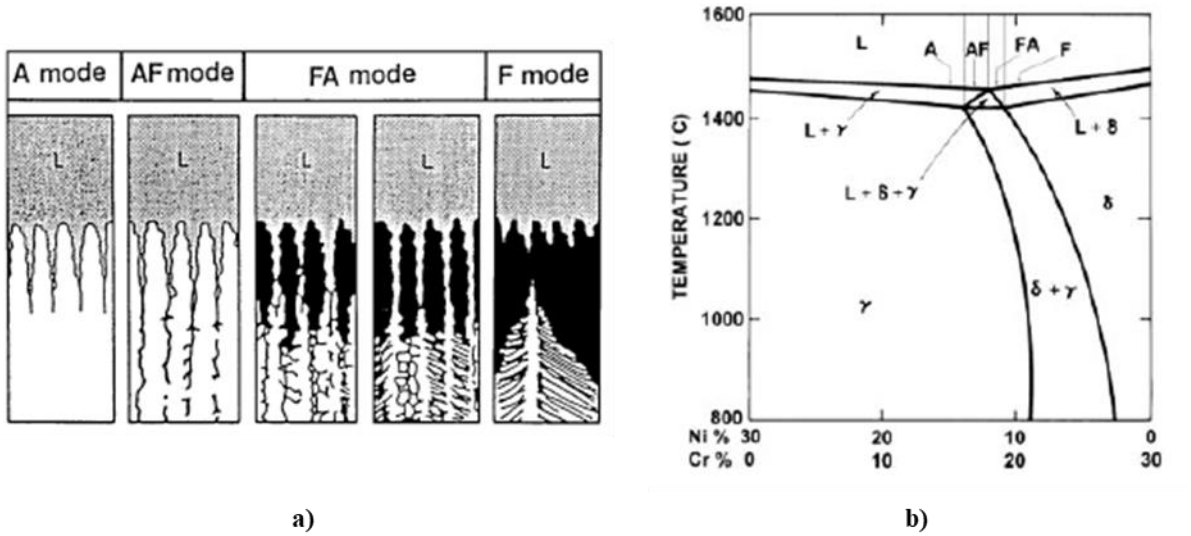

Figure 1.7. a) *The diagram shows the four pathways for austenitic filler wire solidification. The white phase represents austenite, while the black phase represents delta (δ) ferrite. The solidification mode is dictated by the balance of austenite and ferrite stabilizers.* ***b)*** *The phase diagram is a pseudo-binary of the ternary Fe-Cr-Ni phase diagram at 70 wt% Fe, which shows the location of the four different solidification modes. The figures are obtained from Shankar et al.*[57]

Electron backscattered diffraction (EBSD) within a scanning electron microscope (SEM) has enabled both the phase (crystal structure) and crystal orientation of the phases to be determined. Using EBSD, it has been shown that despite microstructures with radically distinct morphologies, the austenite and retained ferrite regions present in both *F* and *FA* type welds are crystallographically related to each other through the Nishiyama-Wasserman (NW) or Kurjdumov-Sachs (KS) orientation relationships.[58] If *FA* type, the weld metal has a dendritic appearance with δ-ferrite residing in the inter-dendritic regions. If the weld metal solidifies following the *F* or *FA* pathway, the solidification structure will be large (here denoted prior δ-ferrite) grains, which largely transform into austenite having a basket-weave (Widmanstätten) type microstructure during cooling.

1.7 Potential Problems Due to Welding

When performing a butt weld, various types of distortions can occur. From the through-thickness view, longitudinal and transverse shrinkage can occur causing a rectangular welded plate to approach a bow-tie shape. The welded plate can also bow outward. Lastly, the plate can show angular distortion, best observed when looking down the length of the weld. This causes the butt welded plate to no longer be flat and approach a V shape.[41] Other welding related defects include different types of cracking (related to the solidification of the various zones, the thermal cycle, and/or the presence of hydrogen), welding process control issues (lack of fusion, undercutting or excessive over-beading, incomplete penetration, porosity, and slag inclusions), and geometric defects (poor design or fit up).[59] These types of processing defects are commonly tested for by liquid penetration or ultrasonic testing.[60,61]

Because the goal for the use of dual phase steels, such as 50CR, is for the construction of maintenance-free bridges, microstructural analysis of the welds is important to explain the observed performance of the welded structures and, perhaps more importantly, to determine if any issues may arise after the initial erection of the bridge.[40] Welding leads to the formation of least three distinct microstructural regions: the fusion zone, the HAZ, and the base material. The fusion zone is a mixture of the base material and the filler wire and is characterized by the level of dilution experienced by the filler metal. Many factors can affect the dilution, including the type of filler wire, heat input, maximum interpass temperature, number of passes, and type of welding technique.[48,62] The dilution consequently affects the phase content of the fusion zone by changing balance of the austenite and ferrite stabilizers.[25–30]

It is well established that welds which only contain the austenite phase (i.e., less than about five vol.% residual δ ferrite) are prone to hot-cracking.[16,57,63] After the discovery of this problem, Sherer et al. determined that austenitic welds that contain 5 - 35 vol% residual δ-ferrite

typically will not hot crack, and thus since 1941, the problem of hot cracking in austenitic welds has essentially been eliminated. This is presumably due to the higher solubility of the δ-ferrite phase for tramp elements like sulfur (S), phosphorus (P), boron (B), silicon (Si), titanium (Ti), and niobium (Nb), which are associated with solidification cracking due to the formation of brittle phases or low melting temperature grain boundary constituents that cause shrinkage stresses, which can lead to cracking.[16,57,63] However, Masumoto et al. suggested that it was not in fact the presence of ferrite, but the primary solidification mode that was the dominating factor in hot cracking prevention. This is supported by the literature review performed by Kujanpaa et al.[57] and data compiled by the American Welding Society (AWS)[26], shown in Figure 1.8.

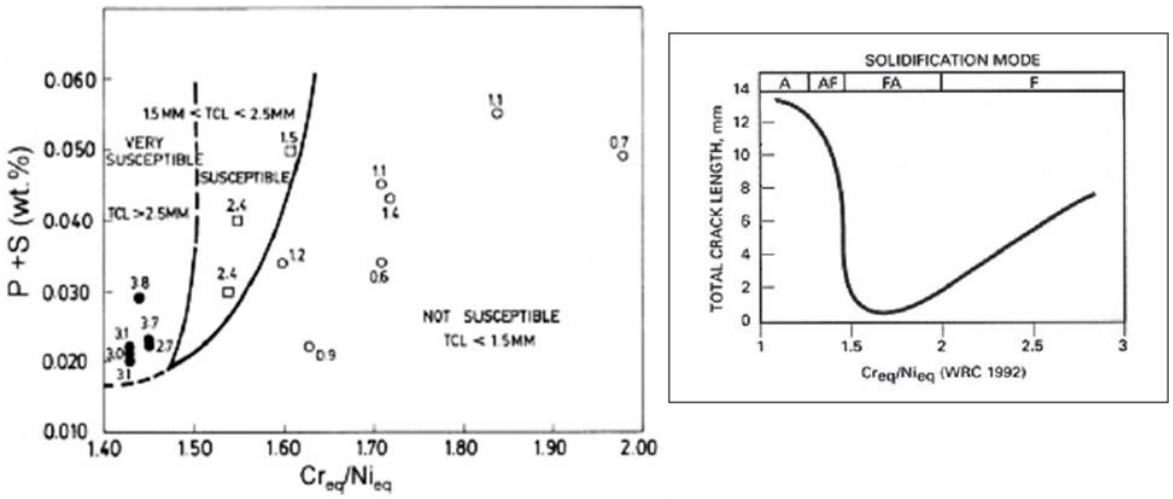

Figure 1.8. a) *The diagram plots the Cr_{eq}/Ni_{eq} obtained using Hammar and Svensson's equations against the wt% of the main impurity elements that tend to cause hot cracking. It can be seen that the austenitic weld should not be susceptible to hot cracking if the Cr_{eq}/Ni_{eq} is greater than 1.6 and/or the combined P+S wt% is less than 0.015 wt%. The figure was obtained from Shankar et al.*[57] ***b)*** *The diagram plots the Cr_{eq}/Ni_{eq} obtained using the WRC-92 equations against the crack length found after welding. It can be seen that the crack length is minimized when the Cr_{eq}/Ni_{eq} is between about 1.5 and 2. This seemingly corresponds to the FA solidification mode. The figure was obtained from Mateša et al.*[26]

It is a matter of controversy as to whether levels of residual δ-ferrite higher than five vol% result in lower mechanical properties of austenitic welds or if they simply have no

effect.[16,29,57,64,65] Embrittlement of austenitic stainless steels has been known to occur due to the decomposition of the residual ferrite phase at elevated temperature applications or from thermal cycling. This is due to the formation of brittle phases, such as the sigma, chi, and G phases (promoted by high amounts of Cr and Mo), as well as due to the spinodal decomposition into a Cr-rich and Fe-rich phase (termed 475 °C embrittlement), which have a deleterious effect on the mechanical properties.[16,43,48,66] It has been shown that both the increasing vol% of sigma phase (more susceptible with increasing ferrite vol%) as well as 475 °C embrittlement (more pronounced with increasing Cr wt%) cause a dramatic decrease in the toughness of austenitic welds. Strong reductions in weld toughness and increases in the ductile to brittle transition temperature (DBTT) have been observed for austenitic welds of a martensitic stainless steel, with increasing ferrite content.[64] However, it has also been shown that only very high (> 50 vol%) residual δ-ferrite contents are correlated with strong reductions in the toughness of a lean, duplex stainless steel.[65] This wide range of observations suggests other factors, such as fusion zone microstructure morphology may have an even more important and controlling influence than simply residual δ-ferrite content.

1.8 Weld Quality Testing

During bridge girder fabrication, a variety of tests must be performed on 1” thick welded plate known as the procedure qualification record (PQR), set forth by AASHTO/AWS D1.5, to ensure that the welding procedure performed will not cause any catastrophic failures of the components. The PQR test suite includes uniaxial tension, bend, and Charpy V-notch (CVN) impact testing. [61] Tensile testing involves putting a sample in pure tension i.e. with no shear stresses applied and measuring the strain response to the stress applied, graphically shown in a stress-strain curve. For the purposes of quality control, tensile testing will typically yield three values: yield strength, tensile strength, and percent elongation, correlated to a specific gage

length.[67] However, other material properties, such as the elastic modulus and the strain hardening exponent, can also be obtained and are useful for the characterization of the material.[68]

Bend testing features the bending of the weld over a circular jig with the goal of achieving a 180° bend.[61] This ensures that the weld has sufficient ductility, typically about 20% elongation as a minimum, as well as proper fusion.[65,69] Because the outside of the bend undergoes high amounts of plastic deformation, any embrittlement or physical gaps due to poor welding will be revealed.[69]

CVN testing can identify the DBTT of a material as well as its impact energy at a given temperature. The DBTT commonly manifests as a rapid drop in the impact energy as a function of temperature in body centered cubic (BCC) materials (in the case of steel, the ferrite and martensite phases), but not in face centered cubic (FCC) materials (the austenite phase), shown in Figure 1.9. This is due to a more temperature sensitive stress yield strength in the body centered cubic crystal structure.[70] This difference is due to the behavior of the slip systems in the BCC material system when compared to the FCC material system. In FCC, the slip systems are of the <110> {111} family, resulting in twelve unique slip systems. In BCC, the slip direction is <111> but the slip plane can be either {110}, {112}, or {123}, leading to a total of forty-eight slip systems. However, as the temperature decreases, access to some of these slip systems are hindered, thus causing the occurrence of the DBTT in BCC materials. The DBTT is commonly determined by one of three ways: 1) the inflection point of the hyperbolic tangent curve, which corresponds to 50% probability that the fracture will be ductile and 50% that it will be brittle 2) the temperature at which a specific impact energy occurs (usually 30J) 3) the temperature at which point no cleavage fracture can be seen using the SEM.[3,71] Because brittle fractures occur rapidly with little deformation, this type of fracture should be avoided.[68]

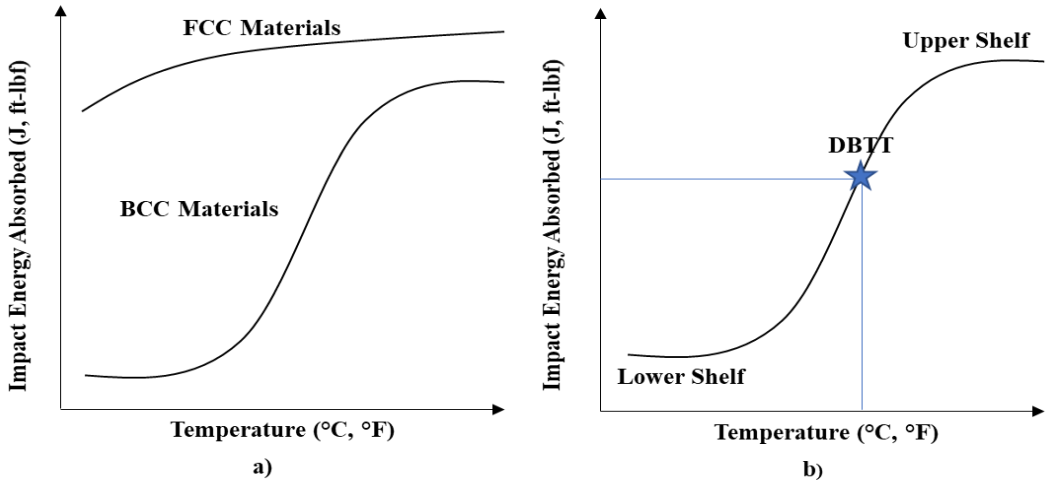

Figure 1.9. a) *Figure shows the typical transition temperature curves for face centered cubic (FCC) and body centered cubic (BCC) materials. It can be seen that the transition temperature curve for BCC materials follows a hyperbolic tangent curve, while the FCC curve does not exhibit the same dramatic drop in impact energy.* ***b)*** *The transition temperature curve for BCC materials can be broken down into three regimes: the upper shelf, the transition region, and the lower shelf. The DBTT is typically taken as the inversion point of the hyperbolic tangent curve, the temperature corresponding to a specific impact energy, or the temperature at which the fracture surface appears to be 50% ductile and 50% brittle (FATT). The figures were adapted from Dieter.*[68]

The measured impact energy, given either in Joules (J) or foot-pound force (ft·lbf) is an indication of a material's fracture toughness, the measure of its ability to resist fracture in the presence of a crack or notch.[70] CVN samples are commonly tested both in the longitudinal (LT) and transverse (TL) orientations. LT samples are machined parallel to the rolling direction with the V notch placed in the transverse direction. TL samples are machined perpendicular to the rolling direction with the notch placed in the longitudinal direction. These orientations can be seen in Figure 1.10.

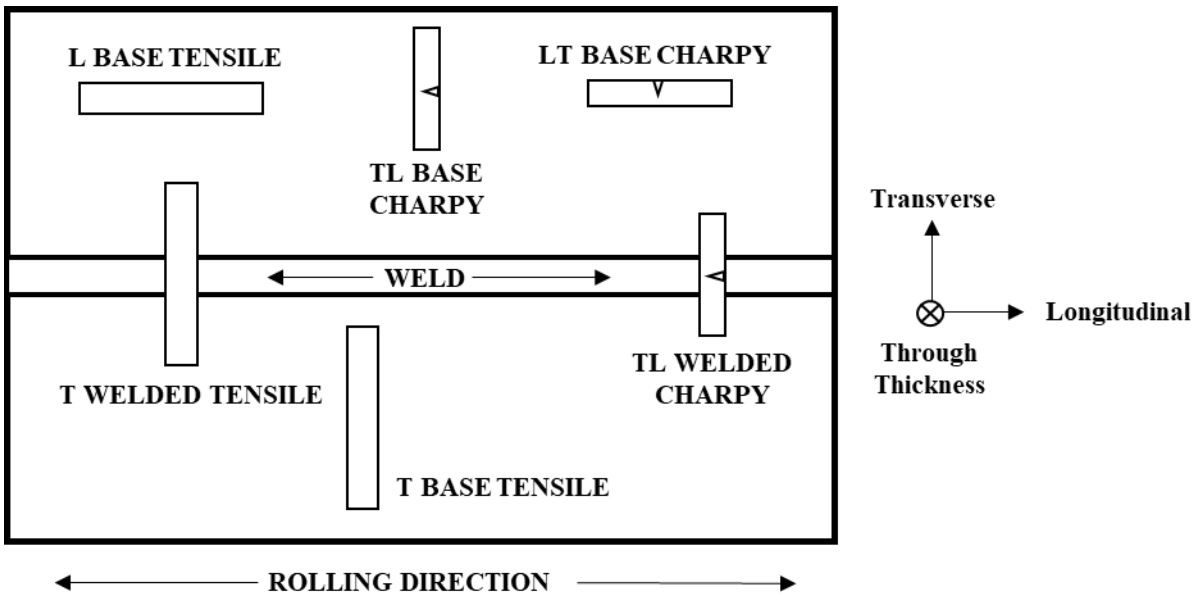

Figure 1.10. *Schematic illustration of different types of sample and their orientations with reference to a coordinate system defined by the L (longitudinal/rolling), and T (long transverse), and S (short-transverse) directions. The welding can also be performed perpendicular to the rolling direction. In that case, the diagram would be rotated 90°and the T(L) samples would be L(T) and vice versa.*

1.9 Research and Thesis Layout

Work performed by the Oregon DOT established the use of Lincoln Electric ER309L filler wire as the most common procedure for the fabrication of 50CR bridge girders. The Oregon study used a heat input of 55 kJ/in and maximum interpass temperatures of 225, 300, 400, and 450 °F on 1" thick plate. The welds performed within any combination of these welding parameters were observed to pass the mechanical property requirements set by AASHTO/AWS D1.5.[72] Given that the interpass temperatures used here exceed the manufacturers recommendations for maximum interpass temperature of 210 – 225 °F, the actual limits remain undetermined.[73,74] Data referred to in the Oregon study also showed that successful welding has been performed using up to 70 kJ/in for 1" thick plate.[73] Increasing the limits on the maximum interpass temperature and the heat input can lead to a greater fabrication efficiency and lower

overall cost, but could cause detrimental effects to the mechanical properties, such as a loss in strength and/or impact energy due to changing microstructure.

The purpose of this project was to 1) gain a deeper understanding of the 50CR alloy system 2) determine if a higher heat input combined with the maximum interpass temperature up to 450 °F could be used when welding 50CR, and 3) evaluate several filler wire alloys and geometries for the use of plate girder fabrication. Although the one of the producers of 50CR (ArcelorMittal) recommends for the use of ER308L, ER309L, ER316L, and their higher silicon content counterparts,[74] ER309L has by far been the most widely used filler wire used for welding 50CR plate girders.[75] To address these three areas, discussion with industry experts, a literature review, compositional testing, metallurgical analysis and mechanical testing were all performed. Three groups of welded 50CR plates were tested. Group 1 contained sixteen 1/2" thick plates, which were received in two batches. Group 2 contained twelve 1" thick plates, and Group 3 contained two PQR plates prepared and tested according to AASHTO/AWS D1.5. All of the 50CR plates were welded at a traditional bridge fabrication shop. When applicable, testing was performed in compliance with the appropriate ASTM or AASHTO/AWS standard.

The results of this study have led to the hypothesis that it is not the absolute phase fraction of retained δ-ferrite that is most critical. Rather, it is the scale and morphology of the microstructure which must be controlled in order to avoid embrittlement of the weld fusion zone.

Chapter 2: Characterization and Testing of the Base Material and the Filler Wires

2.1. Introduction

The ASTM A709 grade 50CR (where the CR indicates improved corrosion resistance) used in this study was provided by ArcelorMittal. According to ASTM A709, both grade 50W (the conventional weathering steel) and 50CR must meet a minimum yield strength of 50 ksi, a minimum tensile strength of 70 ksi, and a minimum percent elongation of 21%.[37] 50CR must also surpass a minimum impact energy of 15 ft·lbf at the test temperature indicated by ASTM A709 defined by the temperature zones indicated by the AASHTO LRFD (load and resistance factor design) Bridge Design Specifications.[37,76] The materials used in this study were 1/2" and 1" thick. The 1/2" thick 50CR came from two separate melts, while all of the 1" material came from one melt. According to communications with ArcelorMittal, all of the 50CR plates for bridge applications are rolled from 9" thick by 85" wide slabs. This leads to an 89% reduction for the 1" thick plates and 94% reduction in the 1/2" thick plates. Similar to 3CR12, 50CR is hot rolled in the ferrite-austenite region. As the hot rolling proceeds, the plate is continuously cooling. As the plate is cooled to room temperature, the austenite transforms into martensite.

Ten filler wire manufacturers and distributers were contacted to find filler wires appropriate for submerged arc welding of 50CR. Factors that were considered include: alloy recommendations by the plate producer, country of origin, cost, availability, and lead time. At the time of the project initiation, the 309L, 309LSi, and 316L used in this study did not meet the Buy America requirements for federally funded projects.[77,78] The Buy America regulation states that only a maximum of "0.1% of the total contract or $2,500, whichever is greater" can be allocated towards the purchasing of foreign ferrous materials for federally aided projects. This

means that the material used must be manufactured within the U.S. and its territories, from initial smelting to final packaging.[77] Of the companies contacted, the majority of the stainless steel filler wires were made in Europe, and thus a special waiver would need to be obtained by the state DOT building a 50CR bridge in order for those filler wires to be used. Fortunately, a metal cored wire, 309LC, met the regulation. Although the Buy America regulation was not a primary concern for this project, it must be taken into consideration for the future implementation of this research toward the realization of 50CR bridges.

Four different 3/32" in filler wires were ultimately selected: ER309L (309L), ER309LSi (309LSi), and ER316L (316L) solid welding wire provided by The Lincoln Electric Company, and ER309L metal cored welding wire (309LC) by Select Arc Inc. The three distinct compositions are listed in Table 2.1.

Table 2.1. *Nominal compositions of the filler wires used in this study per the AWS requirements. The singular values indicate the maximum allowed.*

Element	ER309L[79]	ER309LC[80]	ER309LSi[79]	ER316L[79]
C	0.03	0.03	0.03	0.03
Cr	23.0 – 25.0	23.0 – 25.0	23.0 – 25.0	18.0 – 20.0
Ni	12.0 – 14.0	12.0 – 14.0	12.0 – 14.0	11.0 – 14.0
Mo	0.75	0.75	0.75	2.0 – 3.0
Mn	1.0 – 2.5	1.0 – 2.5	1.0 – 2.5	1.0 – 2.5
Si	0.30 – 0.65	0.30 – 0.60	0.65 – 1.00	0.30 – 0.65
P	0.03	0.03	0.03	0.03
S	0.03	0.03	0.03	0.03
Cu	0.75	0.75	0.75	0.75

Characterization of the base material included microstructural and compositional analysis as well as mechanical testing. Characterization of the four filler wires types involved using the scanning electron microscope (SEM) to observe the microstructure and the distribution of elements present. Emission, combustion, and electron dispersive spectroscopy (EDS) along with X ray diffraction (XRD) were used to determine the composition. Whenever possible, the testing followed the corresponding ASTM standard. These methods are detailed below.

2.2. Experimental Procedure

2.2.1 Compositional Analysis

Compositional analysis was performed on a 1" x 1/2" x 1/2" sample of the 50CR base plate from Group 1 (1/2" thick) in accordance with ASTM E1019[81] and ASTM E1479[82] by Applied Technical Services Inc. To corroborate the external testing, three samples were taken from the both batches of Group 1 (1/2" thick), from Group 2 (1" thick) and from Group 3 (1" thick). The samples were then cut and polished to a finish of 1200 grit and analyzed using a benchtop Panalytical Epsilon 3x energy dispersive X-ray Fluorescence (XRF).

Inch-long filler wire samples of 309L and 309LC were analyzed in accordance with ASTM E1019[81] and ASTM E1479[82] by Applied Technical Services Inc. and Luvak Inc. The composition of the 309L, 309LSi, and 316L solid filler wires was estimated by averaging at least five semi-quantitative EDS area scans in the Quanta 650 SEM.

2.2.2 Microstructure Predictive Analysis

The 50CR composition determined by Applied Technical Services Inc. was used to predict the microstructure in the 50CR by applying the Kaltenhauser Equation, Equation 1.1, as well as by plotting the Cr_{eq} and Ni_{eq} values on the Schaeffler and Balmforth constitution diagrams, shown in Figure 2.1. A Schaeffler diagram Excel spreadsheet, made by Kevin Millican and obtained from an open source website, was used to accurately plot the Cr_{eq} and Ni_{eq} for 50CR. Using multiple linear regression analysis on the alloying elements from the Kaltenhauser Equation and the ferrite content obtained using the point counting method, Equation 2.1 was developed by Balmforth and Lippold.[24] The average of the two sets of data for the 309L and 309LC filler wires as well as the EDS data for the 309LSi and 316L filler wires were inputted into the Schaeffler diagram spreadsheet.

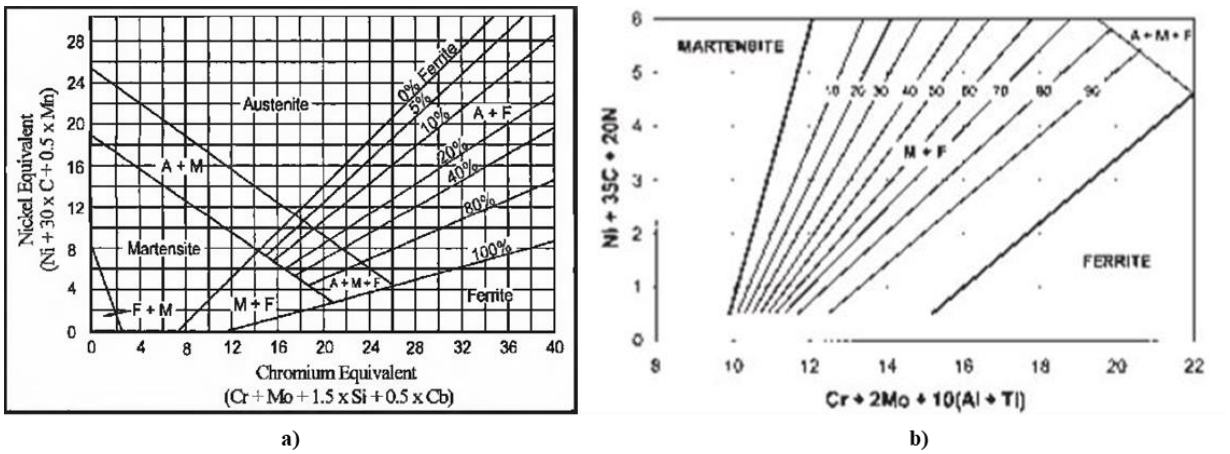

a) b)

Figure 2.1. a) *The Schaeffler diagram was developed by plotting the previously published data on the use of austenitic stainless steel filler wires for dissimilar metal welding. This data included data published in papers as well as other early constitution diagrams.*[4,30] ***b)*** *The Balmforth diagram combines the Lippold diagram, which used the alloying element factors from Kaltenhauser and microstructural data obtained from Lefevre et al., and the new microstructural data obtained from analysis of button melted samples. The figures were obtained from Balmforth and Lippold.*[7]

$$F\% = -109 + 14.3(Cr + 2[Si + Mo] + 9[Al + Ti]) - 21.7\ (Ni + 20C + 10\ N + 0.3\ Mn)$$

Equation 2.1. F% *is the volume percentage of ferrite in the ferritic-martensitic microstructure, while* ***Cr****,* ***Si****,* ***Mo****,* ***Al****,* ***Ti, Ni****,* ***C****,* ***N****, and* ***Mn*** *are the weight percent of chromium, silicon, molybdenum, aluminum, titanium, nickel, carbon, nitrogen, and manganese respectively.*

2.2.3 Microstructural Analysis

Samples were obtained from the planes parallel to the longitudinal (L), long-transverse (T), and short-transverse (S) directions, shown in Figure 2.2, from each group of 50CR plates received. These samples were then ground and polished to a 0.05-micron finish and etched using Vilella's reagent, prepared in accordance to ASTM E407.[83] This contained 25 mL 4 v/v% picric acid (equivalent to 1 g of picric acid), 5 mL hydrochloric acid, and 75 mL of ethanol. Microstructural analysis was performed using a Hirox RH-8800 optical microscope (OM). Micrograph processing using ImageJ was then used to determine the ferrite volume fraction. OM micrographs were converted to a binary black and white 2D image, by thresholding the gray scale image to have the ferrite appear as white and the martensite black. The pixels of the ferrite

were calculated and converted to an area percentage. This area ferrite content was assumed to be equivalent to the volume percentage of residual δ-ferrite in the base material.

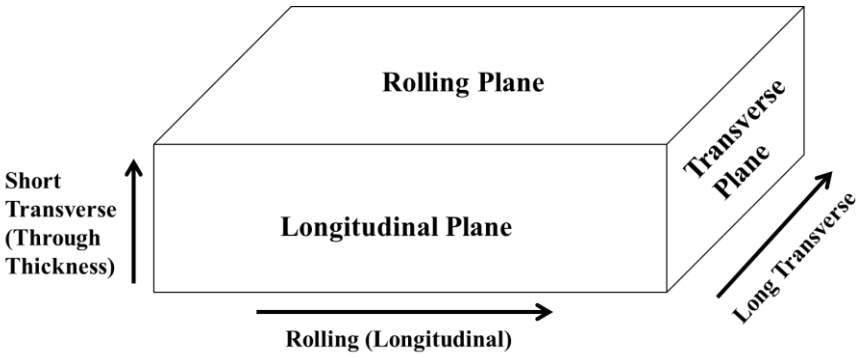

Figure 2.2. *The figure shows the three directions as well as the planes associated with each of the samples.*

One longitudinal face sample was taken from each of the 1/2" and 1" thick 50CR base plates, were ground and polished to a 1200 grit finish, and analyzed using conventional powder X- Ray Diffraction (XRD) to estimate the volume fractions of the phases present and to determine if any retained austenite can be detected. The diffraction patterns were obtained using a Panalytical X'pert Pro multipurpose X-ray diffractometer or a Malvern-Panalytical Empyrean multipurpose X-ray diffractometer.

The filler wires were mounted using epoxy resin. The samples were then ground, polished to a 1-micron finish, and characterized using OM, SEM (using a Quanta LV200), and EDS. In order for the mounted sample to not charge in the SEM, the samples were coated with gold-palladium using a Technics sputter coater.

2.2.4 Hardness Testing

Micro-hardness testing was performed using a conventional Vickers testing machine (Bühler Micromet 5101) using a load time of 15 seconds and a load of 500 g. Data points were taken roughly 0.025" apart. One line of micro-hardness data was taken through the thickness on

two 50CR base material samples from the Group 1 plates, Group 2 plates, and the Group 3 plates, for a total of six samples.

2.2.5 Uniaxial Tensile Testing

Tensile testing was performed on the two batches of 1/2" thick 50CR in the L and T orientations, where the length of the tensile sample was parallel to the direction indicated. The strain rates imposed involve a ramping up program, shown in Table 2.2, in accordance to ASTM A370, which respects the relative strain rate insensitivity of steels during low temperature deformation.[67] Samples with 2" gage length were machined in accordance with the ASTM A370 sheet-type sample geometry, shown in Figure 2.3. Five samples were tested for each condition using a servo-hydraulic controlled 55-kip capacity MTS Model #319.25 at the Virginia Transportation Research Council. A laser extensometer and reflective tape was used to measure the gauge length initially and during the elongation during the testing.

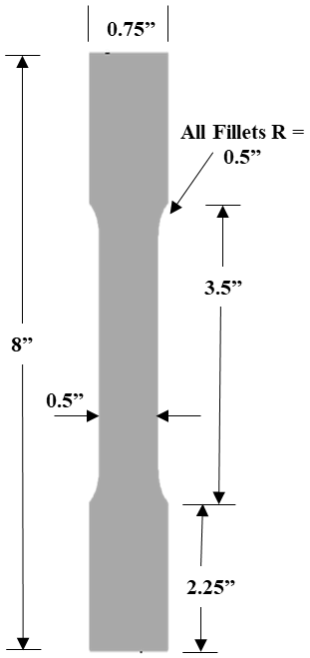

Figure 2.3. *This engineering drawing shows the dimensions of the 1/2" thick 50CR tensile specimen. All of the units are in inches. The direction that the length of the sample was oriented dictated whether the sample was a L or T sample.*

Table 2.2 *Tensile testing program used at the Virginia Transportation Research Council to test the 0.5" thick base 50CR samples.*

Speed (in/s)	Strain Range
0.0005	0.0 – 0.05
0.001	0.05 – 0.10
0.002	0.10 – 0.15
0.004	0.15 – 0.20
0.008	0.20 – end

The tensile testing machine collected the time, axial force, the axial displacement and the laser displacement (as a laser extensometer and reflective tape was used). For the determination of the Holloman strength coefficient (K) and the strain hardening exponent (n), the true stress and true strain were plotted from the 0.2% offset yield stress to the tensile stress. The equation for the curve of best fit is given in Equation 2.2. Because the testing program used doubled the strain rate after the laser strain equaled 0.05, 0.10, 0.15, and 0.20, the strain rate sensitivity (m) was calculated using Equation 2.3.

$$\sigma_{true} = K{\varepsilon_{true}}^{n}$$

Equation 2.2. *The Holloman equation equates true stress with the Holloman stress coefficient multiplied by the true strain raised to the strain hardening exponent while accounting for the existence of a yield stress.*[70]

$$m = \frac{ln\,(\frac{\sigma_2}{\sigma_1})}{ln\,(2)}$$

Equation 2.3. *The strain rate sensitivity (m) is calculated by the natural log of the stress before (σ_1) and after (σ_2) the change in strain rate divided by the natural log of the changed strain rate divided by the original strain rate. Since each change in the strain rate was doubled, the denominator is the natural log of 2.*

2.2.6 Charpy V-Notch Impact Testing

CVN testing was performed on the 1/2" thick 50CR base metal in the both LT and TL orientations using a Tinius Olsen 406.7 J (300 ft·lbf) capacity Charpy testing machine at the Turner-Fairbank Highway Research Center. The length of the LT sample is oriented in the longitudinal (L) direction and the V notch (cracking direction) is parallel to the transverse (T)

direction. The TL sample is oriented in the opposite manner. Twenty full-size base material CVN samples of each orientation were machined from one of the Group 1 (1/2" thick) welded plates far enough away from both the edge of the plate and the weld to be representative of the base metal performance, in accordance to ASTM E23.[84] Three samples were tested at 40 °F, the temperature indicated by ASTM A709 for Virginia.[37] Samples were tested at each of the following additional temperatures: -100, -80, -60, -30, -10, and 10 °F, to determine the DBTT. Analysis of the DBTT behaviors used least squares minimization to obtain a best-fit hyperbolic tangent curve. The resulting curve is commonly used to define three-regimes: the upper shelf, transition region, and lower shelf.

2.2.7 Fractography

Fractography was performed on two of the 1/2" thick 50CR tensile samples and two of the 1" thick 50CR tensile samples using OM as well as SEM. Fracture analysis was also performed on the 1/2" thick 50CR CVN samples tested at the highest and lowest temperatures using the OM and SEM. Samples were sonicated in methanol with the fracture side facing up for five minutes before being placed in the SEM to minimize contamination and prevent charging. Fractography was performed a Quanta LV200 as well as a FEI Quanta 650.

Additionally, one of the 1/2" thick delaminated tensile specimen was mounted with the rolling plane exposed, ground and polished to a 1-micron finish, and etched using Vilella's reagent. The sample was then characterized by OM. Due to the observation of precipitates on the fracture surface looking at the delaminated crack surface, XRF was used to determine if there was an overall local increase in an alloying element, while EDS was used to determine the composition of the precipitates on a smaller scale level.

The widths and thicknesses of the uniaxial tensile samples were measured using calipers after delamination occurred and then used to calculate the ratio between the strain in the width

and thickness directions. The widths and thicknesses prior to testing and after delamination were then used to calculate the reduction in area as a percentage, by taking the ratio between the difference in the final and initial cross-sectional areas and the initial area. The widths and thicknesses were also measured 3.5" away from the end of the sample (equal to roughly 0.5" within the gage length mark) to estimate the ratio of the strains during uniform elongation. This assumed that 0.5" within the gage length is sufficiently far away enough from the necked region that no strain localization occurred.

2.3. Results

2.3.1 Compositional Analysis

Table 2.3. *Comparison between the ASTM A709 grade 50CR requirements, the 50CR producer's nominal composition, and the composition of the 50CR found in this study. The single values given in the first two columns of the table indicate a maximum weight percentage (wt%) of the element allowed in the alloy.*

Alloying Element	Duracorr ®[18]	50CR[37]	Emission and Combustion Spectroscopy	XRF
C	0.025	0.030	0.01	N.D.
N	0.030	0.030	0.008	N.D.
Mn	1.50	1.50	1.23	1.35
P	0.40	0.040	0.025	0.010
S	0.010	0.010	0.004	N.D.
Si	0.70	1.00	0.36	0.51
Cr	11.0 – 12.5	10.5 – 12.5	11.40	11.39
Ni	1.00	1.50	0.36	0.43
Mo	0.20 – 0.35		0.28	0.27
Cu			0.10	0.13
Al			0.004	0.099

Note: N.D. = not detectable. Because of the type of XRF used (energy dispersive), C and N were outside of the detection limit of the instrument used. Similarly, the difference between the energies of the characteristic X-rays of Mo (2.293) and S (2.308) are smaller than the resolution of energy dispersive XRF, and was not able to be accurately determined.

A comparison between the nominal compositional requirements and the composition range found in the current study are shown in Table 2.3. The single values given in the first two

columns of the table indicate a maximum weight percentage (wt%) of the element allowed in the alloy. The XRF data shows the average of the values found across the six total specimens. Although Mo, Cu, and Al are not included in the compositional requirements for 50CR, ASTM A751[85] allows for the addition of alloying elements not specified as long as the steel can still fulfill the necessary mechanical properties, which in this case are 50 ksi for yield strength, 70 ksi for tensile strength, 21% elongation, and 15 ft·lbf at the ASTM A709 required testing temperature.[37]

Table 2.4. *Comparison between AWS A5.9/AWS A5.22 filler wire composition requirements and composition of the filler wires used for the study determined by combustion and emission spectroscopy.*

Element	ER309L	309L Company1	309L Company2	ER309LC	309LC Company1	309LC Company2
C	0.03	0.02	0.018	0.03	0.35*	0.031*
Cr	23.0 – 25.0	23.5	23.4	23.0 – 25.0	24.1	23.7
Ni	12.0 – 14.0	13.5	13.5	12.0 – 14.0	13.0	14.3*
Mo	0.75	0.04	0.043	0.75	0.08	0.078
Mn	1.0 – 2.5	1.62	1.57	1.0 – 2.5	1.52	1.48
Si	0.30 – 0.65	0.33	0.34	0.30 – 0.65	0.60	0.49
P	0.03	0.015	0.015	0.03	0.021	0.024
S	0.03	0.006	0.009	0.03	0.003	0.003
Cu	0.75	0.05	0.060	0.75	0.16	0.18
Other			0.11 Co, 0.040 V			0.085 Co, 0.062 V

** = outside of limits set forth by AWS A5.22, as discussed below*

It can be seen in Table 2.4 that two elements in the 309LC are outside of allowable limits dictated for ER309LC, C and Ni.[80] Based on communications with the first company, roughly 0.4 g was used for combustion testing for the determination of the C content. The resulting 0.35 wt% is equivalent to 1.4 mg of C, which is likely due to contamination of the metal powder contained in the metallic sheath. Due to the C content being outside the allowable limits, a sample was sent to a second company to determine if 309L is outside of the allowed compositional limits or not. The C content determined by the second company was also outside

of the allowable limits, but only by 0.004 mg. Similarly, the Ni level measured by the second company is outside the allowable limits by 0.3%. For the determination of the metallic elements, an estimated 1 g of wire is used for inductive coupled plasma optical emission spectroscopy. Based on this, it is estimated that the Ni exceeds the limit by 3 mg, which could easily be accounted for by one or two grains of the Ni powder. In conclusion, due to the nature of the metal cored wire, enforcing traditional compositional limits is difficult. Scrutiny must be used when preparing the samples and analyzing the results.

Due to the limitations of SEM-based EDS and its tendency to overestimate the presence of lighter elements, the concentrations of C, S, and P are not reported for 309L, 309LSi, or 316L in Table 2.5. However, the remaining elements are estimated to fall within the compositional requirements.

Table 2.5. *Semi-quantitative compositional analysis of solid filler wires (309L, 309LSi, and 316L) using EDS. N.D. indicates the elements that are not detectable using EDS.*

Element	ER309L	309L	ER309LSi	309LSi	ER316L	316L
C	0.03	N.D.	0.03	N.D.	0.03	N.D.
Cr	23.0 – 25.0	24.6	23.0 – 25.0	24.4	18.0 – 20.0	19.5
Ni	12.0 – 14.0	13.1	12.0 – 14.0	13.5	11.0 – 14.0	11.8
Mo	0.75	0	0.75	0	2.0 – 3.0	2.1
Mn	1.0 – 2.5	1.6	1.0 – 2.5	2.3	1.0 – 2.5	2.1
Si	0.30 – 0.65	0.4	0.65 – 1.00	0.8	0.30 – 0.65	0.4
P	0.03	N.D.	0.03	N.D.	0.03	N.D.
S	0.03	N.D.	0.03	N.D.	0.03	N.D.
Cu	0.75	0	0.75	0	0.75	0

2.3.2 Microstructure Predictive Analysis

Using the Kaltenhauser Equation and the compositional data obtained from emission and combustion spectroscopy, the ferrite factor was determined to be 9.1. This means that the microstructure will be partially ferritic with either martensite or austenite present at room temperature, depending on the M_f temperature and the cooling rate. By applying Equation 2.1. to the composition obtained by external testing, it was predicted that ferrite content will be 51%.[24]

Calculating and plotting the Cr_{eq} and Ni_{eq} values of 12.22 and 1.565 respectively, onto the Schaeffler diagram yielded a predicted microstructure that will be some combination of martensite and ferrite. However, because the Schaeffler diagram does not provide iso-ferrite lines in the M + F region, an exact ferrite value could not be predicted.

Similarly, the Cr_{eq} and Ni_{eq} values were calculated and plotted using the preliminary[7] and later published Balmforth diagrams.[7,24] The plotted values were 14.668, 4.62 and 12, 0.87. This difference is due to the changing of the coefficients as well as the removal of Mn from the Ni_{eq} calculation and Si from the Cr_{eq}. Both sets of Balmforth Cr_{eq} and Ni_{eq} calculations yield a predicted microstructure of martensite and ferrite, but the predicted volume content of ferrite varied drastically, yielding 30 vol% and 75 vol% respectively. Due to the fine-tuning of coefficients in the calculations as well as the removal of both the Mn and Si (roughly present in equal wt% in 50CR), the prediction of 75 vol% is likely more accurate.

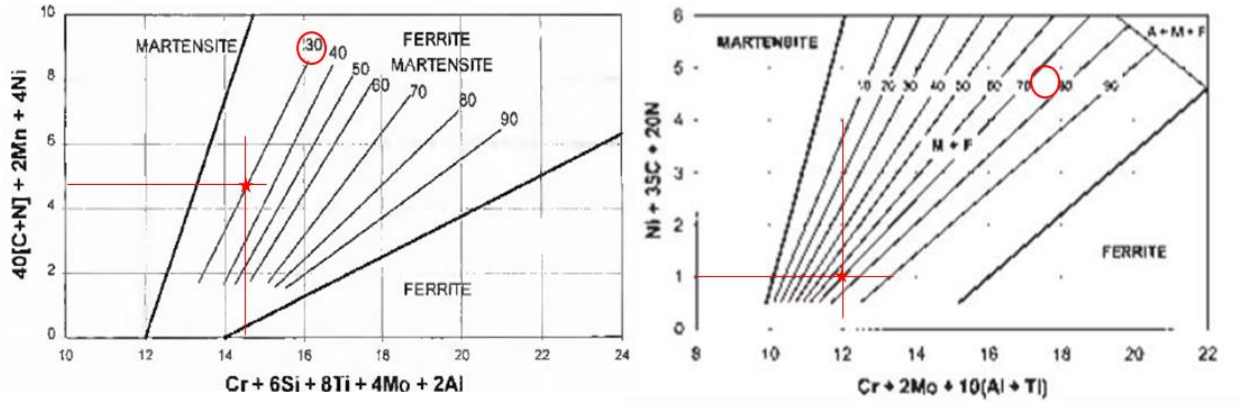

Figure 2.4. *The figure shows the location of the 50CR base material based on the Cr_{eq} and Ni_{eq} values based on the respective Balmforth equations. a) This diagram calculates the Cr_{eq} and Ni_{eq} values using the Kaltenhauser Equation.*

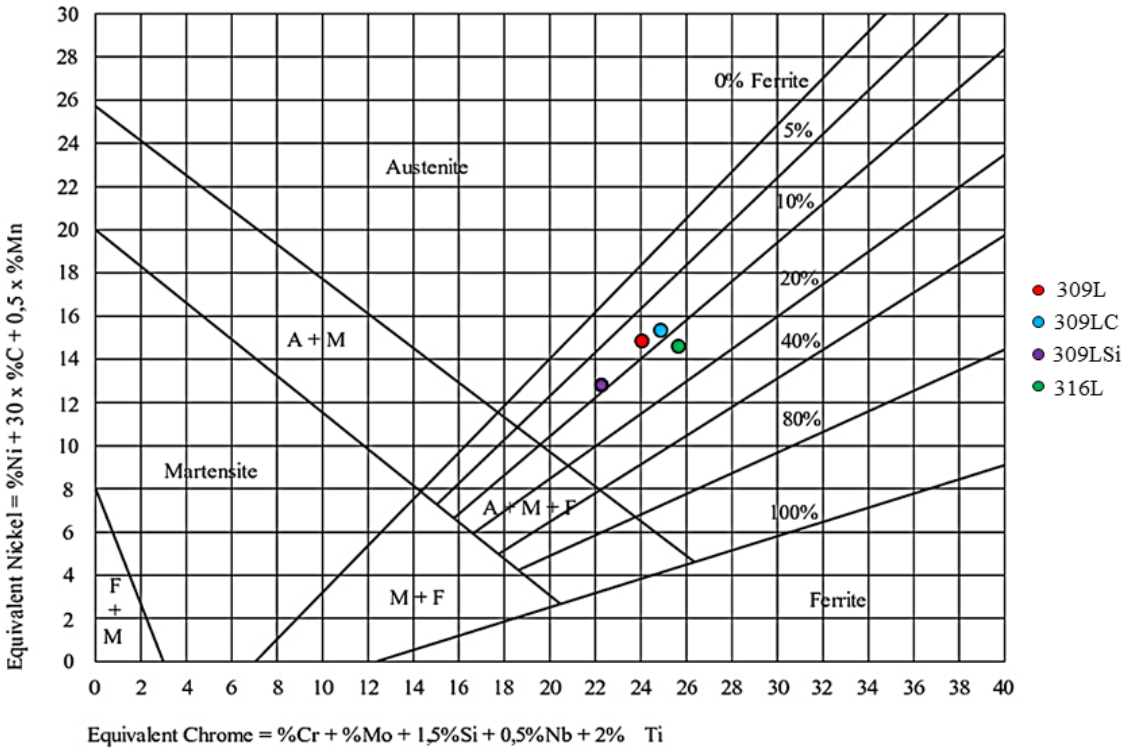

Figure 2.5. *The figure shows the location of the four types of filler wires based on the Cr_{eq} and Ni_{eq} values using the Schaeffler equations. It can be seen that all of the filler wire compositions are designed to have around 10 vol% of ferrite after welding.*

2.3.3 Microstructural Analysis

Micrographs of 50CR base metal revealed the expected dual-phase microstructure for this type of alloy.[1,4,18] The microstructure is comprised of elongated ferrite grains between bands of tempered martensite grains, which ranged from five to fifty microns in thickness. The phase identification was determined by the color contrast in the micrographs. Vilella's etchant reveals general features of the microstructure (such as grain size and shape) and darkens the martensite grains more than the ferrite.[1,24] The dark regions in the optical micrographs (which are highlighted with yellow circles) reveal the presence of stringers, which were found to be Al (in batch 1 of the 1/2" thick plate) or Si (in batch 2 of the 1/2" thick plate) based according to the semi-quantitative EDS shown in Figure 2.6c-d. This difference was reflected in the XRF data for

the two batches of 1/2” thick plate. Sometimes, these stringer particles also contained trace amounts of Mg, Ca, and Ti.

Optical micrographs obtained at 250x magnification were processed using an image analysis program, and the micrographs were thresholded such that the ferrite appears white and the martensite appears black. Analysis of such micrographs revealed a range of ferrite content of five to fifteen vol% in the 1/2” plates and five to ten vol% in the 1” plates, with the remainder determined to be martensite. Analysis of the data determined that there was not a statistically significant difference in the ferrite content between plate thicknesses nor between the longitudinal and transverse faces. One key difference between the 1/2” and 1” thick 50CR microstructures is the gradient in the elongation of the ferrite phase. In the 1” sample, the highest degree of alignment and elongation occurred towards the center of the thickness. This gradient behavior did not seem to occur in the 1/2” samples, and the ferrite was generally elongated throughout the thickness.

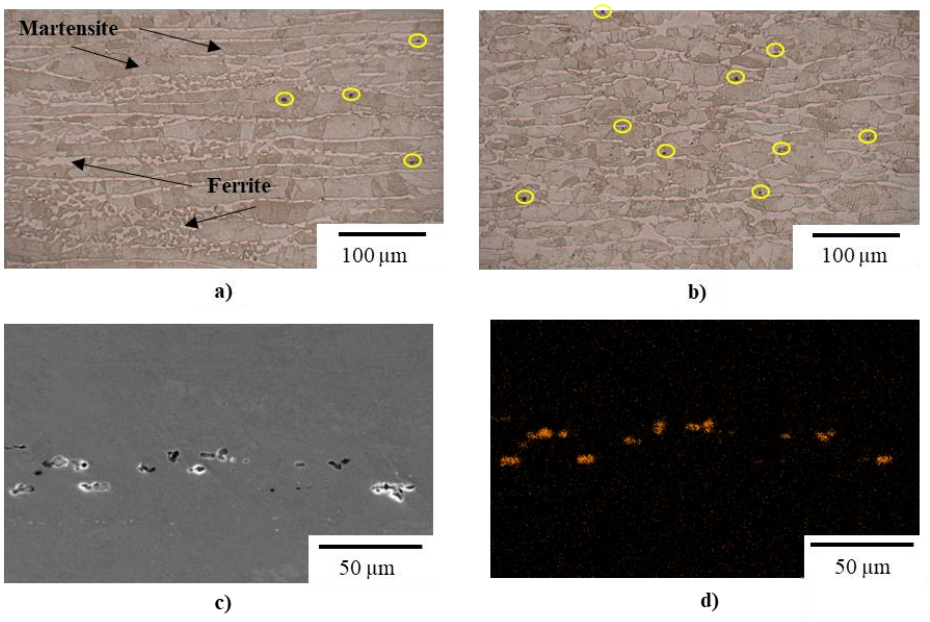

Figure 2.6. *50CR microstructure taken from the* ***a)*** *longitudinal and* ***b)*** *transverse faces of 1/2” thick base plate at 600x magnification using bright field OM with the Al containing particles highlighted with yellow circles around each particle;* ***c)*** *SEM micrograph of stringers;* ***d)*** *corresponding EDS map of Al.*

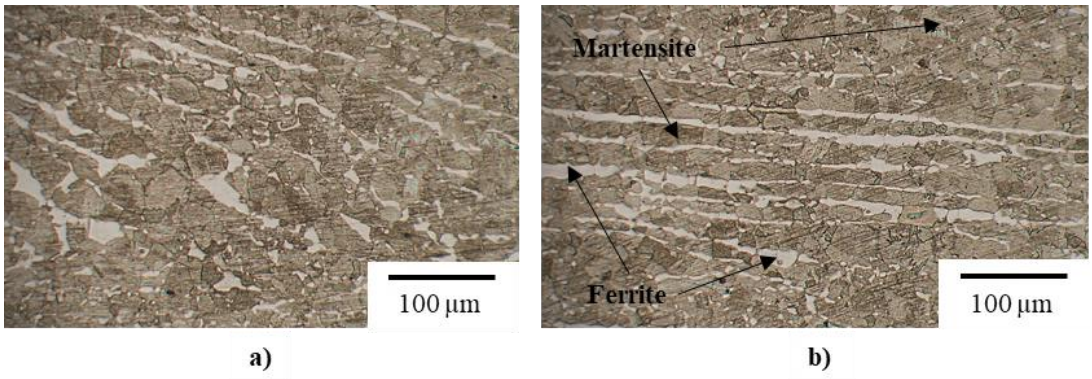

Figure 2.7. *50CR microstructure taken from the longitudinal face of 1" thick base plate at 600X magnification using bright field OM. Vilella's reagent colors martensite and leaves ferrite unetched.*

Conventional powder XRD revealed that there was no residual face centered cubic (FCC) γ-austenite (above the detection limit, taken to be 0.5 – 2 vol%)[86] in the microstructure of 50CR. The XRD pattern of 50CR, shown in Figure 2.8., revealed only body centered cubic (BCC) peaks indicative of both ferrite and martensite (which cannot be discriminated in conventional powder diffraction experiments).

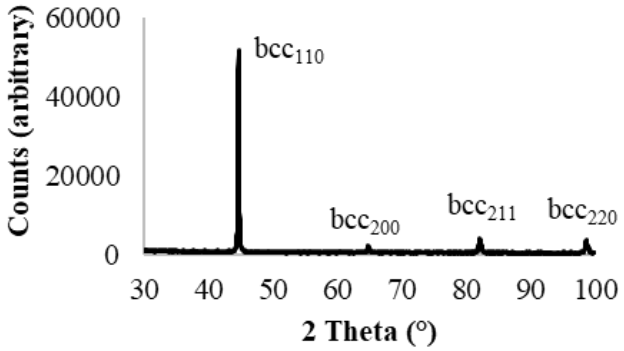

Figure 2.8. *50CR XRD pattern revealing only the presence of BCC type reflection peaks. This indicates that there was not retained austenite above the XRD detectable limit (typically taken to be around 2 vol%).*[86]

Micrographs of the two different wire constructions (solid and metal cored) can be seen in Figure 2.9. The 309LC metal cored wire consisted of a metallic sheath mechanically wrapped around a loose mixture of metal powders. EDS mapping of the cored wire, shown in Figure 2.9c – f, revealed that the metal powder primarily consists of pure Ni particles and particles of a 70%

Cr- 28% Fe alloy containing trace amounts of Mn and Si. The metallic sheath had a nominal composition of 68% Fe, 19% Cr, 9% Ni, 1.5% Mn, and 1% Si (wt%).

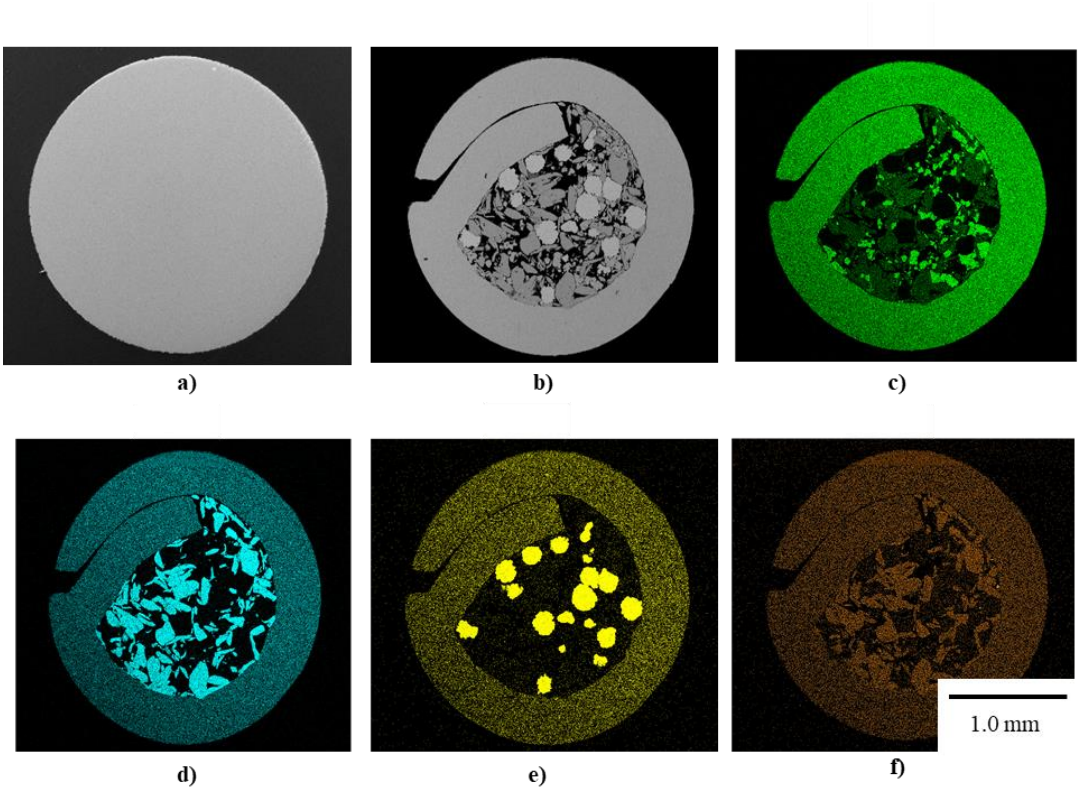

Figure 2.9. *Representative SEM micrographs of* ***a)*** *solid wire and* ***b)*** *cored wire, and EDS maps of* ***c)*** *Fe,* ***d)*** *Cr,* ***e)*** *Ni, and* ***f)*** *Mn*

2.3.4 Hardness Testing

Microhardness testing of the 50CR base metal revealed an average hardness of 200 ± 10 HV5, for Groups 1 (1/2") and 2 (1"). The hardness of the 1" thick Group 3 plates was determined to be slightly higher at 245 ± 10 HV5. These differences in hardness between the groups of base material reflect the variability of the material. Hardness testing through the thickness of the material did not reveal any sort notable variability.

2.3.5 Uniaxial Tensile Testing

The base 50CR from 1/2" thick plates examined in this study surpassed the minimum requirements for the tensile properties indicated in ASTM A709, a yield strength of 50 ksi and a

tensile strength of 70 ksi, and an elongation of 21% as shown in Table 2.6.[37] Although analysis showed that there was a statistically significant difference between the two batches of 1/2" 50CR, the difference is indicative and a result of the commercial steel manufacturing process. A compilation of the mechanical properties of 50CR can be found in Table 2.7.

Table 2.6. *Testing results for the determination of compliance of 50CR with requirements set forth by ASTM A709 for Grade 50CR*

Sample ID & Orientation	Yield Strength (ksi)	Tensile Strength (ksi)	% Elongation
First Batch 50CR L	66.3 ± 0.6	83.4 ± 0.8	28.9 ± 1.61%
First Batch 50CR T	64.3 ± 0.4	80.9 ± 0.2	31.1 ± 0.94%
Second Batch 50CR L	68.2 ± 0.4	89.8 ± 0.2	28.3 ± 0.57%
Second Batch 50 CR T	67.3 ± 0.2	87.1 ± 0.2	30.2 ± 0.32%

Table 2.7. *Average mechanical properties (in metric units) of 50CR determined by tensile testing.* ***K*** *is the Holloman stress coefficient and* ***n*** *is the strain hardening exponent. The* $\boldsymbol{m_1}$ *and* $\boldsymbol{m_2}$ *represent the strain rate sensitivity due to the first and second doubling of the strain rates.*

Material Property	Y.S. (MPa)	T.S. (MPa)	% Elong	E (GPa)	K (MPa)	n	m_1	m_2
L Orientation	464	597	28.6%	204	772	0.092	0.002	0.001
T Orientation	454	579	30.7%	185	752	0.092	0.002	0.001

2.3.6 Charpy V-Notch Impact Testing

Because Virginia is in temperature zone 2, as defined by AASHTO LRFD Bridge Design Specifications, three 50CR samples were tested in each orientation at 40 °F.[37,76] The 50CR samples surpassed the minimum impact energy requirements dictated by ASTM A709 in both orientations.[37] The LT sample tested at 10 °F stopped the hammer with an impact energy of 298 ft·lbf. To prevent damage to the Charpy testing machine due to operation within 80% of its maximum capacity, no additional LT samples were tested at 10 °F or above.[84] The three TL samples had impact energies of 215, 164, and 161 ft·lbf, averaging to 180 ft·lbf at 40 °F. These values greatly exceed the 15 ft·lbf minimum required for non-fracture critical tension components and 25 ft·lbf minimum for fracture critical components of grade 50CR structural steel.[37] Figure 2.10. shows the measured impact energy as a function of temperature for the LT

and TL 50CR samples, with additional test temperatures chosen to fill out the transition temperature curve. The DBTT was determined to be: -38 °F in the LT orientation and -40°F in the TL orientation.

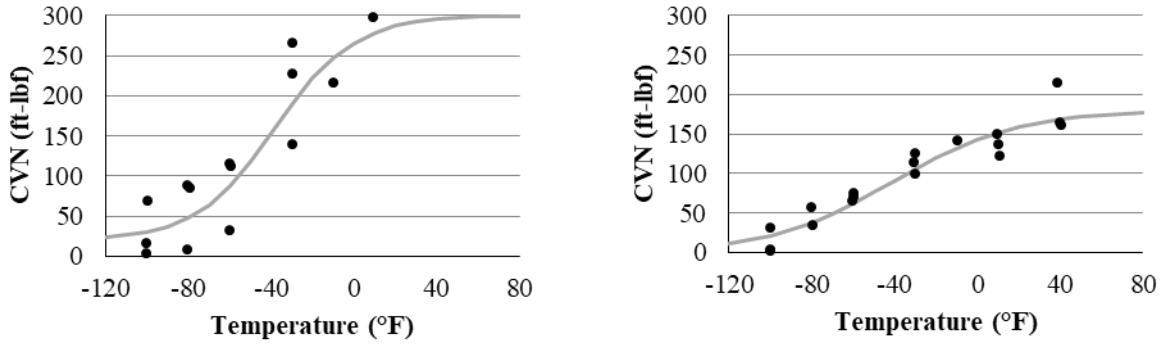

Figure 2.10. *Charpy V-notch impact energy data for 50CR for the entire range of temperatures tested (LT sample orientation on left, TL on right).*

2.3.7 Fractography

During the tensile testing, delamination cracking occurred in the center of the thickness of the samples in both the L and T orientations, shown in Figure 2.11. This occurred after the maximum load or tensile stress was surpassed and towards the end of testing. Using calipers, the cross-sectional area was measured, and the true strain was calculated, shown in Table 2.8.

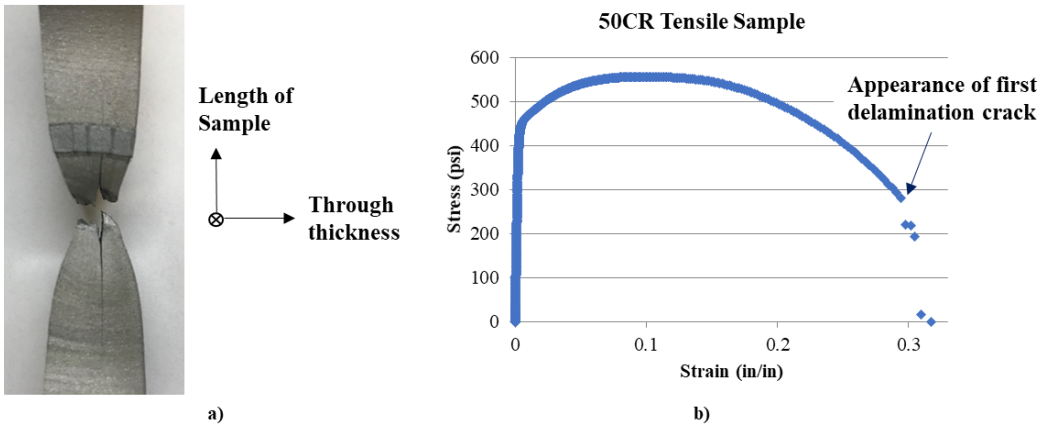

Figure 2.11. a) *The delamination crack occurs around the midpoint in the through-thickness direction. The orientation of the sample determines the "length of sample" direction.* ***b)*** *This engineering stress-strain curve shows the typical behavior of 50CR during a tension test. As the maximum load is surpassed and necking begins, the load decreased until a certain stress state is achieved. The delamination crack then appears near the center of the through-thickness of the specimen and causes a dramatic drop in stress.*

Microstructural analysis of the flow face (containing the orientation direction of the length of the sample and the through thickness direction) indicates that the delamination cracking did not occur as a singular crack that propagated through the length of the specimen, but as multiple micro-cracks that joined together. This can be seen in Figure 2.12. This joining of the micro-cracks to form the main macroscopic fracture crack gives it its undulating or jagged appearance. These micro-cracks (highlighted by the red outline) commonly formed at or near the interphase boundary between the ferrite (the white phase) and the martensite (the black phase), as shown in Figure 2.13.

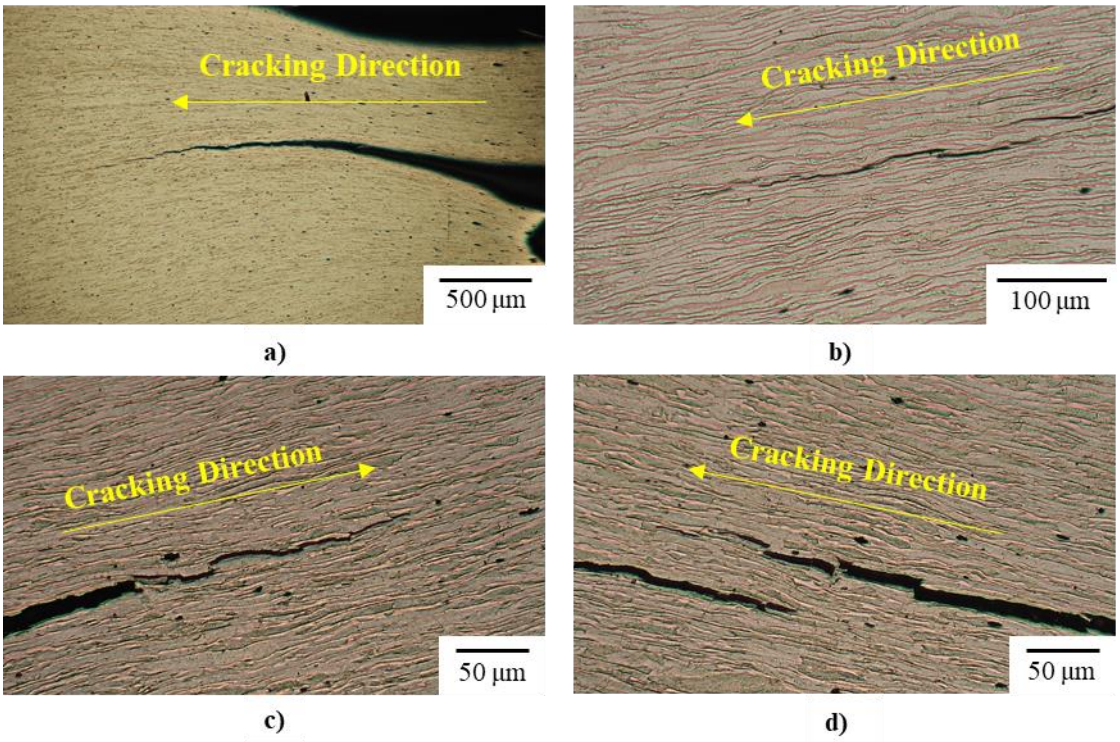

Figure 2.12. a) *OM at 100x magnification of a secondary delamination crack seems to indicate that the delamination cracking occurred as one large propagating crack, but inspection at higher magnifications* ***b)*** *600x and* ***c) – d)*** *at 800x shows that the delamination cracking occurred as many micro-cracks that propagated together in order to form the macroscopic crack.*

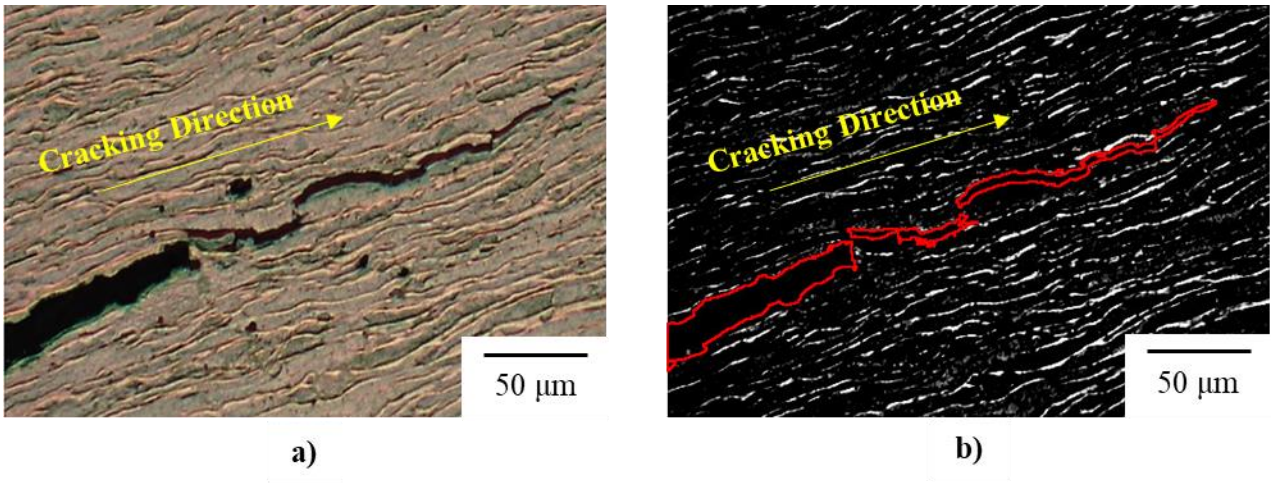

Figure 2.13. a) *OM at 1000x magnification of the secondary delamination crack presented in Figure* ***2.12c. b)*** *Using post-image processing, the 50CR was converted to binary with the white phase being ferrite and the black phase being martensite. The delamination crack is outlined by red. It can be seen that the delamination crack occurred at or near the interface between the ferrite and martensite phases.*

Using SEM to characterize the fracture surface looking down the length of the sample, the two ends of the tensile sample were determined to fracture predominantly in a ductile manner, due to the presence of dimples. However, looking at unpropagated cracks in Figure 2.14 shows that the delamination of 50CR occurs through in a quasi-cleavage brittle manner, shown in Figure 2.12 c) and d). This delamination behavior appears to be aided by the presence of precipitates, which were found to be Al or Si containing precipitates, similar to those shown in Figure 2.6.

Looking at surface of the crack in the through-thickness direction confirmed that the dominating fracture mode for the delamination occurred by quasi-cleavage, shown in Figure 2.15. Regions of high plastic deformation are predicted to be ferrite. This is due to the more ductile nature of ferrite when compared to martensite as well as the phase percentage determined by the conventional metallography. Sonicated to minimize contamination, the fracture surface still contained many precipitates. These were again determined to be Al or Si containing precipitates. XRF of the delamination root area showed an Al content at least one order of

magnitude higher than the 50CR base material. This indicates that the delamination cracking occurred where the concentration of the precipitates was the highest.

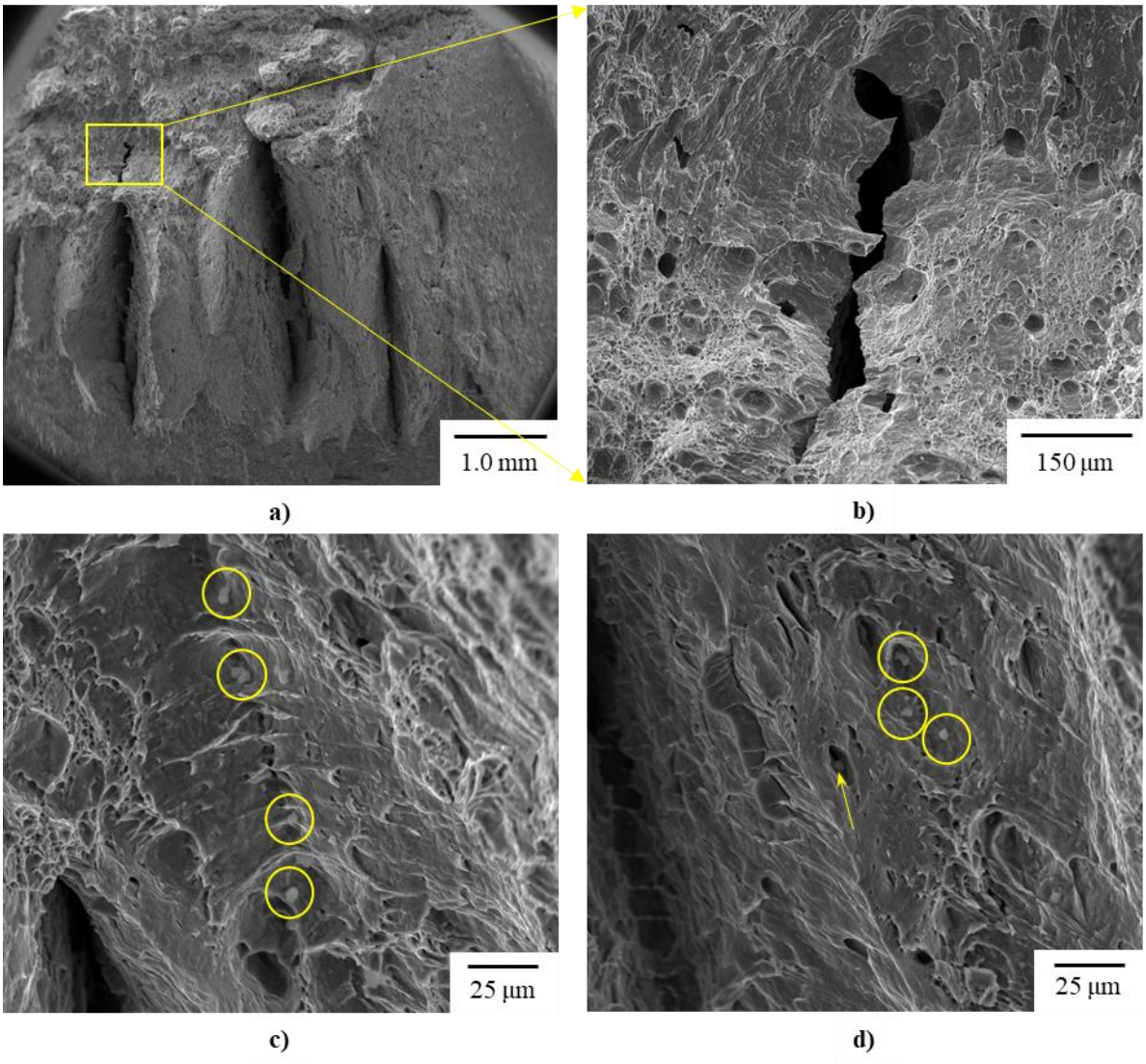

Figure 2.14. a) *SEM micrograph at low magnification of the delaminated sample showing multiple delamination cracks.* ***b)*** *Observation of the arrested delamination crack indicates that the tensile sample fractures into two separate pieces through ductile failure (indicated by the dimples).* ***c) – d)*** *Higher magnifications reveal the presence of precipitates, roughly a couple of microns in size, that appear with the beginning of delamination cracking. These were found to be largely Al or Si based.*

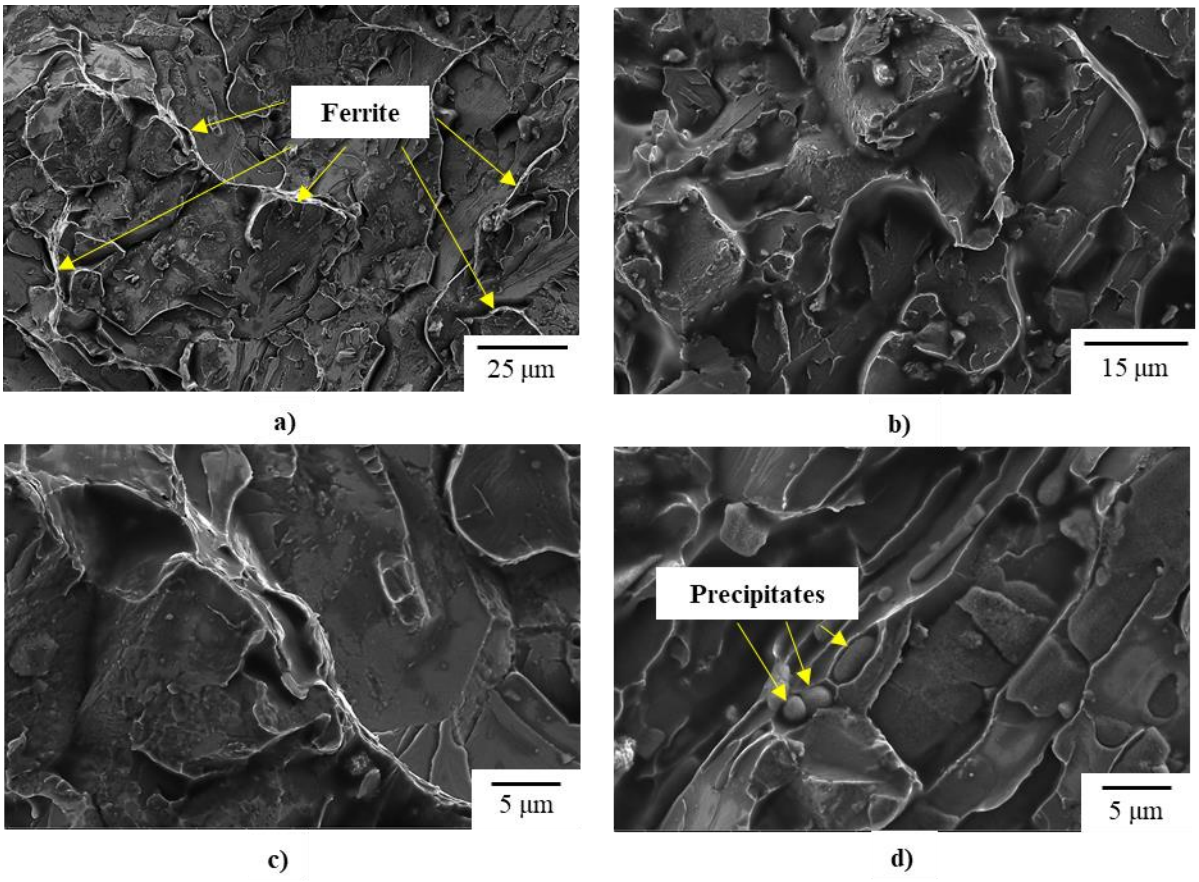

Figure 2.15. a) *SEM micrograph of the main delamination crack fracture face of a 1" thick welded 50CR sample. Regions of quasi-cleavage are interspersed with ribbon-like regions of high plasticity. These are predicted to be ferrite, based on the relative amount present and the mechanical properties of ferrite when compared to martensite.* ***b – c)*** *Observation at progressively higher magnifications revealed the non-linearity commonly seen of the ferrite phase in the 1" thick 50CR samples.* ***d)*** *Higher magnifications reveal the presence of precipitates on the scale of a couple of microns in size. These were again found to be largely Al or Si based.*

The ratios of the true strain in the width to the true strain in the thickness can be seen in Table 2.8. For a value less than one, the material strains faster in the thickness direction (the through-thickness or short transverse direction). This occurred both before and after strain localization and the formation of the neck.

Table 2.8. *Average of five 1/2" thick 50CR samples determined by using calipers to measure the final dimensions after delamination has occurred as well as the dimensions 3.5" from the end of the sample.*

Material Property	R "uniform"	R neck	Reduction in Area (%)
L Orientation	0.563	0.696	78.0%
T Orientation	0.384	0.618	81.6%

Similar observations were made on the fracture surfaces of the CVN samples. The fracture surfaces of the CVN samples tested at the highest and lowest testing temperatures are shown in Figure 2.16. Delamination cracking was shown to be associated with the occurrence of lateral expansion (the outward shearing of the CVN sample causing the cross-section to change from a square to a trapezoid), directly correlated with the ductility of a material. In the samples that showed little to no lateral expansion, such as the samples tested at -100 °F in Figure 2.16 a) and c), delamination cracking did not occur.

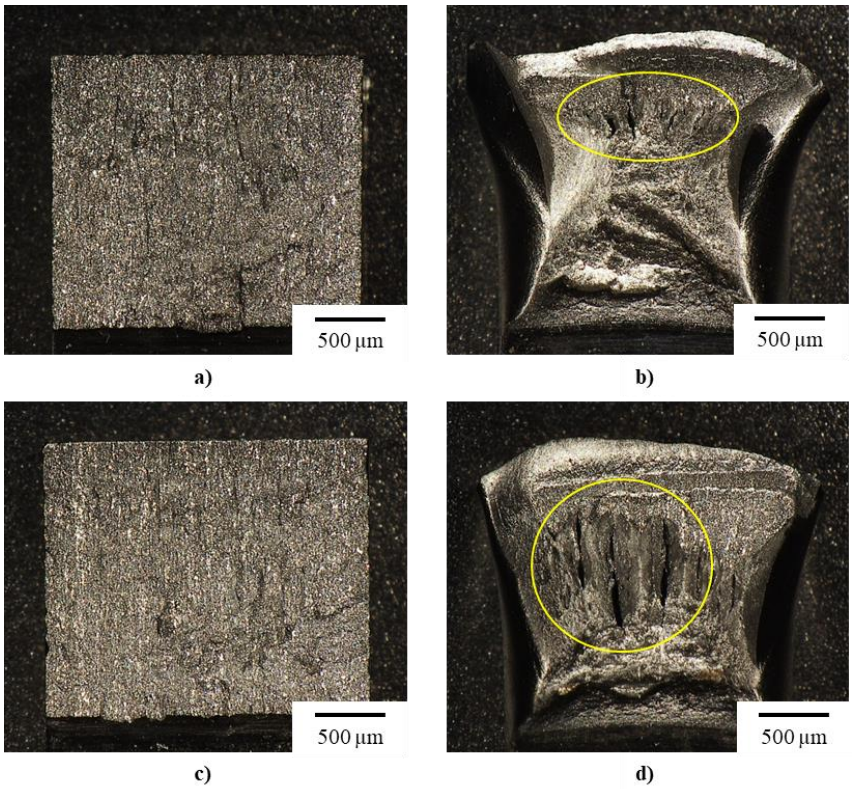

Figure 2.16. *Optical micrographs of the CVN 1/2" 50CR samples tested at the lowest and highest testing temperatures in* ***a – b)*** *LT and* ***c – d)*** *TL orientations taken at 20x magnification. The delamination cracks are highlighted by the yellow oval.*

2.4. Discussion

2.4.1 Base Material (50CR)

Although there were variances within the different melts of 50CR received, the compositions were determined to be within the allowable limits of ASTM A709.[37] The compositional analysis also revealed the presence of elements that are not specifically called out in the grade 50CR compositional requirements. These additional elements are allowed by ASTM A751.[85] Mo is added to 50CR not only to improve corrosion resistance, but also to increase the amount of ferrite in the final microstructure because Mo is a ferrite stabilizer.[25,27–30] Based on communications with the 50CR producer, Al is added as a deoxidizer. Oxygen is considered to have detrimental effects on the mechanical properties of steel, especially the CVN impact energy.[68] Thus, elements such as Al, Si, Mn, and Ti are added to bind to the oxygen in the molten steel to form an oxide layer, which will float on top and can be removed.[87] The alumina that forms typically floats on the top of the crucible during melting, but eddy currents induced within the furnace can cause the alumina to enter the bulk. During subsequent deformation, such an oxide film or particles can be broken up and form what is known as "stringers", shown in Figure 2.6. The remaining trace elements come from contamination from the steel making process, such as the ladle and tundish. The Ti content in 50CR shown here is orders of magnitude lower than what was required in the legacy alloy, 3CR12, and can be treated as negligible.[9] Cu can also be added to increase a steel's resistance to atmospheric corrosion, and Ni can aid in the formation of an adherent mill scale (similar to what forms as the corrosion-resistant barrier in 50CR).[87]

The microstructural predictive models yielded a wide range of results. For a Kaltenhauser ferrite factor of 8 or 9, the microstructure is predicted to contain of 80-90 vol% martensite with the remaining phase assumed to be ferrite.[23] Although the Schaeffler and Balmforth diagrams

correctly predict that the microstructure will be a combination of ferrite and martensite, the amount of ferrite was greatly overestimated. This can be partially accounted for the fact that the constitution diagrams do not take into account the thermomechanical processing, which can greatly affect the microstructure. Furthermore, the constitution diagrams are created under specific conditions and then analyzed using conventional metallography. This both limits the applicability of the solutions as well as the introduces the potential for significant error. Phase analysis by conventional metallography is heavily dependent on the sample preparation and the method used to determine the phase content, whether it is through the line method, the point counting method (used by Balmforth), or another method.[24,28] The accuracy can be greatly improved through the use of a post-image processing program, such as ImageJ, to determine an area-based phase content.

The typical microstructure observed for 3CR12 and its related 12% Cr based alloys is elongated ferrite grains interspersed within a banded martensite microstructure.[2–4,9,11,18,23,88,89] Vilella's etchant is commonly used for martensitic, ferritic, and dual phase steels and will only lightly etch the ferrite while actively etching the martensite.[7,83,86] Because retained austenite was neither observed by conventional metallography (meaning the content if present was less than 10 vol%) nor detected by XRD (meaning the content if present was less than 0.5 vol%), the Mf temperature can be assumed to be higher than room temperature, which agrees with the data obtained previously for 3CR12. This is because the Ms and Mf temperatures are largely dictated by the C% as well as by other austenite stabilizer contents, which are not significantly different between 50CR and 3CR12.[86]

Testing of 3CR12 revealed a broad range of mechanical properties.[2–4,9–12,32,90] The typical tensile properties for 3CR12 are as follows: a yield strength of 52.21 ksi, a tensile strength of

73.97 ksi, and a percent elongation of 28%.[91] The strain hardening rate of 3CR12 was found to be 0.15.[33] Tensile testing performed on 11Cr/A1010 resulted in a yield strength of 56.7 ksi, a tensile strength of 76.7 ksi, and a percent elongation of 36%.[1] Testing performed by ArcelorMittal on plates ranging from 0.157" - 0.375" thick plate resulted in an average yield strength of 58 ksi, a tensile strength of 77 ksi, and a percent elongation of 33%.[18] A range of yield and tensile strengths exists because the tensile properties of dual phase steels are a function of the volume percentages of martensite and ferrite, which are in turn a function of thermomechanical history and composition.[7,32,88,92–94] The mechanical properties of this type of dual phase steels range from 50 to 60 ksi for yield strength, 70 to 80 ksi for tensile strength, and 25% to 40% for elongation. The tensile properties of 50CR falls within the ranges of what is expected from literature.

Previous testing on 11-12% Cr steels shows a wide range of results for the impact energies as well as DBTTs. Testing of 11Cr in the LT orientation resulted in impact energies of 85 ft·lbf at -10 °F, 109 ft·lbf at 10 °F, 118 ft·lbf at 40 °F, and 154 ft·lbf at 70 °F.[1] A1010 (50CR) studies performed by ArcelorMittal and Oregon DOT showed a significant amount of scatter when tested at 10 °F, with values ranging from 60 to 225 ft·lbf on plates ranging from 1/2" thick to 1.5" thick.[38,74] The 50CR tested in this research showed comparable impact energies with respect to the previous alloys of 11Cr and A1010. Transition temperature curve analysis revealed that 3CR12 is approximately -4 °F in the LT orientation and 32 °F in the TL orientation.[2–4,88] The nominal DBTT of the 50CR base plate is taken to be -40 °F, a vast improvement. This is likely due to the absence of an abundance of precipitates (specifically Ti based in the case of 3CR12) within the alloy, which have been shown to act as crack initiation sites.

Delamination cracking has been observed in 3CR12 and A1010 tensile and CVN samples.[4,73] This was shown to occur even after extensive heat treatment and is attributed to the persistent directionality of 3CR12. However, delamination type cracking has been observed in other wrought alloys when a high triaxiality is imposed with the presence of non-metallic inclusions.[4,8,11] This type of cracking requires a high enough triaxiality, produced by necking, to impose a sufficiently high stress in the through-thickness direction, which can only happen in relatively ductile materials. The formation of the initial delamination crack leads to a favorable decrease in the triaxiality by decreasing the through-thickness stress.[4,11]

Characterization of 3CR12 delamination cracking performed by Knutsen revealed that the delamination cracking propagates by cracks opening ahead of main crack at points of weakness, leading to its fairly irregular appearance. The crack propagation mode along the split is a typically a combination of both intergranular and transgranular cleavage fracture, which allows the crack to follow a fairly straight path along multiple grains. A continuous grain boundary front maintained over many grains will favor delamination because the crack path will only be slightly affected by the micro-delamination occurring ahead of the main crack. However, the micro-delamination occurring of the main crack at points of weakness will cause a decrease in energy and will have a blunting effect on the main growing crack, causing it eventually to stop. Thus, it was concluded that the probability of delamination type cracking will increase with the increase in the parallel alignment of grain boundaries in the rolling plane.[4] Mintz further speculated that the delamination can be attributed to intergranular decohesion between the ferrite and martensite phases, and that the carbide-ferrite interphase boundary is very prone to crack initiation, which would act as the point of weakness ahead of the main propagating crack.[8]

The delamination behavior of 50CR largely agrees with that of 3CR12. The propagation of the delamination cracks appears to have occurred as multiple micro-cracks as observed by Knutsen. Closer inspection in 50CR revealed that Mintz attribution of the delamination cracking to the intergranular decohesion between the ferrite and martensite phases seems to be correct. The initiation of the delamination crack occurred only after significant necking has occurred, a reduction in area of about 80%. This implies that in order for delamination to occur, the material must be sufficiently ductile to reach the necessary triaxiality leading to a through-thickness stress sufficient to cause a crack between the phases. This hypothesis is supported by the lack of delamination cracking in the CVN samples that did not show significant amounts of lateral expansion, which is directly related to the ductility. Although the presence of a notch in the CVN samples causes triaxiality, without the ability to plastically deform, the necessary triaxial stress state is unable to be reached and therefore, delamination cracking does not occur.

The strain hardening exponent for 50CR was found to be 0.092 in both the L and T orientations. For a low strain hardening exponent, the multiplication of dislocations is not as significant as for a material with a high strain hardening exponent. This means that for two materials with the same starting dislocation density, the material with the higher strain hardening exponent will achieve a higher dislocation density at the maximum load or tensile strength. Due to dislocation entanglement and other hinderances to dislocation motion due to the high dislocation density, the material's ability to plastically deform is impeded and the probability of fracture increases. More importantly, the strain hardening exponent (n) in the Holloman equation (Equation 2.2) gives an indication of the onset of plastic instability. The strain hardening exponent found in 50CR is comparable to that of a high strength low alloy steel, shown to range from 0.02 – 0.25, depending on the tempering, as well as that of 3CR12.[33,95]

The ability of a material to neck without fracturing can be related to the strain rate hardening exponent, also known as the strain rate sensitivity.[96,97] This is represented by m in Equation 2.3. Studies have shown that even for low values of m, the inherent inhomogeneity associated with uniaxial tensile samples can lead to the stabilization of the neck. In fact, for an inhomogeneity with a ratio of 0.98 and a strain hardening exponent of 0.2, the addition of a strain rate sensitivity of 0.01 can delay the onset of catastrophic instability (when all of the strain localizes to the neck) by almost 15% strain.[97] Although the strain rate sensitivity for the testing of 50CR was found to be 0.002 or 0.001 depending on the sample orientation, this could account for the large post-uniform elongation shown in the same. The ability to delay the onset of catastrophic instability, i.e. the localization of all of the strain in a neck, inherently increases the stress in the through-thickness direction, allowing for the decohesion between elongated grains.

The ratio of the true strain in the width to the true strain in the thickness remained less than one both in the region considered to be uniform deformation as well as the necked region, indicating that the material strains faster in the thickness when compared to the width. This allows for a higher through-thickness stress to develop at a lower overall % elongation. However, the delamination did not occur until ~ 80% reduction in area was reached, indicating that delamination cracking can only occur when extreme necking is able to occur.

Once initiated, the delamination crack was able to easily travel along the boundary between the elongated ferrite and martensite phases. The presence of precipitates creates a point of weakness ahead of the main propagating crack and causes micro-cracks to form, which then become part of the main crack. However, instead of Ti based precipitates like those in 3CR12, the precipitates in 50CR were mainly Al or Si based. This is because 50CR is deoxidized using

primarily with Al and Si. This seems to indicate that the specific precipitate species does not matter.

2.4.2 Filler Wire (309L, 309LC, 309LSi, and 316L)

The composition of the solid filler wires was determined to be within the necessary requirements set forth by AWS. However, due to the construction of the metal cored wire, compositional analysis proved to be a challenge. The outer metallic sheath was determined to be insufficient in the Cr and Ni content when compared to the requirements for ER309L. This was supplemented by the pure Ni and Fe-Cr alloy powder in the inner core, shown in Figure 2.9. However, because the metallic sheath is only mechanically wrapped around the metal powder, one or two grains of the powder can greatly change the composition determined by emission and combustion spectroscopy, which samples a small amount of material. Thus, enforcing compositional requirements requires additional consideration.

Using the compositional data determined by the various techniques for the four filler wires, it was determined that the melting of the filler wire would produce a microstructure that would contain a nominal 10 vol% of ferrite. This agrees with the available literature of the expected delta ferrite content of a 300 series austenitic filler wire.[10,16,26,30,98–103]

Chapter 3: Characterization and Testing of Welded Plates

3.1. Introduction

Weld plate fabrication was performed by High Steel Structures LLC in accordance with AASTHO/AWS D1.5 SAW B-U3c-S for the sixteen Group 1 (1/2" thick plates) and the twelve Group 2 (1" thick plates) and B-U2-s for the two Group 3 (1" thick PQR plates), shown in Figure 3.1.[104] The aforementioned 3/32" filler wires were used to weld the 50CR base plates together: 309L, 309LSi, and 316L solid welding wire, and 309LC metal cored welding wire. Lincolnweld 880M® flux was used for all of the welding.

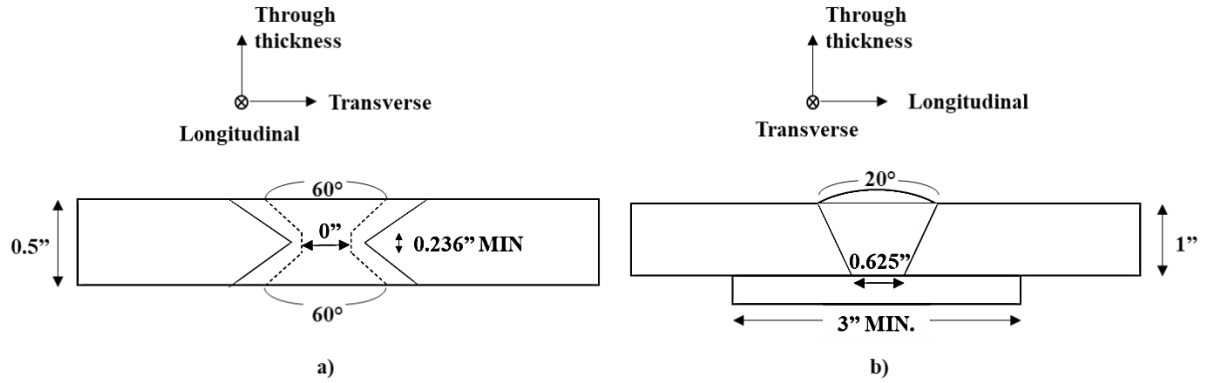

Figure 3.1. a) *Schematic of the welding joint used for the welding of the sixteen Group 1 (1/2" thick) and twelve Group 2 (1" thick) plates.* ***b)*** *Schematic of the welding joint used for the welding of the two Group 3 (PQR) plates.*

Based on published literature and communications with the various industry experts, heat inputs of 50 kJ/in and 75 kJ/in in combination with maximum interpass temperatures of 125 °F, 300 °F, and 450 °F were selected for welding the Group 1 plates.[72,74] The lowest interpass temperature was chosen based on prior welding experience from the Route 340 Bridge in Waynesboro, VA (from Figure 1.2b); when fabricating multi-pass welds, the temperature of the plate was approximately 125 °F after the initial pass, thus was chosen in this study to represent the 50CR producer's recommended maximum interpass temperature.[74] According to communications with the Virginia DOT, 300 °F has often been used in the welding practice of

50CR. However, work performed by Oregon showed 1" thick plates welded with a heat input of 54 kJ/in and a maximum interpass temperature of up to 450 °F have been proven to be able to pass the PQR plate testing.[39] In order to achieve an interpass temperature of 450 °F, the fabricator heated the welded plate with an oxyacetylene torch. Because previous published data was obtained from testing on 1" thick material, the results from this study expands the knowledge base for the expected results for varying welding parameters used on 50CR.

Heat inputs of 70 kJ/in and 90 kJ/in and maximum interpass temperature of 300 and 450 °F were used on the Group 2 plates. These parameters represent an increase in the heat inputs when compared to previous literature (54 kJ/in as seen in the Oregon DOT study), while keeping the maximum interpass temperatures the same.[39] Two 1" thick plates (Group 3) were prepared and tested in accordance with the AASTHO/AWS D1.5 Welding Procedure: Specification Plate A fabrication requirements using 309L and 309LC with a maximum heat input of 90 kJ/in and a maximum interpass temperature of 450 °F.[61] A list of all the combinations of parameters employed in this study can be found in Table 3.1.

Table 3.1. *List of welding parameter combinations used in the study with the second batch of 1/2" plates received indicated by the asterisk.*

Group	Plate Thickness (inch)	Filler Wires Used	Heat Input (kJ/in)	Maximum Interpass Temp. (°F)
1*	½	309L, 309LC, 309LSi, 316L	50	300
1	½	309L, 309LC, 309LSi, 316L	75	125
1*	½	309L, 309LC, 309LSi, 316L	75	300
1	½	309L, 309LC, 309LSi, 316L	75	450
2	1	309L, 309LC, 309LSi, 316L	70	300
2	1	309L, 309LC, 309LSi, 316L	90	300
2	1	309L, 309LC, 309LSi, 316L	90	450
3 (PQR)	1	309L, 309LC	90	450

The Group 1 plates were received at two separate occasions and is indicated by the asterisk shown in Table 3.1. This led to a slight difference in the 50CR base plate composition as

the welding performed. All but one of the Group 1 plates passed visual inspection and radiographic testing in accordance with AASHTO/AWS D1.5 Section 6C. Welded plates are required to be free of any cracking or visible piping porosity, limited internal porosity, and have thorough fusion between adjacent weld layers, and between the weld metal and the base plate.[61] The Group 1 plate that failed this requirement (309LC, welded with a heat input of 75 kJ/in, and a maximum interpass temperature of 300 °F) contained a 5/64" (2 mm) weld gap, which was determined to be due to an improper joint fit up. Mechanical testing of this welded plate was still performed to determine if it would still meet the mechanical property requirements. Those results are not included in the main statistical analysis of the data.

A comparison of the welding parameters utilized on the Group 3 plates is presented in Table 3.2. A lower heat input was used for both the root and cap weld passes, but they are not included in the heat input calculation per AASHTO/AWS D1.5.[61] Less passes were required to weld the plates using the 309LC filler wire because it has a higher overall deposition rate and lower fume and spatter.[49,52–54] Visual, radiographic, and ultrasonic inspection were performed on both PQR plates in accordance to AASHTO/AWS D1.5 [61] and no defects were reported.

It should be noted that the wire feed speed employed for the cored wire was reported by the girder fabricator to be 53% faster than that of the solid wire (275 vs. 180 inches per minute) for the welding of the Group 1 plates. Welding of the PQR plates (Group 3) with cored wire was performed with wire feed speeds, which were 31% faster than the solid filler wire (225 vs. 172 inches per minute). This is necessary because the cored wire has a lower mass density and faster melting rate due to the path that the arc current takes.[49,50,52–54] For the multi-pass welds, the use of 309LC required two to three less weld passes to accomplish the same weld. This is due to the higher deposition rate and the lower spatter and fume generation (leading to possible loss of

alloying elements through evaporation) of metal cored wire versus solid wire. [49,50,52–54] The voltage, amperage, and travel speeds were kept constant between the weld plates as much as possible.

Table 3.2. *Welding parameter data provided by girder fabricator for the welding of Group 3 plates*

Welding Parameter	309L-90 kJ/in-450 °F	309LC-90 kJ/in-450 °F
Total Number of Weld Passes	12	10
Average Heat Input (kJ/in)	88.3	88.1
Average Current (A)	566	514
Average Voltage (V)	39	40
Average Travel Speed (in/min)	15	14
Average Feed Speed (in/min)	172	225

In a prior study of 3CR12 CVN samples, it was observed that the plates are prone to delamination-type failure, where secondary cracks run parallel to the plane of the plate.[9] This observation suggests that 3CR12 and similar alloys such as 50CR may be susceptible to lamellar cracking during fillet welding of T-joints typical of welded plate girders and for which the Cranfield test was developed.[59] However, Grobler investigated this possibility and, yet, did *not* observe lamellar cracking in his study of 3CR12.[9] However, Grobler still indicated that it is an issue worthy of further consideration and suggests a means of exploring it. Whether or not this possible failure mode would affect the performance of 50CR structural members is beyond the scope of the thesis. Notably, the present investigation of butt-joints revealed no cracks *of any sort* in the as-welded plates.

3.2. Experimental Procedure

3.2.1 Compositional Analysis

EDS area scans were used to estimate the composition of fifteen areas of 400 by 500 microns on the transverse face starting from the edge of the weld and moving towards the center of each Group 1 plate using a scribed line and micro-hardness indention points, spaced 0.025”

apart, as markers. The location of the indention points was 0.125” from each edge of the sample, as shown in Figure 3.2.

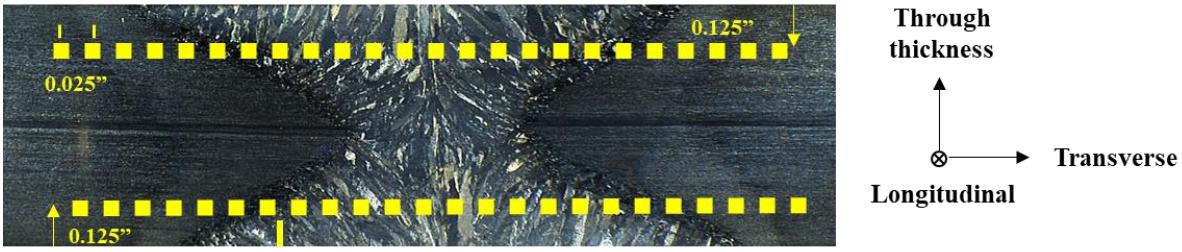

Figure 3.2 *Welded 1/2” plate with representative scribe (shown by the line) and location of micro-Vickers hardness indention points.*

The compositions obtained using EDS were used to estimate the amount of dilution (D) of Cr and Ni using Equation 3.1, where C_{fz}, C_{bm}, C_{fm} are the concentrations of an element in the fusion zone, base metal, and filler metal respectively.[62] The concentrations of these two elements were used because they had the largest concentration difference between the base metal and the filler wire, thus decreasing the uncertainty in the dilution estimates.

$$D = \frac{C_{fz} - C_{fm}}{C_{bm} - C_{fm}}$$

Equation 3.1. *The dilution value (D) is calculated by taking the ratio of the difference between the composition of one specific element (Cr, Ni, etc.) in the fusion zone (C_{fz}) and the filler metal (C_{fm}) to the difference in composition between the base (C_{bm}) and filler metals (C_{fm}).*[62]

3.2.2 Predictive Modeling

The Rosenthal model was utilized to predict the time that the weld plate would be in the 1472 °F (800 °C) to 932 °F (500 °C) range ($\Delta t_{8\text{-}5}$). Equation 1.3 was applied to determine whether the thin (2D heat flow) or thick plate (3D heat flow) conditions should be applied. Once the critical thickness determined that all of the plates used in this study were greater than the thickness of the plate used, the relevant thin-plate equations (Equation 1.4, 1.8 and 1.10) were applied to determine the peak temperature as a function of distance away from the weld centerline, the $\Delta t_{8\text{-}5}$, and the time versus temperature curve at a specific distance away from the

weld centerline. In order to calculate the values, the imperial units in this research were converted to metric and the thermal properties of 50CR were assumed to be the same as that of 3CR12. The specific gravity multiplied by the specific heat (ρC) and thermal conductivity of 3CR12 were taken to be 3.93E6 J/m^{3}K and 26 W/mK respectively.[45] The pre-heat temperature (T_0) was taken to be 298K or 76.76 °F since the weld plate was not preheated for the initial pass. However, for the subsequent passes, the pre-heat temperature was taken to be the maximum interpass temperature for the specific welding parameter combination (plate thickness, heat input, and maximum interpass temperature).

The semi-quantitative compositions determined by the EDS area scans of the Group 1 plates used to calculate the Cr_{eq} and Ni_{eq} values. They were then entered into the Schaeffler diagram Excel spreadsheet to more accurately predict the microstructure of the fusion zone.

3.2.3 Microstructural Analysis

Four inches were cut and discarded from either side of the Group 1 and 2 plates to ensure that the steady-state condition for submerged arc welding had been reached. All of the weld cross-section samples (the transverse face) were ground and polished to a 0.05-micron finish. The welded samples were etched using waterless Kalling's No. 2 reagent, prepared in accordance with ASTM E407.[83] This was a mixture of 5 g of cupric (copper II) chloride, 100 mL of hydrochloric acid, and 100 mL of ethanol. An inverted optical microscope was used to take micrographs of the various microstructural regions. ImageJ was used post process the micrographs to determine amount of ferrite present. OM micrographs were converted to a binary black and white 2D image, by thresholding the gray scale image to have the ferrite appear as black and the austenite white. The pixels of the ferrite were calculated and converted to an area percentage. This area ferrite content was assumed to be equivalent to the volume percentage of residual δ-ferrite in the fusion zone. Scribed lines and Vickers micro-hardness indention points,

shown in Figure 3.2, were used to ensure that the same region was analyzed with EDS. Three macro-etch samples were prepared in accordance with AASHTO/AWS D1.5 Section 5.18.2 and analyzed according to Section 5.19.3 for each plate in Group 3 by Lehigh Testing Laboratories.[61]

One transverse face sample from each of the welded Group 3 plates, ground and polished to a 1200 grit finish, and analyzed using either a Panalytical X'pert Pro multipurpose X-ray diffractometer or a Malvern-Panalytical Empyrean multipurpose X-ray diffractometer. GSAS-II was used to perform Rietveld refinement on the diffraction patterns and to estimate the volume fractions of the phases present.

3.2.4 Micro-hardness Testing

Two lines of data were taken across the weld 0.125" from each edge of each of the Group 1 welded plates, as seen in Figure 3.2. One line of data was taken across the weld 0.25" from the one of the edges of each of the Group 2 welded plates. The data was collected using a Bühler Micromet 5101, a load of 500 g, and a loading time of 15 seconds.

2.5 Uniaxial Tension Testing

Tensile testing was performed on each of the Group 1 plates in the T orientation with the weld placed in the middle of the gage length. Samples were tested in sets of five on a servo-hydraulic controlled 55-kip capacity MTS Model #319.25 at the Virginia Transportation Research Council. A laser extensometer and reflective tape was used to measure the gauge length initially and during the elongation during the testing. In the same way, three samples, shown in Figure 3.3b, from Group 2 plates were tested in the T orientation using a servo-hydraulic controlled 110-kip capacity MTS Model #312.31 at the Turner-Fairbank Highway Research Center. The testing programs are shown in Table 3.3 and 3.4 respectively. The initial speed for the testing program at Turner-Fairbank was determined by multiplying parameter A (3.25" in this case) by 0.015"/60 to obtain the speed in inches per second. Finally, one all-weld-

metal tensile and two reduced-section tensile samples were machined and tested from each Group 3 plate in accordance with AASHTO/AWS D1.5 Section 5.18.1 and Section 5.18.4 by Lehigh Testing Laboratories.[61] The samples were then analyzed in accordance with Section 5.19.1 and 5.19.4, which leads to the reporting tensile strength, reduction in area, and percent elongation for both types of tensile samples and yield strength for just the all-weld-metal tensile sample. Because the yield strength was not provided by the testing facility, the data was obtained and analyzed using the same methods as for the testing performed at the University of Virginia using the conventional 0.2% offset method.

Table 3.3. *Tensile testing program used at the Virginia Transportation Research Council to test the 0.5" thick welded samples.*

Speed (in/s)	Strain Range
0.0005	0.0 – 0.05
0.001	0.05 – 0.10
0.002	0.10 – 0.15
0.004	0.15 – 0.20
0.008	0.20 – end

Table 3.4. *Tensile testing program used at the Turner-Fairbank Highway Research Center to test the 1" thick welded samples.*

Speed (in/s)	Strain Range
0.0008125	0 - 0.015
0.00089375	0.015 - 0.020
0.001161875	0.020 - 0.025
.001742813	0.025 - 0.030
0.002962781	0.030 - 0.035
0.005925563	0.035 – end

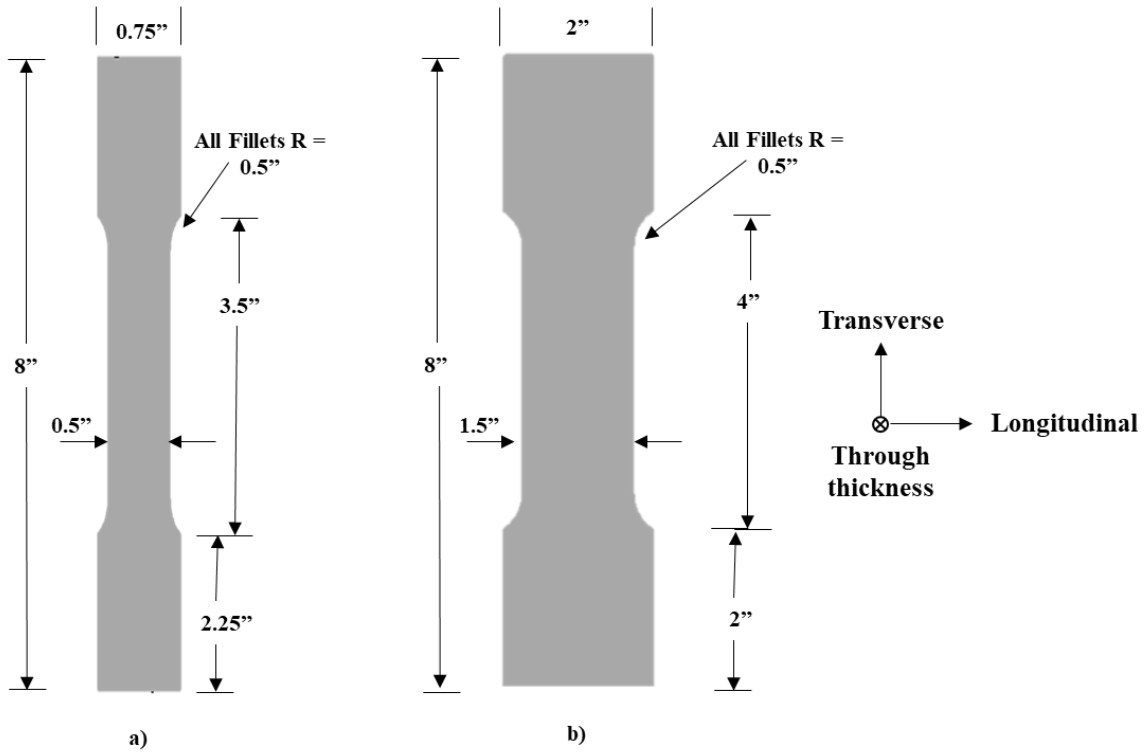

Figure 3.3. *The sample geometries of the reduced area weld tension samples for* ***a)*** *Group 1 samples and* ***b)*** *Group 2 samples. All of the units are in inches.*

3.2.6 Charpy V-Notch Impact Testing

Twenty-four full-size weld CVN samples were machined from Group 1 plates in the TL orientation and tested on a Tinius Olsen 406.7 J (300 ft·lbf) capacity Charpy testing machine at the Turner-Fairbank Highway Research Center in accordance with ASTM E23.[84] The number of samples tested at -20°F and the additional test temperatures explored is presented in Table 3.5. In summary, five to ten samples were tested at -20°F for each Group 1 plate and two to three additional samples were tested at each of the following temperatures for the highest heat input and maximum interpass combination: -100, -60, -30, -10, 10, 40, 70, and 150 °F. Testing temperatures below room temperature were achieved using a machine-controlled ethanol bath in accordance to ASTM E23.[84] Testing at 150 °F was achieved by heating the samples in hot water and used to determine an upper shelf impact energy. Five full-size welded CVN samples were machined from each Group 2 plate and tested in accordance to ASTM E23 by Chicago Spectro

Service Laboratory Inc.[84] Finally, five full-size welded CVN samples were machined from each Group 3 plate and tested in accordance to AASHTO/AWS D1.5 Section 5.19.5 by Lehigh Testing Laboratories.[61]

Table 3.5. *List of welding parameter combinations used for the Group 1 plates, along with the number of specimens tested at -20 °F and additional temperatures at which 2 or 3 samples were tested. Ten full-sized welded CVN samples from the defective plate were also tested and will be discussed separately.*

Welding Parameters	-20 °F	Additional Test Temperatures
309L-50 kJ/in-300 °F	10	N/A
309L-75 kJ/in-125 °F	10	N/A
309L-75 kJ/in-300 °F	10	N/A
309L-75 kJ/in-450 °F	10	-100 °F, -60 °F, -30 °F, -10 °F, 10 °F, 40 °F, 70 °F, and 150 °F
309LC-50 kJ/in-300 °F	10	N/A
309LC-75 kJ/in-125 °F	10	N/A
309LC-75 kJ/in-450 °F	10	-100 °F, -60 °F, -30 °F, -10 °F, 10 °F, 40 °F, 70 °F, and 150 °F
309LSi-75 kJ/in-125 °F	5	N/A
309LSi-75 kJ/in-450 °F	5	-100 °F, -60 °F, -30 °F, -10 °F, 10 °F, 40 °F, 70 °F, and 150 °F
316L-75 kJ/in-125 °F	5	N/A
316L-75 kJ/in-450 °F	5	-100 °F, -60 °F, -30 °F, -10 °F, 10 °F, 40 °F, 70 °F, and 150 °F

3.2.7 Side Bend Testing

Four side-bend test samples were machined from each Group 3 plate and tested in accordance to AASHTO/AWS D1.5 Section 5.19.2 by Lehigh Testing Laboratories. [61]

3.2.8 Fractography

OM was used to characterize the Group 1 CVN samples welded using a heat input of 75 kJ/in and a maximum interpass temperatures 450 °F at the highest, lowest, and AASHTO/AWS D1.5 testing temperatures. The conclusions made from optical microscopy were then confirmed using SEM. All of the samples were sonicated in methanol for ten minutes with the fracture side facing up before SEM was performed to minimize contamination.

3.3. Results

3.3.1 Compositional Analysis

The average composition determined for the fusion zone of each set of Group 1 plates is presented in Table 3.6. The average for each filler wire, ignoring the contributions of the heat input and maximum interpass temperature, is shown in bold. The compositions within each plate's fusion zone was determined to be within 0.5 wt% of each other. This indicates that the composition within the fusion zone was overall uniform. These calculated values of dilution are consistent with available literature on submerged arc welding dilution.[4,7,24,29]

Table 3.6. *Average of sixty (fifteen data points for four sets of welding parameters using the same filler wire) semi-quantitative Group 1 fusion zone compositions determined by EDS is shown in bold. The average of fifteen data points is shown for each specific weld plate as well. The values are given in wt%.*

Filler Metal	Heat Input (kJ/in)	Maximum Interpass Temp. (°F)	Fe	Cr	$D\%_{Cr}$	Ni	$D\%_{Ni}$	Mn	Si	Mo
309L	**50**	**300**	70.1	19.6	31.3	8.3	39.6	1.4	0.5	0
309L	**75**	**125**	75.4	17.1	52.3	5.6	60.2	1.4	0.5	0
309L	**75**	**300**	72.9	18.3	42.9	6.9	50.5	1.4	0.6	0
309L	**75**	**450**	75.8	16.9	54.1	5.4	62.0	1.4	0.5	0
Average	**N/A**	**N/A**	**73.6**	**18.0**	**45.1%**	**6.5**	**53.0%**	**1.4**	**0.5**	**0**
309LC	**50**	**300**	68.0	20.9	23.1%	9.2	36.8%	1.4	0.7	0
309LC	**75**	**125**	71.9	19.0	38.2%	7.1	51.6%	1.5	0.5	0
309LC	**75**	**300**	71.1	19.2	36.3%	7.6	47.9%	1.3	0.7	0
309LC	**75**	**450**	71.3	19.2	36.2%	7.4	49.9%	1.5	0.6	0
Average	**N/A**	**N/A**	**70.7**	**19.5**	**34.2%**	**7.7**	**47.2%**	**1.4**	**0.6**	**0**
309LSi	**50**	**300**	73.4	17.9	50.3%	6.4	54.3%	1.6	0.7	0
309LSi	**75**	**125**	74.3	17.4	53.8%	6.0	57.1%	1.6	0.6	0
309LSi	**75**	**300**	72.9	18.0	49.0%	6.7	51.7%	1.6	0.7	0
309LSi	**75**	**450**	72.9	18.1	48.7%	6.7	52.0%	1.7	0.7	0
Average	**N/A**	**N/A**	**73.4**	**17.8**	**50.4%**	**6.4**	**53.8%**	**1.6**	**0.7**	**0**
316L	**50**	**300**	72.5	17.0	30.9%	7.4	38.8%	1.4	0.6	1.1
316L	**75**	**125**	77.1	15.1	54.6%	4.9	60.5%	1.5	0.5	0.9
316L	**75**	**300**	72.1	17.3	27.6%	7.6	36.8%	1.4	0.6	1.1
316L	**75**	**450**	76.5	15.2	52.7%	5.2	57.5%	1.5	0.5	1.1
Average	**N/A**	**N/A**	**74.5**	**16.1**	**41.4%**	**6.3**	**48.4%**	**1.5**	**0.5**	**1.1**

3.3.2 Predictive Modeling

Because the calculated critical thickness was greater than the plate thickness used (shown in Table 3.7), the Rosenthal thin plate equations were used to calculate the peak temperature in the fusion zone as a function of the distance from the weld centerline, shown in Figure 3.4 as well as the Δt_{8-5}, reported in Table 3.7. Because it is defined as the time spent between 800 and 500 °C, a low Δt_{8-5} value is indicative a fast cooling rate. A similar trend occurs in the peak temperature calculation, where the combination of 1" and 70 kJ/in shows the lowest value, followed by 1"- 90 kJ/in, 1/2"- 50 kJ/in, and 1/2" – 70 kJ/in. The preheat temperature for these calculations was assumed to be 298K, or room temperature. This means that these calculations are only valid for the initial welding pass laid down on each plate.

Table 3.7. *Using Equation 1.6, the Δt_{8-5} was calculated for each welding heat input-plate thickness combination. It can be seen that ranking for the cooling rate (from fastest to slowest) goes as follows: 1" – 70 kJ/in, 1" – 90 kJ/in, 1/2" – 50 kJ/in, 1/2" – 75 kJ/in. The preheat temperature was assumed to be 298 K or room temperature.*

Parameter with Mixed Units in **Bold**	1.969E6 J/m (**50 kJ/in**)	2.953E6 J/m (**75 kJ/in**)	2.756E6 J/m (**70 kJ/in**)	3.543E6 J/m (**90 kJ/in**)
Critical Thickness in mm (**inch**)	29.2 (**1.15**)	35.7 (**1.41**)	34.5 (**1.36**)	39.1 (**1.54**)
Thickness of Plate in mm (**inch**)	12.7 (**1/2**)	12.7 (**1/2**)	25.4 (**1.0**)	25.4 (**1.0**)
Δt_{8-5} in sec	52	117	25	42

Similar calculations were applied assuming that the maximum interpass temperature was equal to the preheat temperature for Equations 1.4, 1.8 and 1.10. With an increase in the preheat temperature, the critical thickness as well as the Δt_{8-5} increased as expected. All of the welding parameter combinations remained in the thin plate 2-D regime of the Rosenthal calculations.

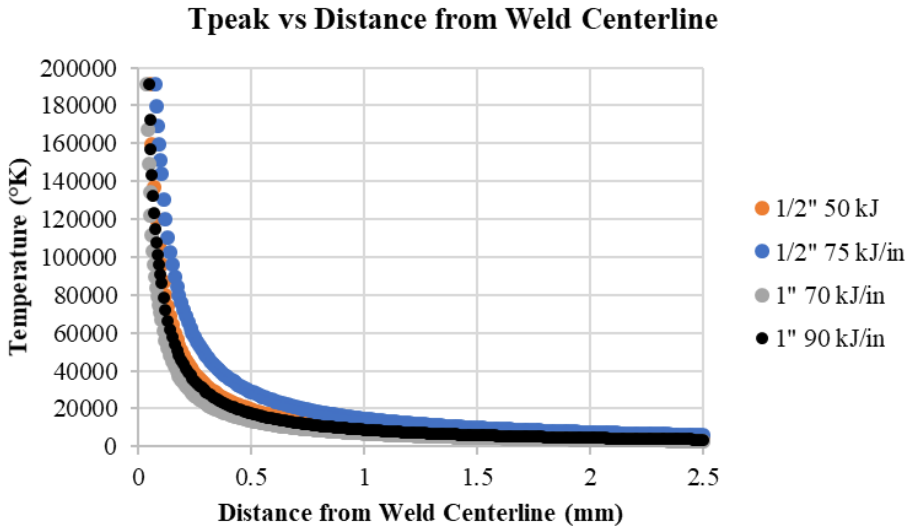

Figure 3.4. *Using Equation 1.4, the peak temperature of each welding heat input-plate thickness combination is plotted against the distance from the weld centerline (up to 0.1"). It can be seen that ranking follows the same trend as the $\Delta t_{8\text{-}5}$ (from lowest to highest peak temperature at a given distance away from the weld centerline): 1" – 70 kJ/in, 1" – 90 kJ/in, 1/2" – 50 kJ/in, 1/2" – 75 kJ/in.*

A prediction of the fusion zone phase content can be made by plotting the Cr_{eq} and Ni_{eq} compositions of the filler metal and the base material (50CR) using the Schaeffler diagram spreadsheet (Figure 3.5). By connecting the compositions, a dilution line with all of the possible microstructures is revealed. For this study, the dilution line includes regions with (a) austenite and ferrite (little dilution), (b) a combination of austenite, ferrite, and martensite, or (c) martensite and ferrite (in cases of extreme dilution). By plotting the fusion zone EDS data, the weld microstructure was predicted to land mainly in the three phase region of austenite, ferrite, and martensite, with specifically about 20-30% ferrite.[25,27,29] The plate welded using 309LC, with a heat input of 50 kJ/in and a maximum interpass temperature of 300 °F, however, was found to be in just the austenite and ferrite region.

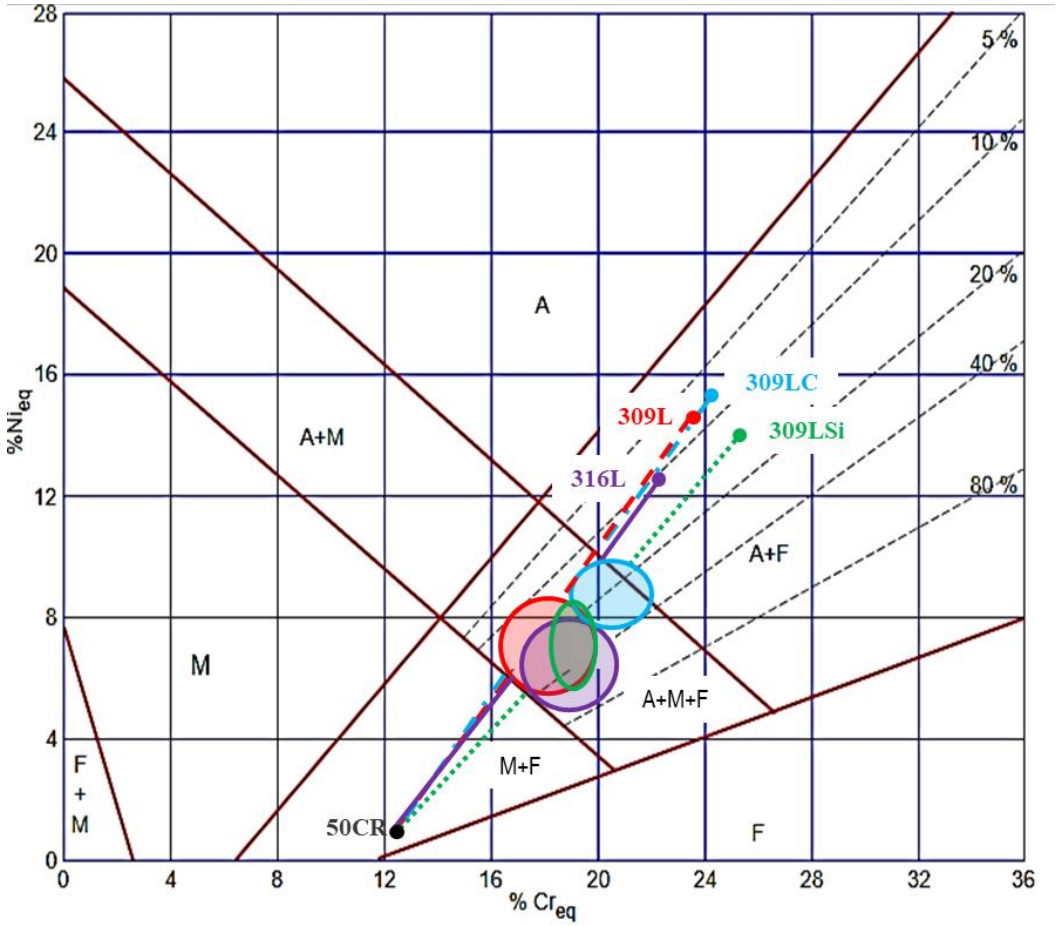

Figure 3.5. *Schaeffler diagram (after reference 29) including the compositions of the filler wires used in this study, dilution lines, and the ranges of measured compositions of the 309L (red), 309LSi (green), 309LC (blue), and 316L (purple) plotted as ellipses which fall squarely in the region labeled A+M+F (austenite + martensite + ferrite).*

Based on the Cr_{eq}/Ni_{eq} values and the solidification model shown in Figure 1.7b, the solidification mode for all of the fusion zones is predicted to involve the formation of primary δ-ferrite, which will then undergo a solid-state transformation to austenite (termed the F solidification pathway in the Chapter 1).[26,56] This occurs due to the high amount of ferrite stabilizers relative to the amount of austenite stabilizers.

Table 3.8. *The range of results is shown for each specific Group 1 weld plate. The solidification mode was predicted using Figure 1.7b which was obtained from Mateša et al.*[26] *All of the fusion zone phase content predictions were shown to be in the austenite, ferrite, and martensite region except for the plate welded using 309LC, with a heat input of 50 kJ/in and a maximum interpass temperature of 300 °F, which was located in the austenite and ferrite region. The WRC-92 calculations ignore the Si wt% for* Cr_{eq} *and Mn wt% for* $Ni_{eq,}$ *which are taken into account for the Schaeffler calculations.*

Filler Metal	Heat Input (kJ/in)	Maximum Interpass Temp. (°F)	Fusion Zone Phase Content (vol% F)	Cr_{eq}/Ni_{eq} (Schaeffler)	Cr_{eq}/Ni_{eq} (WRC-92)	Predicted Solidification Mode
309L	**50**	**300**	20 – 23%	2.2 – 2.3	2.3 – 2.4	F
309L	**75**	**125**	28 – 31%	2.8 – 2.9	3.0 – 3.1	F
309L	**75**	**300**	24 – 26%	2.5 – 2.6	2.6 – 2.7	F
309L	**75**	**450**	28 – 32%	2.9 – 3.0	3.1 – 3.2	F
309LC	**50**	**300**	21 – 23%	2.2	2.2 – 2.3	F
309LC	**75**	**125**	26 – 28%	2.5 – 2.6	2.6 – 2.7	F
309LC	**75**	**300**	23 – 27%	2.4 – 2.5	2.5 – 2.6	F
309LC	**75**	**450**	25 – 28%	2.4 – 2.5	2.6 – 2.7	F
309LSi	**50**	**300**	24 – 30%	2.5 – 2.7	2.6 – 2.9	F
309LSi	**75**	**125**	24 – 31%	2.6 – 2.8	2.7 – 3.0	F
309LSi	**75**	**300**	23 – 31%	2. 4 – 2.8	2.5 – 3.0	F
309LSi	**75**	**450**	23 – 28%	2.5 – 2.7	2.6 – 2.8	F
316L	**50**	**300**	17 – 22%	2.3 – 2.4	2.4 – 2.5	F
316L	**75**	**125**	23 – 32%	2.8 – 3.1	3.1 – 3.4	F
316L	**75**	**300**	19 – 21 %	2.3 – 2.4	2.4 – 2.5	F

3.3.3 Microstructural Analysis

Microstructural analysis of both Group 1 and 2 welded samples revealed four distinct microstructural zones. These four zones are the fusion zone, the coarse-grained heat affected zone (coarse HAZ), the fine-grained heat affected zone (fine HAZ), and the unaffected base material, shown in Figure 3.6. This is consistent with previous research performed on 50CR[74] and its legacy alloy, 3CR12.[9,99] Representative micrographs of each region can be seen in Figure 3.7. Image processing of the fine HAZ revealed that the ferrite content remained at ~10 vol%, and the size of the martensite bands remained at 5 to 50 microns. Metallographic analysis of the fusion zones revealed various particles with sizes up to tens of micrometers. EDS revealed that

these particles were Al based, and are likely a result of the melting base material. These particles were of varying size and no correlation with filler wire, heat input, or maximum interpass temperature was observed.

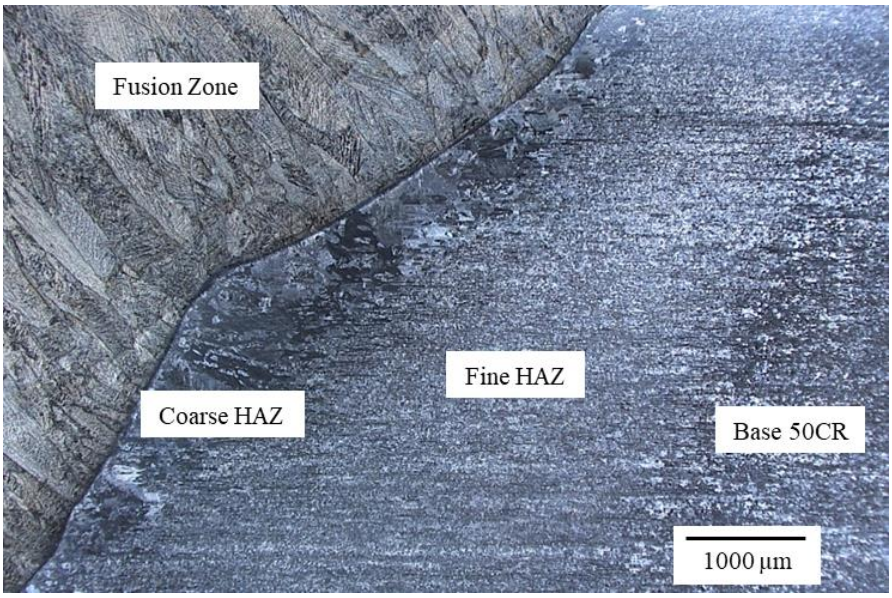

Figure 3.6. *Typical welded plate microstructure for all of the filler wires, taken using 35X magnification and dark field OM*

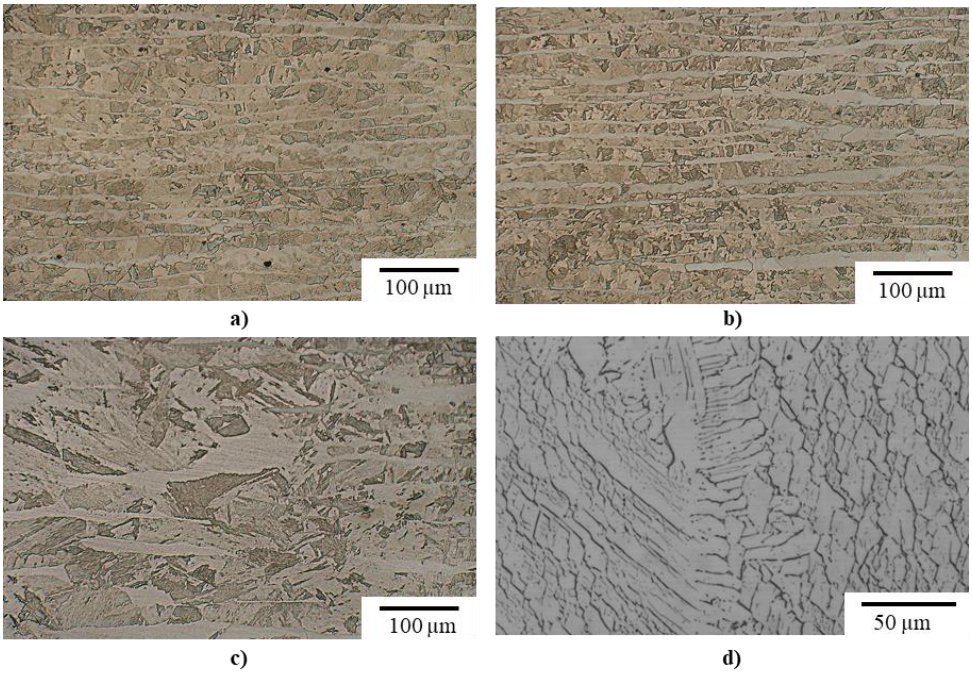

Figure 3.7. *Typical welded plate microstructure for each region:* ***a)*** *unaffected base material (50CR)* ***b)*** *fine HAZ* ***c)*** *coarse HAZ* ***d)*** *fusion zone.* ***a – c)*** *show a mixture of martensite and ferrite, while the fusion zone contains residual ferrite within an austenite matrix.*

Etching of the second batch of the Group 1 plates revealed that more than two weld passes, with as many as eight, were used to weld the plates with a maximum interpass temperature of 300 °F. This was likely due to welder variability and is indicative of what the properties would be if a welding defect has to be ground out and the plate re-welded. Although each distinct weld pass could be determined by the naked eye after etching, at the microscopic level, there was not a clear distinction in the microstructure and very little variance in the composition (within the expected variability associated with EDS).

Austenitic filler wires are designed to have at least 5 vol% residual δ-ferrite to prevent hot cracking of the austenitic weld.[26] No cracking of any sort was found in the welded plates in the present study. Kalling's No.2 etchant preferentially attacks ferrite more readily than austenite[83]. Post-image analysis of the optical micrographs of the etched samples was able to differentiate between the two phases (again by thresholding of image, this time coloring ferrite black and austenite white in the binary 2D image). Based a two-sided T-test, it can be stated with 95% confidence that neither raising the heat input nor the maximum interpass temperature causes a statistically significant change in the amount of residual delta ferrite in the fusion zone in the Group 1 plates. The nominal ferrite content in the fusion zones is presented in Table 3.9. The rank order in ferrite content is the same for the two plate thicknesses: 316L < 309L = 309LSi < 309LC, all of which are higher than the minimum δ-ferrite (5 vol%) required.

Table 3.9. *Average ferrite content in the fusion zone for plate groups 1 and 2 determined by ImageJ analysis of OM micrographs*

Weld Filler Wire **Plate Group**	**316L** **(vol. % ferrite)**	**309L** **(vol. % ferrite)**	**309LSi** **(vol. % ferrite)**	**309LC** **(vol. % ferrite)**
Group 1 (1/2")	10	12	12	17
Group 2 (1")	15	18	18	26

The three macro-etches from each PQR test plate were found to be acceptable. The weld fusion zone was free of cracks and porosity, and there was thorough fusion between adjacent layers of weld metal as well as between the weld metal and the base material.

Figure 3.8 reveals that welds produced in Group 1 plates using the metal cored wire (309LC) have a somewhat finer, and less aligned macrostructure, as compared to the welds produced using conventional solid filler wire (a, c, d). Higher magnification images in Figure 3.9 further emphasize the fact that the cored wire induces a finer microstructure in the fusion zone, indicative of a faster cooling rate. The micrographs illustrate that the use of the metal cored wire results in a finer structure, both at the level of the columnar prior δ-phase grains (Figure 3.8) and in the fineness of the Widmanstätten structure of the austenite phase which results from solid state phase transformation (Figure 3.9).

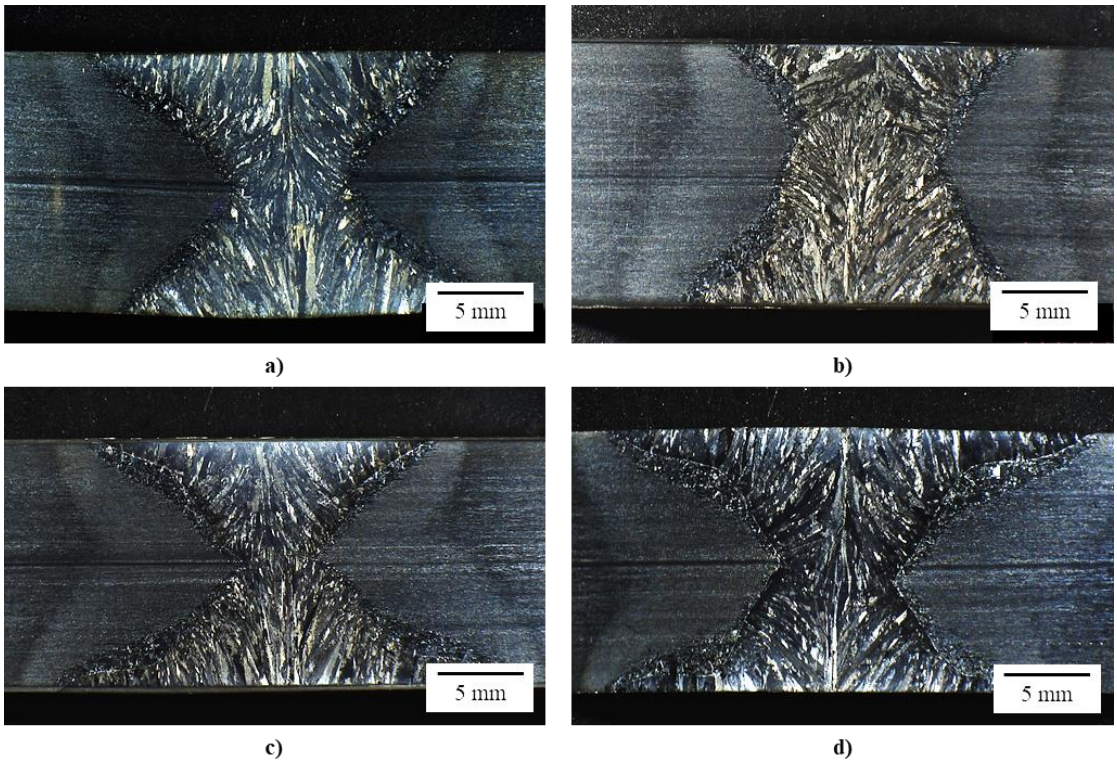

Figure 3.8. *Representative macro-etch images of the fusion zone from welds produced using a) 309L, b) 309LC, c) 309LSi, and d) 316L which illustrates a more irregular microstructure along the centerline of the weld in the case of the 309LC.*

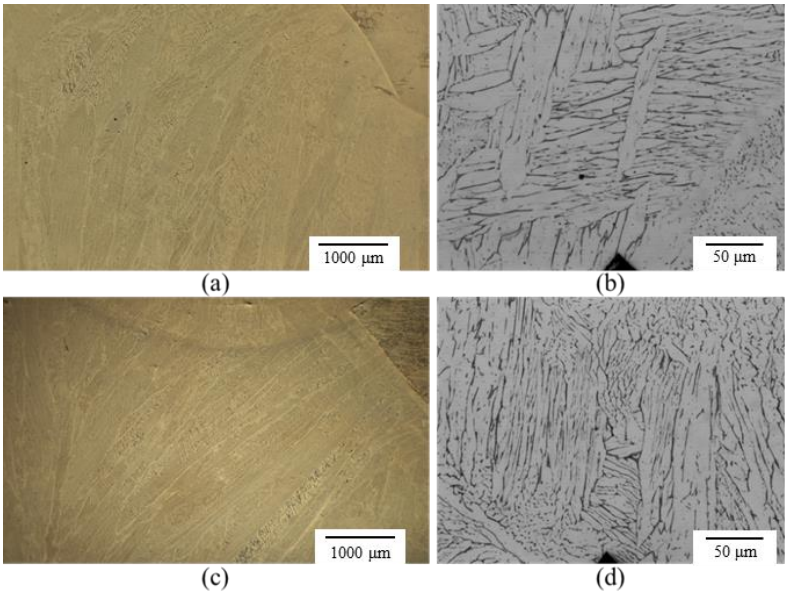

Figure 3.9. *Representative microstructural images of the fusion zones of welds in 1/2" plates using 309L (**a & b**) and 309LC (**c & d**) filler metals with a heat input of 75 kJ/in and an interpass temperature of 125 °F (**a & c**) and 450 °F (**c & d**). The micrographs illustrate that use of the cored wire results in a finer structure, both at the level of the columnar prior δ-phase grains (**a & c**) and in the fineness of the Widmanstätten structure of the austenite phase which results from solid state phase transformation (**b & d**)*

Both FCC γ-austenite and BCC δ-ferrite were determined by XRD to be present in the fusion zone, as shown in Figure 3.10. As mentioned previously, austenitic filler wires are typically designed to retain at least 5 vol% δ-ferrite, to prevent solidification cracking. The larger δ-ferrite (bcc_{110}) peak in the diffraction pattern of the weld produced using 309LC confirms that there is a higher volume fraction of ferrite retained when compared to conventional solid 309L filler wire (Figure 3.10). Analysis of the XRD patterns of the Group 3 fusion zones revealed a residual δ-ferrite content of 22.1 vol% for the plate welded using 309L and 39.4 vol% for the plate welded using 309LC. This is comparable to data from the Group 2 plates welded using the same welding parameters obtained using conventional metallography.

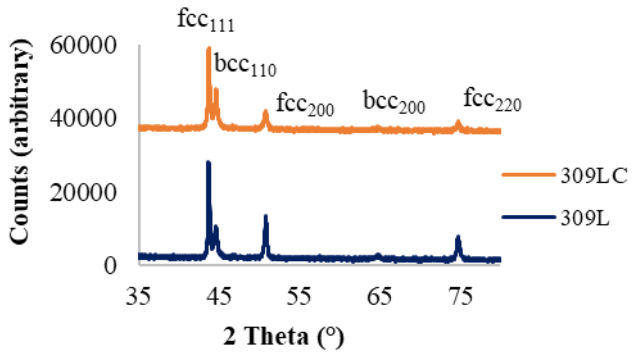

Figure 3.10. *XRD pattern of the fusion zone of Group 3 plates having peaks from both austenite and retained δ-ferrite.*

3.3.4 Micro-hardness Testing

Microhardness data taken from welded samples of Group 1 all reveal regions of enhanced hardness after welding. The higher hardness in the fine HAZ region of all the welds is due to precipitation of carbides.[11,89] Figure 3.11 reveals an interesting distinction between the plates welded using the solid filler wires (309L, 309LSi, and 316L) and the metal cored wire (309LC). The plates welded with a solid filler wire had the highest hardness values (ranging from 300 – 350 HV) in the fusion zone, and a narrow region of depressed hardness right outside the fusion zone in the HT-HAZ. On the other hand, the hardness of the fusion zone resulting from the use of 309LC was only about 200 HV, similar to that of the base metal. The highest region of the plated welded with 309LC was the fine HAZ, ranging from 250 – 300 HV.

Based on the micro-hardness results on the Group 1 samples welded using a maximum interpass temperature of 300 °F, it was clear that these samples had been welded with more passes than the other samples. Although this was not originally planned for and occurred due to welder variability, this represents a welded plate that has been repaired due to a detected weld flaw. The highest hardness found in these samples was approximately 400 HV, only slightly higher than what was typically found in the fusion zone for solid wire. Typical microhardness values for the Group 2 samples were in the range of 300 – 375 HV, consistent with the fine HAZ

hardness values of Group 1 plates welded using a maximum interpass temperature of 300 °F, i.e. more than two weld passes were used to fill the double V-groove.

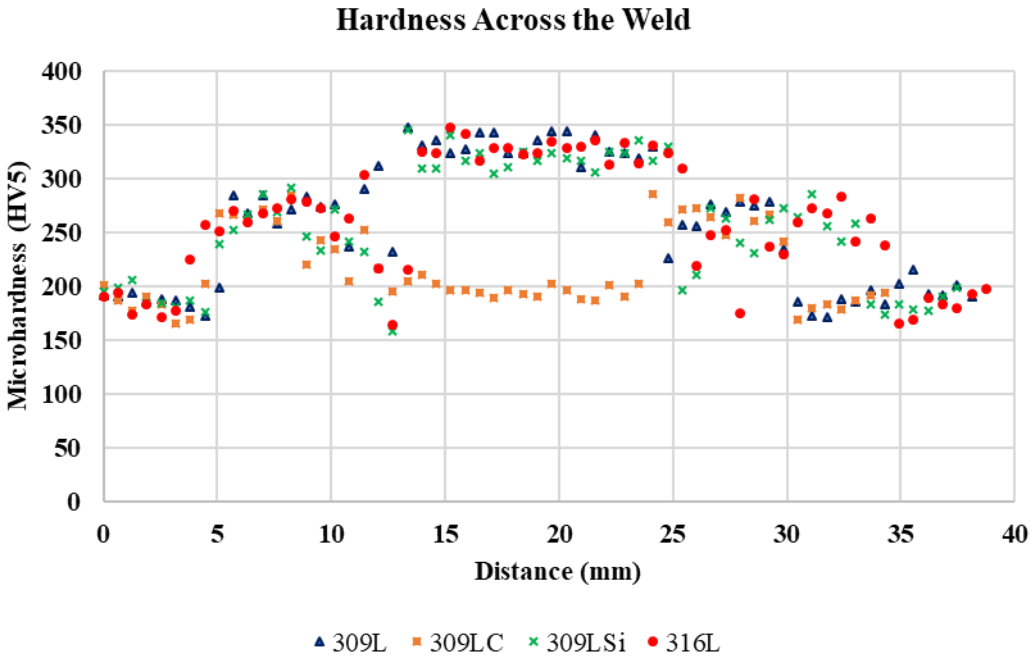

Figure 3.11. *Typical hardness trends found in across the second weld pass using the different fillers, 75 kJ/in, and 450 °F in the Group 1 plates. The fusion zone hardness values of the solid wires (309L, 309LSi, and 316L) are consistent despite the differences in composition, while the 309LC has a lower hardness in the fusion zone and is comparable to that of the base material.*

3.3.5 Uniaxial Tension Testing

In order to explore the change in the mechanical properties of the welded plate as the heat input and/or the maximum interpass temperature was increased, tensile testing was performed on each of the Group 1 and 2 plates. Because 50CR is not yet included in AASHTO/AWS D1.5, there are no tensile requirements for welded 50CR, so the data was compared to 50CR base metal requirement set forth by ASTM A709.[37] Ten reduced section tension samples were tested from each of the plates welded using the 309L and 309LC filler wires, and five samples were tested from each of the plates welded using 309LSi and 316L for Group 1. Three samples were tested for each of the Group 2 plates.

Based on the results from one-sided t-testing of data obtained from mechanical testing of 1/2" welded plates in Group 1, it can be said with at least 95% confidence that a sample selected at random from any of the welding combinations explored will surpass the minimum yield strength requirement of 50 ksi dictated by ASTM A709 for grade 50CR,[37] regardless of which filler wire, heat input (50 kJ/in and 75 kJ/in), and maximum interpass temperature (125 °F to 450 °F) were employed. Based on two-sided t-testing, it can also be said with 95% confidence that neither increasing the heat input nor increasing the maximum interpass temperature caused a statistically significant change to the yield strength for all consumables, even though different numbers of welding passes were used to weld the plates with a heat input of 75 kJ/in and a maximum interpass temperature of 300 °F.

Using the same statistical analysis procedure as was used for the yield strength data, it can be said with at least 95% confidence that a 1/2" welded plate sample selected at random will meet the 70 ksi tensile strength minimum requirement set forth by ASTM A709,[37] regardless of the consumable weld wire employed. It can also be stated with at least 95% confidence that neither increasing the heat input, nor increasing the maximum interpass temperature caused a statistically significant change in the tensile strength.

ASTM A709, which is currently used as the standard to which welded 50CR's mechanical properties are compared, contains minimum requirements for yield strength, tensile strength, and percent elongation.[37] According to ASTM A370, percent elongation can only be accurately reported if the fracture occurs in the middle 50% of the gage length.[67] However, in this study, the fracture typically occurred outside of this region, with only 14% of all of the welded samples fracturing within the reportable region. This is due to the fact that the strain

localized in the unaffected 50CR based material observed by the formation of the neck, where the delamination cracking and fracture ultimately occurred.

Tensile test data from the 1" thick Group 2 plates was also compared to the minimum requirements dictated by ASTM A709.[37] The average values from the three tensile tests all met the minimum requirements for both the yield strength and the tensile strength. The lower level of confidence level (< 90%) associated with the yield strength of the Group 2 samples is most likely due to the smaller number of samples tested. One-sided t-tests of the tensile strength data showed with at least 95% confidence that a sample selected at random from all of the welding parameter combinations will meet the 70 ksi required minimum.[37] Tensile testing on the two Group 3 welded PQR plates included both two reduced section tensile samples and one all weld metal tensile bar. The data from the testing is listed in Table 3.10 below. The tensile strengths for the reduced section samples exceed the minimum tensile strength requirement of 70 ksi and the yield strength exceeded the minimum requirement of 50 ksi.[37] The tensile testing data from the two PQR plates showed comparable results when compared to the data from analogous plates from Group 2. One interesting distinction between the internally and externally tested tensile samples is the location of the failure. The Group 1 and Group 2 failures both showed the appearance of delamination cracking in the base material and ultimately failed there. However, the Group 3 reduced section tensile samples failed either in the weld or in the HAZ.

Table 3.10. *Results from testing of Group 3 plates welded using 309L and 309LC with a heat input of 90 kJ/in and a maximum interpass temperature of 450 °F.*

Sample Type	Yield Strength (ksi)	Tensile Strength (ksi)	% Elongation (%)	Reduction in Area (%)
309L reduced section	(56, 63)	89, 90	23, 26	25, 25
309L all weld	54	88	30	27
309LC reduced section	(61, 55)	95, 92	42, 32	36, 33
309LC all weld	58	94	36	46

3.3.6 Charpy V-Notch Impact Testing

AASHTO/AWS D1.5 indicates the average of five samples with the highest and lowest test values thrown out should be reported or to simply test three samples and average those values.[61] For non-fracture critical members, the specified testing temperature for AASHTO zones 1 and 2 is 0 °F and -20 °F for zone 3.[61] For fracture critical components, the testing is to be performed at -20 °F, regardless of zone.[61] In both cases, the minimum CVN value is 20 ft·lbf. Testing was performed at -20 °F to make it relevant to all three AASHTO zones as well as fracture critical components and increase the applicability of the data.

Table 3.11. *Average impact energies of the Group 1 full-size CVN samples. The asterisk indicates the failure to meet both the fracture critical and non-fracture critical minimum impact energy requirements of the AASHTO/AWS D1.5*

Filler Wire	Heat Input (kJ/in)	Maximum Interpass Temp. (°F)	CVN All 5 Samples (ft·lbf)	AASHTO/AWS D1.5 CVN (ft·lbf)
309L	50	300	53	53
309L	75	125	21	20
309L	75	300	38	39
309L	75	450	17*	17*
309L Retest	75	450	22	21
309LC	50	300	57	57
309LC	75	125	40	39
309LC	75	450	41	41
309LC Retest	75	450	39	36
309LSi	75	125	26	26
309LSi	75	450	20	20
316L	75	125	24	24
316L	75	450	25	25

The data obtained from the Group 1 plate is shown in Table 3.11. Most all of the tested conditions would pass the minimum standard for non-fracture critical components. However, it can be seen that the first set of five samples welded using 309L filler, at a heat input of 75 kJ/in and a maximum interpass temperature of 450 °F, failed to pass the standard. A second set of five samples passed, indicating that this condition is a borderline case. Two-sided t-tests indicate with

95% confidence that increasing the maximum interpass temperature did not have a significant effect on the CVN values, in comparison to the heat input. Increasing the heat input from 50 to 75 kJ/in resulted in a 29% decrease in CVN impact energy (from an average of 53 to 38 ft·lbf) when 309L filler wire was implemented.

The CVN impact energies for Group 2 plate samples are presented in Table 3.12. They all greatly exceeded the AASHTO/AWS D1.5 minimum requirement for both fracture and non-fracture critical components.[61] One-sided t-testing of the tensile strength data showed with at least 95% confidence that a sample selected at random from all of the welding parameter combinations will exceed the requirement.

Table 3.12. *Average impact energies of the Group 2 full-size CVN samples*

Filler Wire	Heat Input (kJ/in)	Maximum Interpass Temp. (°F)	CVN All 5 Samples (ft·lbf)	AASHTO/AWS D1.5 CVN (ft·lbf)
309L	70	300	72	74
309L	90	300	66	65
309L	90	450	50	50
309LC	70	300	74	74
309LC	90	300	71	71
309LC	90	450	71	71
309LSi	70	300	78	78
309LSi	90	300	73	74
309LSi	90	450	74	75
316L	70	300	43	43
316L	90	300	52	49
316L	90	450	65	69

One set of five CVN samples, with the notch placed in the weld, were tested for each Group 3 plate. Each plate yielding higher impact energies than the analogous Group 1 samples, but comparable to those from Group 2, as shown in Table 3.13. In the Group 1 plate, full-sized CVN samples were taken from the middle 3/8” (10 mm) of the 1/2” thick plate. For the Group 2

and 3 plates, full-size CVN plates were also taken from the middle 3/8" (10 mm) of the plate, keeping in mind that there are more weld passes used when welding these plates.

Table 3.13. *Summary of impact energies of PQR full-size weld samples*

Filler Wire	Heat Input (kJ/in)	Maximum Interpass Temperature (°F)	CVN All 5 Samples (ft·lbf)	AASHTO/AWS D1.5 CVN (ft·lbf)
309L	90	450	90	89
309LC	90	450	93	93

Previous research on duplex stainless steels (50-50 vol% ferrite and austenite) reports a three-regime transition temperature curve, similar to that of purely ferritic steels.[46] The temperature transition curves of the four filler wires welded using a heat input of 75 kJ/in and a maximum interpass temperature of 450 °F on the Group 1 plates, deemed the most aggressive welding parameter combination, are shown in Figure 3.12.

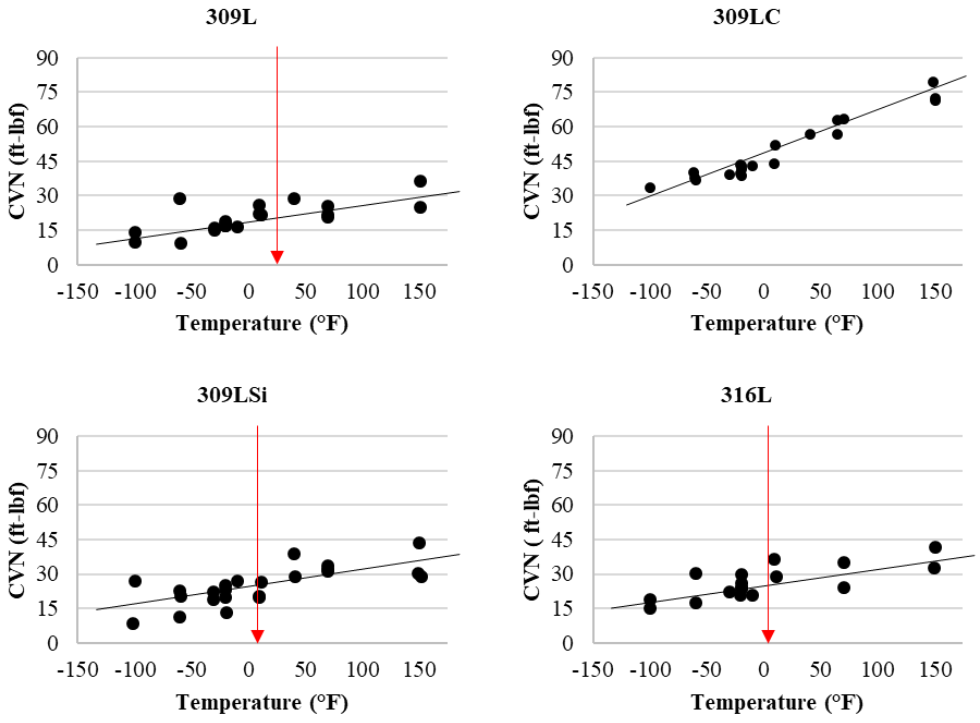

Figure 3.12. *CVN data for the 1/2" welded (Group 1) plates using a heat input of 75 kJ/in and a maximum interpass temperature of 450 °F for the entire range of service temperatures. The red arrow indicates the fracture appearance transition temperature (FATT), determined based on visual inspection, as described in more detail in the Fractography section below.*

Based on the results, the three-regime transition curve was abandoned in favor of linear fitting which is more consistent with a microstructure predominantly containing austenite.[68] The impact energies for the plates welded using 309LC were consistently higher in comparison to those welded with the three solid filler wires. Based on the fitted transition temperature curve, 50CR welded using 309LC will not fall below the 20 ft·lbf minimum until well below -100 °F, significantly lower than any minimum service temperature.[61,76] The DBTT of the other filler wires (309L, 309LSi, 316L) is estimated to be in the range of 0 - 25°F, based upon the fracture appearance transition temperature (FATT), described in detail in the Fractography section below.

3.3.7 Side Bend Testing

The four bend tests performed on each PQR plate were acceptable.[61] No cracks were seen in the weld or at the fusion line (as previously shown by Grobler) when a full 180° bend was placed on the bend test sample. Figure 3.13 presents images of a typical side bend test sample. The lines that appear in Figure 3.13b were shown to be raised regions as they were not seen in OM after light sanding with 600 grit paper.

a) b)

Figure 3.13. a) *Side view and* ***b)*** *top view of the side bend samples with the weld placed in the middle.*

3.3.8 Fractography

Although both of the Group 3 reduced section samples failed either in the weld or in the HAZ, the fracture surfaces differ between the sample that was welded using 309L and the one welded using 309LC, as can be seen in Figure 3.14. Analysis of the fracture surface for the 309L

sample indicates a mixture of intergranular and transgranular brittle fracture, shown in Figure 3.15. Intergranular brittle fracture is typically characterized by a very smooth and faceted fracture surface, while transgranular cleavage will typically show cleavage lines, as seen here. The regions of intergranular brittle fracture are not highly faceted in this cause due to the elongated nature of the prior δ grains.

Figure 3.14. *Group 3 reduced section tension sample fracture surface welded using* ***a)*** *309L and* ***b)*** *309LC. The 309L sample appears to contain a mixture of ductile and brittle fracture modes, while the 309LC sample only contains ductile.*

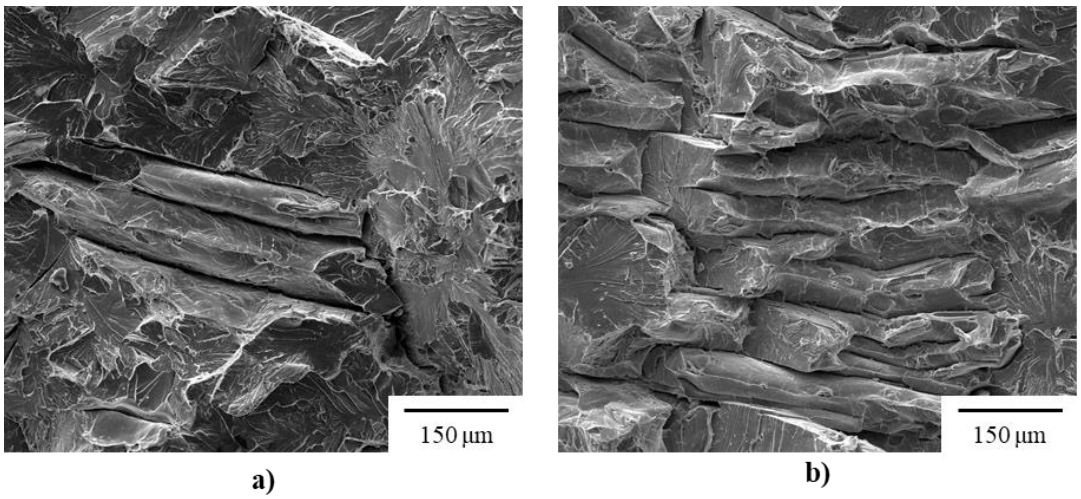

Figure 3.15. *Group 3 reduced section tension sample fracture surface welded using 309L with both intergranular (the long smooth rod-like fractures) and transgranular brittle fracture displayed.*

One method for the characterization of CVN fracture surfaces is visual inspection and optical microscopy. Ductile fractures appear dull whereas brittle fractures (both intergranular and intragranular) will generally have a more granular appearance, which will more readily reflect light and appear shiny.[68,70,84] Figure 3.16 shows the fracture surface appearance of welds made using all four filler wires at a heat input of 75 kJ/in and a maximum interpass temperature of 450 °F. Each row of figures corresponds to CVN tests performed at -100, -20 and 150 °F, from left to right. The first observation to be made is that all of the fracture surfaces of the 309LC samples are ductile. Secondly, one can observe details about the appearance of the brittle fractures in the welds made using the other three (solid) filler wires. It is important to note that for the remaining tested samples tested at -20 °F (the Group 1 samples that were welded with a maximum interpass temperature of 300 °F and all of the Group 2 and 3 samples), the fracture surfaces were considered to be 100% ductile.

Because the transition temperature curves of the welds do not exhibit the typical three-zone lower-shelf, upper-shelf, and transition regions, it was desirable to develop another means of establishing the DBTT. Therefore, the 50% ductile-50% brittle fracture appearance transition temperature (FATT) was determined by optical microscopy. The degree of ductile vs. brittle fracture surface appearance was quantified and the results were analyzed using linear regression to determine the best-fit temperature (FATT) at which the 50:50 transition occurred, as indicated by arrows in Figure 3.17. These are the DBTT values, which are also indicated with arrows in Figure 3.12.

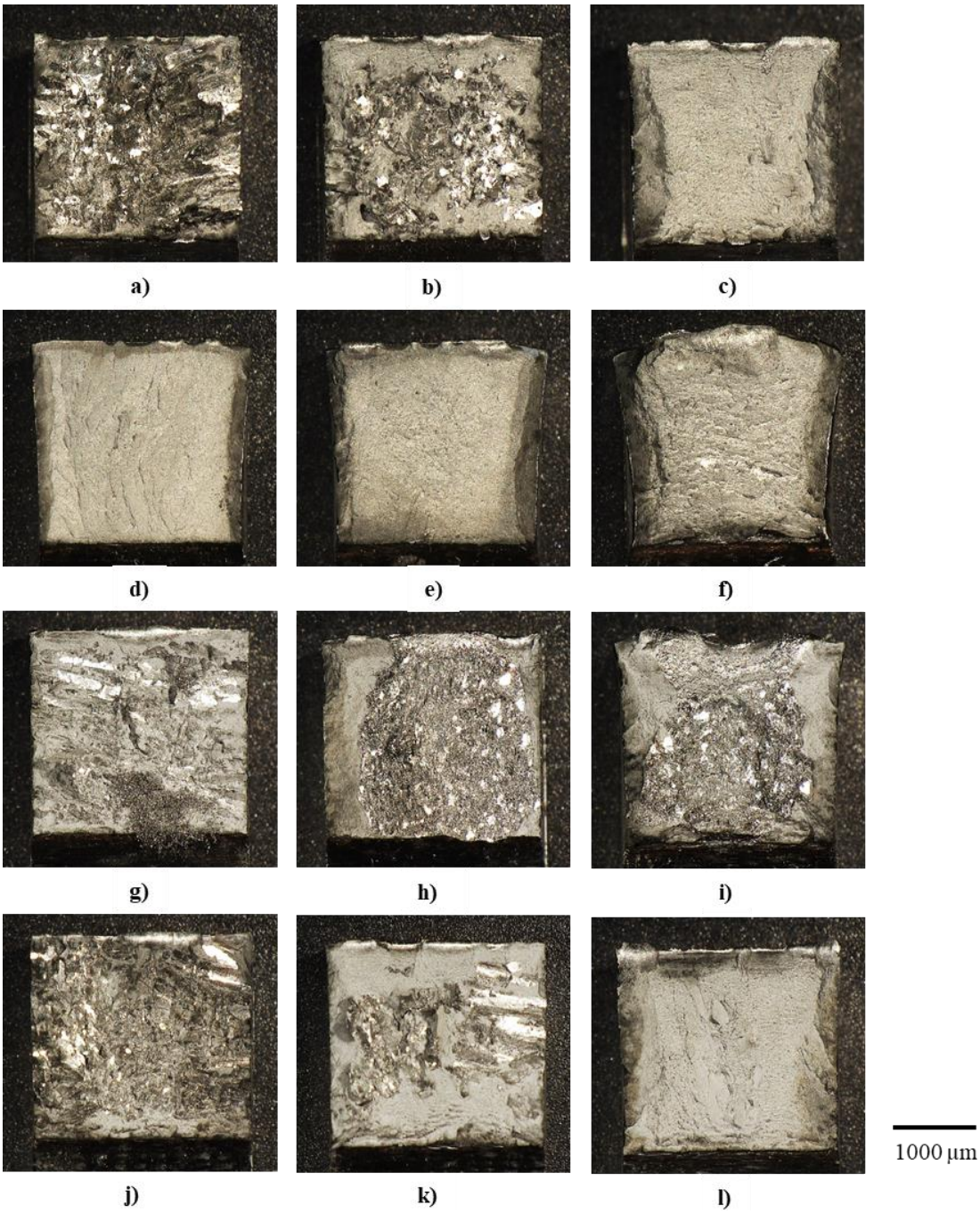

Figure 3.16. *Optical micrographs of the CVN fracture surfaces taken at 20X magnification of the Group 1 samples welded using a heat input of 75 kJ/in and a maximum interpass temperature of 450 °F. Each row of figures corresponds to tests performed at -100 °F (a, d, g, j), -20 °F (b, e, h, k), and 150 °F (c, f, i, l) on welds made using 309L (a, b, c), 309LC (d, e, f), 309LSi (g, h, i), and 316L (j, k, l), respectively.*

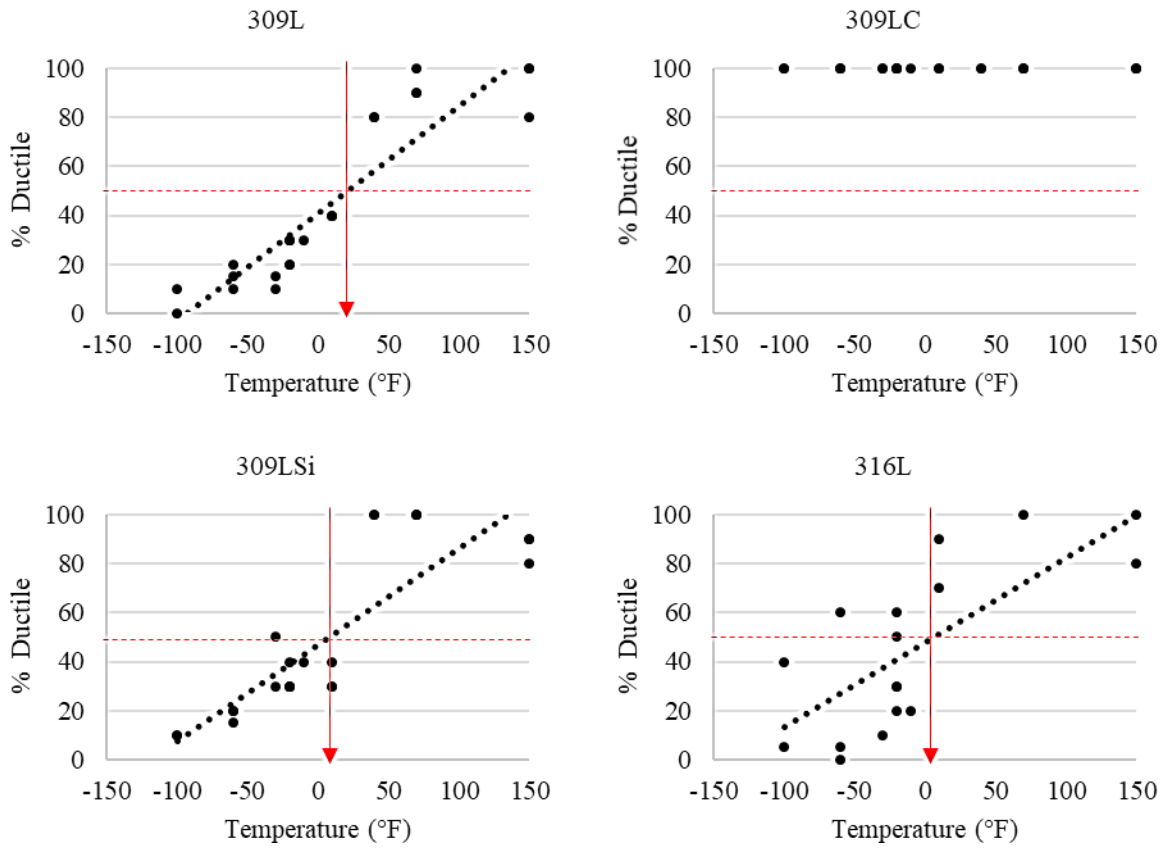

Figure 3.17. *Based on optical micrographs of the CVN fracture surfaces taken at 20X magnification of the Group 1 samples welded using a heat input of 75 kJ/in and a maximum interpass temperature of 450 °F.*

Analysis with the SEM indicated that the CVN brittle fractures occurred most commonly by transgranular cleavage as opposed by intergranular, as shown in Figure 3.18. This is indicated by the cleavage lines, especially visible in Figure 3.18b.

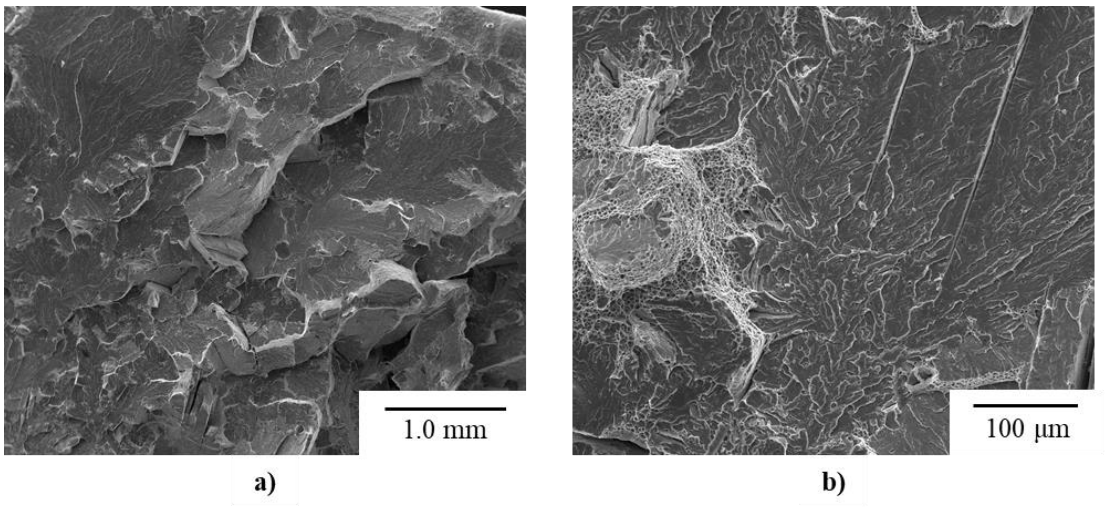

Figure 3.18. *SEM micrographs of solid wire CVN weld brittle fractures showing indications of transgranular cleavage as opposed to intergranular fracture.*

3.4. Discussion

3.4.1. Microstructure

The metal cored wire consistently resulted in fusion zones with less dilution from the base material. This indicates that 1) the composition of the fusion zone using 309LC was closer to the original filler wire composition and 2) the metal cored overall delivered slightly less heat to the base material during welding. According to literature, for the same welding inputs, metal cored wire is more likely to transfer the molten metal by a spray mechanism as opposed to globules, assuming free flight transfer occurs.[49] Assuming that this difference in metal type transfer occurred in this study, the spray type droplets are more likely to experience cooling during the metal transfer due to the significantly smaller size, and would thus deliver a slightly lower overall heat to melt the base material, resulting in the lower dilution.[42]

Based on the Schaeffler constitution diagram prediction, the expected phases in the fusion zone was a mixture of austenite, ferrite, and martensite. However, no martensite was seen the conventional metallography. This could be accounted by the relatively slow cooling rates experienced by the welds.

From the Rosenthal thin plate calculations in Section 3.3.2, it is clear that the cooling rate for the Group 2 plates was significantly faster than that of the Group 1 plates. This led to a higher residual δ-ferrite content, seen in the metallographic analysis. This trend implies that even thicker plate will experience faster cooling rates for the same heat input. However, due to the potential loss of mechanical strength and impact energy as the amount of residual δ-ferrite increases (to more than 50 vol%), further testing must be performed to establish a desired $\Delta t_{8\text{-}5}$ range.

3.4.2. Effect of Microstructure on Mechanical Properties

The microstructural analysis revealed that 309LC consistently presented with a higher residual δ ferrite content. This is again likely related to the literature suggested difference in molten metal transfer type between the solid and metal cored wires.[49] Due to the spray type transfer, the overall heat transferred to the weld plate was slightly lower, resulting in a slightly faster cooling rate, allowing for less time for the solidified δ ferrite to solid state transform into austenite, even though all of the fusion zones solidified through the F pathway. This difference in transfer type could also explain the difference seen in the size of the prior δ grain size. Due to a smaller molten particle size being transferred, the heat would dissipate faster to the surrounding base material and therefore act as an initiation site for solidification and growth. This difference in the type of metal transfer is also likely the cause of the difference in the fusion zone hardness, shown in Section 3.3.4. Due to the faster cooling rate associated with 309LC welds, the fusion zone would be unable to precipitate in a significant way, while the slow cooling rate of the three solid wires would allow for the weld to remain the temperature range optimal for precipitation and/or ferrite decomposition for a longer period of time. The precipitates that may have formed include the sigma, chi, and G phases.[16,43,48,66] In fact, the G phase typically is seen on the nano-scale,[105,106] and is likely why it was not observed during the fusion zone characterization. The

formation of nano-scale precipitates in the fusion zone of the solid wire welds could account for the over 100 HV difference in the micro-hardness.

The results of the present study agree with previous testing of welded 50CR plates performed by Oregon on the performance of 309L filler wires. For a heat input of 54 kJ/in used in combination with a maximum interpass temperature of 225°F, 300 °F, 400 °F, or 450 °F, it was found that the samples from the plates were able to surpass the requirements set forth by AASHTO/AWS D1.5.[72] However, there was not any comparable data in literature available on 309LC, 309LSi, and 316L. Again, the range of retained ferrite observed in this study is considered to be in the safe range, where no correlation between ferrite content and ductility has been observed. Only at very low < 2 vol% is there a correlation with hot cracking[63] and at very high > 50 vol% is there a correlation with low temperature embrittlement.[65] Bend testing was also consistent with available literature on bend testing of the legacy alloy, 3CR12, where cracking within the coarse-grained HT-HAZ was only observed when welding with 3CR12 filler wire and not when using austenitic filler wires such as the 309L and 316L type filler wires employed in the present study.[9]

That said, the subtle difference in the microstructure between the plates welded using the solid and metal core wires correlated with the ductile to brittle transition temperature (DBTT) of the resulting welds. Note the large, bright regions, which are present in the fracture surfaces of the CVN samples tested at low temperatures, especially in Figures 3.14 (a, d, g, h) that correspond to the large prior δ-ferrite grains which extend parallel to thickness in Figure 3.8 (a, b, d). The use of 309LC metal core filler wire results in the refinement of the δ-ferrite grains during solidification as well as the Widmanstätten structure adopted by the austenite within those grains during cooling (Figure 3.9). Thus, as alluded to in the Chapter 1, it is hypothesized that

even though the ferrite content of the weld comprised of 309LC filler metal is higher than the others (Table 3.8), the distribution/morphology of that retained ferrite is not detrimental to the toughness. Indeed, the refined microstructure appears to be beneficial, in spite of the higher ferrite content.

This claim is supported by the Cr_{eq}/Ni_{eq} values when compared to the crack length vs Cr_{eq}/Ni_{eq} plot obtained from Mateša et al. The crack length is minimized between a value of 1.5 and 2. The metal cored wire had the lowest Cr_{eq}/Ni_{eq} value of all of the Group 1 samples. The samples that had more than simple two passes also showed a lower Cr_{eq}/Ni_{eq} than their two weld pass counterparts. Thus, not only did the multiple passes aid in the disruption for forming long columnar grains that would span the location of the V notch, but they also aided in the formation of a slightly less crack prone microstructure.

3.4.3 Mechanical Properties of the Group 1 Plate with an Incomplete Weld

During tensile testing, it was discovered that the samples from the plate welded using 309LC, a heat input of 75 kJ/in, and a maximum interpass temperature of 300 °F contained a lack of fusion defect, a gap of roughly 0.0787" (2 mm) in size, which was visible during radiography. Communications with the girder fabricator indicated that the weld gap arose from improper weld groove alignment and not from difficulty welding with the metal cored wire. Nevertheless, mechanical testing of the plate was performed as if there was no mechanical flaw.

The samples from the plate with a 2 mm gap (309LC, 75 kJ/in, 300 °F) resulted in an average yield strength of 55.2 ksi with a standard deviation of 0.76 ksi. This means that the plate would have met the ASTM A709 requirements.[37] The one-sided t-test also showed with 99% confidence that a sample chosen at random from the defective plate would have been able to meet the minimum requirements. Because the yield strength is the amount of stress a sample can

undergo before yielding and beginning to plastically deform, a gap of this size is shown to be tolerable. This is helpful information to guide non-destructive evaluation requirements.

The samples from the plate with the incomplete weld (309LC, 75 kJ/in, 300 °F) yielded an average tensile strength of 69.9 ksi with a standard deviation of 3.42 ksi. This means that the plate would have met the ASTM A709 requirements, due to rounding. However, it fails the one-sided T-test for 90% confidence. This is due to the existence of the 2 mm gap, which acted like a pre-existing crack, resulting in a lower tensile strength.

The CVN impact energies for the plate with the incomplete weld is given below in Table 3.14. Although there was a 0.0787" (2mm) gap, the machining of the V-notch eliminated a majority of the welding defect. However, some of the welding gap still remained, which caused a decrease in the impact energy because the sample was already pre-cracked. The remaining weld gap simply continued to split, eliminating the need for a crack path to develop.

Table 3.14. *CVN impact energy for the defective plate*

Filler Wire	Heat Input (kJ/in)	Maximum Interpass Temp. (°F)	CVN All 5 Samples (ft·lbf)	AASHTO/AWS D1.5 CVN (ft·lbf)
309LC	75	300	22	22
309LC Retest	75	300	24	24

Overall, the mechanical testing of the defective plate would have passed according to the AASHTO/AWS D1.5 requirements. This is further indication of the advantages that come with using 309LC filler wire. Welds made with 309LC may be more tolerant of flaws, though no testing was performed on equivalently flawed welds made with solid filler wires. These results could also indicate that the non-destructive evaluation requirements for the welding of 50CR using 309LC filler wire could be relaxed. However, further testing of welded plate with planned defects must be performed before a firm conclusion on this point could be made.

Chapter 4: Conclusions and Future Work

4.1 Conclusions

1. The following filler wires: 309LC, 309LSi, and 316L can be used as alternatives to 309L for the welding of ASTM A709 Grade 50CR. Note that 309LC metal cored wire requires a higher feed rate (up to ~ 50%), but other welding parameters (voltage, current, and travel speed) can remain the same.

2. 309LC filler wire can be used to weld 1/2" plates with heat inputs of up to 75 kJ/in and all interpass temperatures explored up to 450 °F. Such welds exceed all mechanical property requirements.

3. The use of 309L filler wires for welding 1/2" plates results in welds leads to impact energies that are borderline with respect to AASHTO/AWS D1.5 requirements at a heat input of 75 kJ/in over the interpass temperature range investigated (125 – 450 °F). The ability for the plate welded with a maximum interpass temperature of 300 °F to surpass the requirements is due to the use of an abnormal number of weld passes. The properties of the welds produced with a heat input of 50 kJ/in far exceed all of the mechanical property requirements.

4. The use of 309LSi and 316L filler wires for 1/2" plates pass the toughness requirement for non-fracture critical components at a heat input of 75 kJ/in, but fail to meet the toughness requirement for fracture critical components at all interpass temperatures explored (125 and 450 °F).

5. The enhanced toughness of welds in 1/2" plates formed using 309LC filler wire appear to be due to the mitigation of large, aligned δ-ferrite grain formation during solidification especially in the middle of the weld. In fact, 309LC neither showed a DBTT nor a fracture appearance transition temperature (FATT), and remained ductile down to -100 °F. The large and aligned grains of the welds produced by the solid wire serve as preferred crack paths, leading to the observation of brittle nature. This occurred despite the higher volume fraction of delta ferrite in the metal cored wire weld.

6. The absence of brittle nature on the second batch of Group 1 and the Group 2 samples was due to the presence of multiple weld passes, which led to an angular variation that prevented the easy crack path present in the weld plates welded with solid wire in the first batch of Group 1.

7. Heat inputs of 90 kJ/in and interpass temperatures of up to 450 °F can be used for 309L, 309LC, 309LSi, and 316L filler wires for 1" thick plate. The thicker plates are more tolerant of high heat inputs because they represent a larger heat reservoir outside the fusion zone itself. This was shown by the Rosenthal calculations in which the 1" plates have a shorter $\Delta t_{8\text{-}5}$ for the same heat input value.

8. The delamination cracking of 50CR occurred due to the presence of elongated grains and intermetallic precipitates as well as the necessary combination of mechanical properties that allowed for the formation of a neck with high enough triaxiality to develop a sufficient through-thickness stress. The presence of elongated grains, common to the rolled plate, led to an easy crack path with minimal undulation, as seen in the micrographs in this study. These Al based stringers replace the titanium carbo-nitrides found to be responsible in 3CR12. The strain hardening exponent was found to be 0.092 in both the L and T orientations. This low strain hardening exponent led to the onset of plastic instability at a relatively low strain, but the non-negligible strain rate sensitivity allowed for the stabilization of the neck and the delay of catastrophic instability, leading to the post-uniform elongation seen. This delay allowed for the formation of a neck with a reduction in area of ~80%, leading to the sufficient through-thickness stress for delamination to occur. The ratio of the true strain in the width direction to the true strain in the thickness direction was found to be less than one both in the uniformly straining regime as well as in the region where strain localization occurred, i.e. the neck. This further aided in the development of the necessary triaxiality by causing the material to strain faster in the through-thickness direction of the tensile specimen, allowing the necessary stress to develop at an overall lower strain.

4.2 Future Work

Based on the results of this study, it was shown that the 50CR plates welded with the metal cored wire showed a smaller prior-δ ferrite grain size and more refined Widmanstätten austenite. It is hypothesized that the difference in the molten metal transfer mode (spray vs globular) revealed in previous studies causes the observed difference in solidification structure.[49,50,107–110] However, the transfer mode has not been shown for this set of welding inputs (amperage, travel speed, voltage, bias, etc.). The difference in transfer modes will likely lead to an overall different temperature gradient in the resulting melt pools. The globular transfer will likely lead to a Gaussian distribution, with the highest temperatures in the center of the weld pool, while the spray type transfer will likely show more variations. A high-speed thermal camera would be required for this study. One hinderance to the high-speed observation of the metal transfer and verification of the literature is the welding method used in this study. Because the filler wire and the resulting metal transfer occurs under a flux powder bed, it would be difficult to optimize a set up to perform this experiment.

In order to meet the goal of erecting maintenance-free 50CR bridges, this study showed that the mechanical properties of the weld joints using the newly proposed welding parameters are able to surpass the minimum requirements. However, the question of long-term corrosion resistance of the resulting welds is still unresolved. The predecessor alloy for 50CR, 3CR12, had a prescribed amount of Ti added to the alloy composition to render the material “stabilized” relative to sensitization to grain boundary corrosion and cracking phenomena. The Ti would bind excess C in the alloy preferentially and thereby prevent the formation of unwanted chromium carbide on grain boundaries. However, detailed study showed that this well-intentioned alloy design strategy was not effective for certain cases, and therefore, the requirement for Ti stabilization is not included in the specification of 50CR.[35,111–113]

Sensitization in an austenitic weld can be tested for initially by using the 10 vol% oxalic etch test as indicated by ASTM A262 Practice A. For a sensitized material, the etchant will reveal "ditch" structures along the grain boundaries which indicate the possible presence of chromium carbides. However, Practice A can only identify suspicious microstructures and required other testing to prove or disprove the occurrence of sensitization.[114] Another test that can be used is the modified Strauss Test indicated by ASTM A763 Practice Z. This utilizes a bend test to reveal the embrittlement of the weld and HAZ due to chromium carbide formation that causes Cr depletion near the grain boundaries. The cracks and fissures that form are indicative of intergranular attack.[112,113]

In the case of welded 50CR, modes 2 and 4 of sensitization are most likely to occur in the HAZs of the welds, while sensitization of the austenitic fusion zone is also probable. Mode 2 is more likely to appear in the second batch of the Group 1 plates as well as the Group 2 and 3 plates due to the high number of passes used. This would increase the probability that HAZs of two adjacent passes overlapped in order to cause sensitization. Mode 4 is most likely to occur in the 1/2" plates welded using 75 kJ/in due to the slow cooling rate experienced, shown by the Rosenthal $\Delta t_{8\text{-}5}$ calculation. Reduced section tensile testing of the Group 3 plates indicated fractures that occurred within the welds. Fractography of the 309L showed indications of intergranular brittle fracture, which could be due to of sensitization. Thus, further research must be performed to determine whether or not the proposed welding parameters caused sensitization to occur. If sensitization occurred, then intergranular corrosion can occur, which may lead to stress corrosion cracking. This would ultimately undermine the longevity and maintenance-free nature of 50CR bridges.

Chapter 5: References

1. Fletcher, F. B. *Improved Corrosion-Resistant Steel for Highway Bridge Construction*. *Publication No. FHWA-HRT-11-062* (2011).
2. Ball, A. & Hoffman, J. . Microstructure and Properties of a Steel Containing 12% Chromium. *Met. Technol.* **8**, 329–338 (1981).
3. Matthews, L. M. & DeMarsh, E. A. *The Response of As Rolled 3CR12 Steel to Heat Treatment*. (1985).
4. Knutsen, R. D. A Microstructural Examination of Duplex Ferrite-Martensite Corrosion Resisting Steels. (University of Cape Town, 1989).
5. Okasha, N. M., Frangopol, D. M., Fletcher, F. B. & Wilson, A. D. Life-Cycle Cost Analyses of a New Steel of Bridges. *J. Bridg. Eng.* **17**, 168–172 (2012).
6. Soliman, M. & Frangopol, D. M. Life-Cycle Cost Evaluation of Conventional and Corrosion-Resistant Steel for Bridges. *J. Bridg. Eng.* **20**, (2015).
7. Balmforth, M. . & Lippold, J. C. A Preliminary Ferritic-Martensitic Stainless Steel Constitution Diagram. *Weld. J. Suppl.* 1-s-7-s (1998).
8. Thomas, C. R. Structure and Properties of a Duplex Ferritic-Martensitic Stainless Steel. in *Duplex Stainless Steels* (ed. Lula, R. A.) 649–664 (American Society for Metals, 1983).
9. Grobler, C. Weldability Studies on 12 % and 14 % Chromium Steels. (University of Pretoria, 1987).
10. Jana, S. Effect of Heat Input on the HAZ Properties of Two Duplex Stainless Steels. *J. Mater. Process. Technol.* **33**, 247–261 (1992).
11. Hoffman, J. . The Welding Metallurgy of a Titanium Stabilized 12 Percent Chromium Ferritic-Martensitic Steel. in *International Conference on New Developments in Stainless Steel Technology* (ed. Lula, R. A.) 305–218 (American Society for Metals, 1985).
12. Taban, E., Deleu, E., Dhooge, A. & Kaluc, E. Laser Welding of Modified 12% Cr Stainless Steel: Strength, Fatigue, Toughness, Microstructure and Corrosion Properties. *Mater. Des.* **30**, 1193–1200 (2009).
13. Bennett, P. The Weldability of 12 Percent Chromium Ferritic Corrosion Resisting Steels. *Mater. Australas.* **23**, 15–16 (1991).
14. Venkatesan, M. V., Murugan, N., Sam, S. & Albert, S. K. Effect of Heat Input on Macro, Micro and Tensile Properties of Flux Cored Arc Welded Ferritic Stainless Steel Joints. *Trans. Indian Inst. Met.* **67**, 375–383 (2014).
15. Whitefield, D. J. & Van Bennekom, A. Abrasive Wear Properties of Experimental Metastable Duplex Stainless Steels. *Wear* **196**, 92–99 (1996).
16. Mathers, G. Welding of Austenitic Stainless Steel. https://www.twi-global.com/technical-knowledge/job-knowledge/welding-of-austenitic-stainless-steel-103.

17. Schade, C., Lawley, A. & Wagner, E. Development of a High-Strength-Dual-Phase P/M Stainless Steel. https://www.researchgate.net/publication/239541756_DEVELOPMENT_OF_A_HIGH-STRENGTH-DUAL-PHASE_PM_STAINLESS_STEEL/citation/download (2005) doi:10.1017/CBO9781107415324.004.

18. ArcelorMittal. Duracorr: Life-Cycle Cost-Effective 12% Chromium Stainless Steel. vol. 35 1–5 https://usa.arcelormittal.com/.../steel-products/plate-products/Duracorr-lifecycle.pdf (2014).

19. Lombaard, J. 3CR12 in Water Applications. in *13th International Corrosion Congress Proceedings* (ed. Clayton, V.) 1–10 (Australasian Corrosion Association, 1996).

20. Ulvan, E. & Koursaris, A. The Effect of Hot Rolling and Annealing on the Cold Bulk Formability of Steel Types 3CR12 and 304. *Journal of Materials Shaping Technology* vol. 6 251–260 (1989).

21. Atlas Steels. ATLASCR12 and ATLASCR12TI: The 12% Chromium Ferritic Stainless Steels. www.atlassteels.com.au/documents/TN13-CR12_steels_rev_July_2012.pdf (2012).

22. Knutsen, R. D. Effect of Non-Metallic Inclusions on the Fracture of 3CR12 Corrosion Resistant Steel. in *Electron Microscopy Society of Southern Africa Proceedings* 37–38 (Electron Microscopy Society of Southern Africa, 1985).

23. Knutsen, R. D. Microstructural Investigation of Austenite Decomposition in 3CR12 Steel. in *Electron Microscopy Society of Southern Africa 31st Annual Conference Papers* vol. 22 155–156 (1992).

24. Balmforth, M. . & Lippold, J. C. A New Ferritic-Martensitic Stainless Steel Constitution Diagram. *Weld. J. Suppl.* 339-s-345-s (2000).

25. Kotecki, D. & Armao, F. Stainless Steel Welding Guide. *The Lincoln Electric Company* https://www.lincolnelectric.com/assets/US/EN/literature/c64000.pdf (2014).

26. Mateša, B., Samardžić, I. & Dunder, M. The Influence of the Heat Treatment on Delta Ferrite Transformation in Austenitic Stainless Steel Welds. *Metalurgija* **51**, 229–232 (2012).

27. Lundin, C. D., Ruprecht, W. & Zhou, G. *Ferrite Measurement in Austenitic and Duplex Stainless Steel Castings*. (1999).

28. Niagaj, J. & Mazur, Ł. Review of Methods for Measurement of Ferrite Content in High Alloyed Steels and Their Welded Joints. *Weld. Int.* **28**, 345–353 (2014).

29. Schaeffler, A. L. Constitution Diagram for Stainless Steel Weld Metal. *Met. Prog.* **56**, 680-680B (1949).

30. DeLong, W. T., Ostrom, G. A. & Szumachowski, E. R. Measurement and Calculation of Ferrite in Stainless Steel Weld Metal. *Weld. J. Suppl.* **35**, 521-s-528-s (1956).

31. Koskiniemi, J. A., Karjalainen, L. P., Pistorius, P. G. H. & Van Rooyen, G. T. Effects of Chemical Composition and Thermomechanical Treatment on Austenite to Ferrite

Transformation in 12 wt-%Cr Steels. *Mater. Sci. Technol.* **14**, 1115–1121 (1998).

32. Ball, A., Chauhan, Y. & Schaffer, G. B. Microstructure, Phase Equilibria, and Transformations in Corrosion Resistant Dual Phase Steel Designated 3CR12. *Mater. Sci. Technol.* **3**, 189–196 (1987).

33. Thomas, C. R. & Hoffman, J. . Metallurgy of a 12% Chromium Steel. in *Proceedings of the International Conference on Recent Developments in Specialty Steels and Hard Materials (Materials Development '82)* (eds. Comins, N. R. & Clark, J. B.) 299–306 (Pergamon, 1983). doi:10.1017/CBO9781107415324.004.

34. Damstahl Academy. Titanium Stabilized Stainless Steel. https://www.damstahl.com/Files/Billeder/2011/PDF/UK/titanium_steel.pdf (2011).

35. Amuda, M. O. H. & Mridha, S. An Overview of Sensitization Dynamics in Ferritic Stainless Steel Welds. *Int. J. Corros.* (2011) doi:10.1155/2011/305793.

36. Knutsen, R. D. & Hutchings, R. Occurrence of Non-Metallic Inclusions in 3CR12 Steel and Their Effect on Impact Toughness. *Mater. Sci. Technol.* **4**, 127–135 (1988).

37. ASTM International. ASTM A709/A709M: Standard Specification for Structural Steel for Bridges. (2017) doi:10.1520/A0709.

38. ArcelorMittal. Durcorr/A1010: Bridge Applications and Fabrication Guidelines. https://usa.arcelormittal.com/~/media/Files/A/Arcelormittal-USA-V2/what-we-do/steel-products/plate-products/Duracorr-Bridge.pdf (2013).

39. Seradj, H. Weldability of ASTM A1010 Steel. in *Proceedings of 8th International Conference on Short and Medium Span Bridge* (2010).

40. Provines, J. T., Sharp, S. R., Ozbulut, O. & Daghash, S. *Maintenance-Free Corrosion-Resistant Steel Plate for Bridges*. (2019).

41. Easterling, K. *Introduction to the Physical Metallurgy of Welding*. (Buttersworth-Heinemann Ltd., 1992).

42. Messler Jr, R. W. & Savage, W. F. *Principles of Welding: Processes, Physics, Chemistry, and Metallurgy*. (John Wiley and Sons Inc., 1999).

43. TWI Ltd. Submerged Arc Welding Process. https://www.twi-global.com/technical-knowledge/job-knowledge/submerged-arc-welding-process-005.

44. Poorhaydari, K., Patchett, B. M. & Ivey, D. G. Estimation of Cooling Rate in the Welding of Plates with Intermediate Thickness. *Weld. J. Suppl.* 149–155 (2005).

45. Meyer, A. M. Interstitial Diffusion from the Weld Metal into the High Temperature Heat Affected Zone in 11–12 Percent Chromium Steel Welded Joints. (University of Pretoria, 2000).

46. Sieurin, H. Fracture Toughness Properties of Duplex Stainless Steels. (Royal Institute of Technology, 2006).

47. Hong, J. Y., Shin, Y. T. & Lee, H. W. Characterization of Corrosion Resistance in a

Ferritic Stainless Steel Stabilized with Ti Addition. *Int. J. Electochemical Sci.* **9**, 7325–7334 (2014).

48. David, S. A., Vitek, J. M. & Alexander, D. J. Embrittlement of Austenitic Stainless Steel Welds. *J. Nondestruct. Eval.* **15**, 129–136 (1996).

49. Select Arc Inc. Select Arc Premium Welding Products - Full Line Catalog. http://select-arc.com/products/pdf/master_select-arc_catalog_2.17-updated.pdf (2018).

50. Prajapati, P. & Badheka, V. J. Investigation on Various Welding Consumables on Properties of Carbon Steel Material in Gas Metal Arc Welding Under Constant Voltage Mode. *Sadhana* **42**, 1751–1761 (2017).

51. Shirzadi, A. A., Bhadeshia, H. K. D. H., Karlsson, L. & Withers, P. J. Stainless Steel Weld Metal Designed to Mitigate Residual Stresses. *Sci. Technol. Weld. Join.* **14**, 559–565 (2009).

52. Myers, D. Advantages and Disadvantages of Metal Cored Wires. https://www.esabna.com/us/en/education/blog/advantages-and-disadvantages-of-metal-cored-wires.cfm.

53. Polymet. The Benefits of Using Metal Cored Wire. http://www.polymet.us/wp-content/uploads/2016/12/The-Benefits-of-Using-Metal-Cored-Wire.pdf.

54. Lyttle, K. A. Metal Cored Wires: Where Do They Fit in Your Future? *Weld. J.* **75**, 35–38 (1996).

55. Columbus Stainless. Tehnical Data: 3CR12, 3CR12L, CS410S. https://sassda.co.za/wp-content/uploads/2013/10/technical_data_3CR122.pdf (2007).

56. Koseki, T. & Flemings, M. C. Solidification of Undercooled Fe-Cr-Ni Alloys: Part II Microstructural Evolution. *Metall. Mater. Trans. A Phys. Metall. Mater. Sci.* **27**, 3226–3240 (1996).

57. Shankar, V., Gill, T. P. S., Mannan, S. L. & Sundaresan, S. Solidification Cracking in Austenitic Stainless Steel Welds. *Sadhana* **28**, 359–382 (2003).

58. Karlsson, L., Arcini, H., Bergquist, E. L., Weidow, J. & Börjesson, J. Effects of Alloying Concepts on Ferrite Morphology and Toughness of Lean Duplex Stainless Steel Weld Metals. *Weld. World* **54**, 350–359 (2010).

59. Lippold, J. C. *Welding Metallurgy and Weldability*. (John Wiley and Sons Inc., 2015).

60. ASTM International. ASTM E1417/E1417M: Standard Practice for Liquid Penetrant Testing. (2016) doi:10.1520/E1417.

61. American Welding Society. AWS D1.5M/D1.5 Bridge Welding Code. (2015).

62. Dupont, J. N. Dilution in Fusion Welding. *ASM Handbook, Weld. Fundam. Process.* **6A**, 115–121 (2011).

63. Lundin, C. D., Delong, W. T. & Spond, D. F. Ferrite-Fissuring Relationship in Austenitic Stainless Steel Weld Metals. *Weld. J. Suppl.* **54**, 241–246 (1975).

64. Wang, P., Lu, S. P., Xiao, N. M., Li, D. Z. & Li, Y. Y. Effect of Delta Ferrite on Impact Properties of Low Carbon 13Cr – 4Ni Martensitic Stainless Steel. *Mater. Sci. Eng. A* **527**, 3210–3216 (2010).

65. Kotecki, D. J. Ferrite Control in Duplex Stainless Steel Weld Metal. *Weld. J. Suppl.* **65**, 273–278 (1986).

66. Mathers, G. Welding of Austenitic Stainless Steel Part 2. https://www.twi-global.com/technical-knowledge/job-knowledge/welding-of-austenitic-stainless-steel-part-2-104.

67. ASTM International. ASTM A370: Standard Test Methods and Definitions for Mechanical Testing of Steel Products. (2017) doi:10.1520/A0370-14.2.

68. Dieter, G. E. *Mechanical Metallurgy*. (McGraw Hill Education (India) Private Limited, 2013).

69. Mathers, G. Bend Testing. https://www.twi-global.com/technical-knowledge/job-knowledge/bend-testing-073 (2004).

70. Hertzberg, R. W., Vinci, R. P. & Hertzberg, J. L. *Deformation and Fracture Mechanics of Engineering Materials*. (Wiley India Private Limited, 2014).

71. Chai, G. Ductile to Brittle Transition Behavior of Super Duplex Stainless Steels. *Struct. Durab. Heal. Monit.* **3**, 191–196 (2007).

72. Seradj, H. Oregon's Experience with ASTM A1010. in *TRB 9th Annual Meeting Compendium of Papers* (Transportation Research Board of the National Academies, 2015).

73. Seradj, H. Oregon's First ASTM A1010 Bridge and Risk Management. in *World Steel Bridge Symposium* (American Institute of Steel Construction, 2012).

74. ArcelorMittal. Plate: Duracorr: Welding Guidelines. https://usa.arcelormittal.com/~/media/Files/A/Arcelormittal-USA-V2/what-we-do/steel-products/plate-products/Duracorr-welding.pdf (2010).

75. Medlock, R., Gilmer, H., Miller, D. & Ream, A. Bridge Welding Reference Manual. (2019).

76. Wright, W. J. Steel Bridge Design Handbook: Bridge Steels and Their Mechanical Properties. vol. 1 (2015).

77. New York State Department of Transportation. Contract Administration Manual. (2016).

78. Federal Highway Administration. FHWA's Buy America Q and A for Federal-aid Program. https://www.fhwa.dot.gov/construction/contracts/buyam_qa.cfm (2017).

79. American Welding Society. AWS A5.9/A5.9M Specification for Bare Stainless Steel Welding Electrodes and Rods w/Errata. (2006).

80. American Welding Society. AWS A5.22/A5.22M Specification for Stainless Steel Flux Cored and Metal Cored Electrodes and Rods. (2012).

81. ASTM International. ASTM E1019: Standard Practice for Describing and Specifying Inductively Coupled Plasma Atomic Emission Spectrometers. (2018).

82. ASTM International. ASTM E1479: Standard Test Methods for Determination of Carbon, Sulfur, Nitrogen, and Oxygen in Steel, Iron, Nickel, and Cobalt Alloys by Various Combustion and Inert Gas Fusion Techniques. (2016).

83. ASTM International. ASTM E407: Standard Practice for Microetching Metals and Alloys. (2015) doi:10.1520/E0407-07R15E01.2.

84. ASTM International. ASTM E23: Standard Test Methods for Notched Bar Impact Testing of Metallic Materials. (2016) doi:10.1520/E0023-12C.2.

85. ASTM International. ASTM A751: Standard Test Methods , Practices , and Terminology for Chemical Analysis of Steel Products. (2014) doi:10.1520/A0751-14A.priate.

86. Vander Voort, G. F. & Manilova, E. P. Hints for Imaging Phases in Steels. *Adv. Mater. Process.* **163**, 32–37 (2005).

87. ArcelorMittal. Guidelines for Fabricating and Processing Plate Steel. https://usa.arcelormittal.com/~/media/Files/A/Arcelormittal-USA-V2/what-we-do/steel-products/plate-products/Fabrication-guide.pdf (2015).

88. Blum, F., Comins, N. R. & Weiss, B. Z. The Influence of Microstructural Parameters on the Yield Stress and Fracture Toughness of 3CR12 Steel. *J. South African Inst. Min. Metall.* **92**, 185–193 (1992).

89. Akinlabi, E. T. & Akinlabi, S. A. Characterising the Effects of Heat Treatment on 3CR12 and AISI 316 Stainless Steels. *Int. J. Mech. Aerospace, Ind. Mechatronic, Manuf. Eng.* **8**, 256–261 (2014).

90. Klopper, J. J., Laubscher, R. F., Steuwer, A. & James, M. N. An Investigation into the Effect of Weld Technique on the Residual Stress Distribution of 3CR12(DIN 1.4003) Built-Up Structural Sections. *Proc. Inst. Mech. Eng. Part L J. Mater. Des. Appl.* **225**, 123–132 (2011).

91. Thomas, C. R. 3CR12 - One of the New Generation of 12% Chromium Corrosion Resisting Steels. *Chemsa* vol. 8 50–55 (1982).

92. Schade, C. T., Murphy, T. F., Lawley, A. & Doherty, R. D. Development of a Dual-Phase-Precipitation-Hardening PM Stainless Steel. *Int. J. Powder Metall.* **45**, 38–46 (2009).

93. Chauhan, Y. Transmission Electron Microscopy of a Dual Phase Steel Designated 3CR12. in *Electron Microscopy Society of Southern Africa Proceedings* vol. 14 155–156 (Electron Microscopy Society of Southern Africa, 1984).

94. Siyasiya, C. W. The Transformation Behaviour and Hot Strength of 3CR12 During the Continuous Casting Process. (University of Pretoria, 2004).

95. Yan, W. *et al.* Delamination Fracture Related to Tempering in a High-Strength Low-Alloy Steel. *Metall. Mater. Trans. A Phys. Metall. Mater. Sci.* **41A**, 159–171 (2010).

96. Meier, M. Plastic Deformation and the Onset of Tensile Instability. (2004).

97. Hosford, W. F. & Caddell, R. M. *Metal Forming: Mechanics and Metallurgy*. (Cambridge University Press, 2007).

98. Chandra, K. *et al.* Low Temperature Thermal Aging of Austenitic Stainless Steel Welds: Kinetics and Effects on Mechanical Properties. *Mater. Sci. Eng. A* **534**, 163–175 (2012).

99. Meyer, A. M. & Du Toit, M. Interstitial Diffusion of Carbon and Nitrogen into Heat-Affected Zones of 11-12% Chromium Steel Welds. *Weld. J. Suppl.* **80**, 275–280 (2001).

100. Suutala, N., Takalo, T. & Moisio, T. Ferritic-Austenitic Solidification Mode in Austenitic Stainless Steel Welds. *Metall. Mater. Trans. A Phys. Metall. Mater. Sci.* **11A**, 717–724 (1980).

101. TWI Ltd. Embrittlement of Austenitic Steel Welds at High Temperature. https://www.twi-global.com/technical-knowledge/faqs/faq-what-is-the-origin-of-embrittlement-in-austenitic-stainless-steel-welds-exposed-to-high-temperatures.

102. Chang, E. & Ye, X. Analysis of the Microstructure and Mechanical Properties of 309L Austenitic Stainless Steel. *Baosteel Tech. Res.* **6**, 57–60 (2012).

103. Aguilar, S., Tabares, R. & Serna, C. Microstructural Transformations of Dissimilar Austenite-Ferrite Stainless Steels Welded Joints. *J. Mater. Phys. Chem.* **1**, 65–68 (2013).

104. American Welding Society. AWS D1.1 Structural Welding Code-Steel. (2000).

105. Matsukawa, Y. *et al.* The Two-Step Nucleation of G-Phase in Ferrite. *Acta Mater.* **116**, 104–113 (2016).

106. Subramanian, G. O., Kong, B. S., Lee, H. J. & Jang, C. Evaluation of the Thermal Aging of δ -Ferrite in Austenitic Stainless Steel Welds by Electrochemical Analysis. *Nat. Sci. Reports* **8**, 1–17 (2018).

107. Azizova, S. K. & Lyalin, K. V. Research into Melting and Transfer of Electrode Metal during Welding with Cored Electrode Wire. *Weld. Prod.* **16**, 13–17 (1969).

108. French, I. E. & Bosworth, M. R. Comparison of Pulsed and Conventional Welding with Basic Flux Cored and Metal Cored Welding Wires. *Weld. J. Suppl.* **74**, 197-s-205-s (1995).

109. Matsuda, F., Ushio, M., Tsuji, T. & Mizuta, T. Arc Characteristics and Metal Transfer with Flux-Cored Electrode in CO2 Shielding (Report I): Effect of Geometrical Shape in Wire Cross-Section on Metal Transfer in Stainless Steel Wire (Welding Physics, Processes, and Instruments). *Trans. JWRI* **8**, 187–192 (1979).

110. Ushio, M., Raja, A. & Matsuda, F. Melting Characteristics of Flux Cored Wire (Welding Physics, Process and Instrument). *Trans. JWRI* **13**, (1984).

111. Toit, M. & Naudé, J. The Influence of Stabilization with Titanium on the Heat Affected Zone Sensitization of 11 to 12 % Chromium Ferritic Stainless Steels under Low Heat Input Welding Conditions. *Weld. i* **55**, 38–47 (2011).

112. van Warmelo, M., Nolan, D. & Norrish, J. Mitigation of Sensitisation Effects in Unstabilised 12%Cr Ferritic Stainless Steel Welds. *Mater. Sci. Eng. A* **464**, 157–169

(2007).

113. Lakshminarayanan, A. K. & Balasubramanian, V. Assessment of Sensitization Resistance of AISI 409M Grade Ferritic Stainless Steel Joints Using Modified Strauss Test. *Mater. Des.* **39**, 175–185 (2012).

114. ASTM International. ASTM A262: Standard Practices for Detecting Susceptibility to Intergranular Attack in Austenitic Stainless Steels. (2015) doi:10.1520/A0262-15.